



Contents lists available at ScienceDirect

Journal of Pharmaceutical Analysis

journal homepage: www.elsevier.com/locate/jpa
www.sciencedirect.com

Review Paper

3D biofabrication of vascular networks for tissue regeneration: A report on recent advances

M.D. Sarker^{a,*}, Saman Naghieh^a, N.K. Sharma^b, Xiongbiao Chen^{a,b,**}^a Division of Biomedical Engineering, College of Engineering, University of Saskatchewan, Saskatoon, SK, Canada^b Department of Mechanical Engineering, College of Engineering, University of Saskatchewan, Saskatoon, SK, Canada

ARTICLE INFO

Article history:

Received 12 June 2018

Received in revised form

24 August 2018

Accepted 26 August 2018

Available online 28 August 2018

Keywords:

3D bioprinting

Tissue engineering

Vascularization

Extrusion

Laser-based printing

Co-axial printing

ABSTRACT

Rapid progress in tissue engineering research in past decades has opened up vast possibilities to tackle the challenges of generating tissues or organs that mimic native structures. The success of tissue engineered constructs largely depends on the incorporation of a stable vascular network that eventually anastomoses with the host vasculature to support the various biological functions of embedded cells. In recent years, significant progress has been achieved with respect to extrusion, laser, micro-molding, and electrospinning-based techniques that allow the fabrication of any geometry in a layer-by-layer fashion. Moreover, decellularized matrix, self-assembled structures, and cell sheets have been explored to replace the biopolymers needed for scaffold fabrication. While the techniques have evolved to create specific tissues or organs with outstanding geometric precision, formation of interconnected, functional, and perfused vascular networks remains a challenge. This article briefly reviews recent progress in 3D fabrication approaches used to fabricate vascular networks with incorporated cells, angiogenic factors, proteins, and/or peptides. The influence of the fabricated network on blood vessel formation, and the various features, merits, and shortcomings of the various fabrication techniques are discussed and summarized.

© 2018 Xi'an Jiaotong University. Production and hosting by Elsevier B.V. This is an open access article under the CC BY-NC-ND license (<http://creativecommons.org/licenses/by-nc-nd/4.0/>).

1. Introduction

Tissue regeneration requires the simultaneous growth of vasculature to facilitate the diffusional mass transfer of nutrients, oxygen, growth factors, biochemical signaling factors, carbon dioxide, and metabolic waste from the surroundings to cells and vice versa [1,2]. In particular, the vascular network should reach within 100–200 μm of the tissue to avoid ischemic conditions and cell death [3]. Blood vessels with different diameters (~4–300 μm) spread in a complicated fashion (i.e., fractal shapes) into tissue to exchange nutrients, gas, and metabolites to a huge cell population [4]. Capillaries in the vascular network play a vital role in the mass transfer mechanism. Therefore, tissue regeneration with scaffolds requires the incorporation of an interconnected capillary network with vessels located every 100–200 μm in all directions.

Tissue vascularization is a complex process that develops through vasculogenesis and angiogenesis in vivo [4–6]. In vasculogenesis,

endothelial progenitor cells (EPCs) migrate to an ischemic site, proliferate, and differentiate to form capillary vessels, while angiogenesis occurs when new blood vessels sprout from existing ones according to a gradient of angiogenic factors [5,7]. The blood vessels formed by either vasculogenesis or angiogenesis are eventually remodeled and mature as per the demands of specific tissues through the upregulation of various growth factors.

Taking into account the in vivo vasculature formation mechanism, a number of 3D fabrication approaches have evolved over past decades to mimic the native vascular network. Direct and indirect bioprinting approaches have proven promising for the fabrication of large 3D tissue constructs with intricate vascular networks. The use of coaxial needles in extrusion-based (EB) systems revolutionized these biofabrication techniques and resulted in the ability to print lumen-incorporated strands. Indirect biofabrication is convenient when scaffolding biopolymers demonstrate poor printability and manipulation complexity. In this regard, sacrificial biopolymers are a smart choice of scaffolding material in vascular network fabrication. In addition to EB biofabrication, several potential approaches including micro-pattern fabrication and assembly, laser-based fabrication, nano-scale fabrication, and natural matrix recellularization have evolved to generate vascular networks. Stacking 2D micropatterned substrates or micro tissue modules results in the formation of complex interconnected vascular networks. Laser-based fabrication

Peer review under responsibility of Xi'an Jiaotong University.

* Corresponding author.

** Corresponding author at: Division of Biomedical Engineering, College of Engineering, University of Saskatchewan, Saskatoon, SK, Canada.

E-mail addresses: mas921@mail.usask.ca (M.D. Sarker), xb719@mail.usask.ca (X. Chen).<https://doi.org/10.1016/j.jpba.2018.08.005>2095-1779/© 2018 Xi'an Jiaotong University. Production and hosting by Elsevier B.V. This is an open access article under the CC BY-NC-ND license (<http://creativecommons.org/licenses/by-nc-nd/4.0/>).

allows both 2D and 3D fabrication in a layer-by-layer fashion in the presence of a photo mask, donor substrate, photo sensitive polymer, or photo initiator. Electrospinning, an advanced fabrication technique reported in numerous studies [8–11], supports the fabrication of extracellular matrix (ECM)-like nano-scale filaments that enhance the interaction with endothelial cells (ECs). Seeding ECs into decellularized tissue matrix promotes vascularization, with the preparation process affecting the quality of the native matrix.

A review of recent progress with respect to tissue vascularization with available fabrication techniques is necessary to guide future research. Several articles have focused on the synergistic effect of cells, biopolymers, angiogenic factors, and fabrication approaches in terms of tissue vascularization. However, review articles that focus on recent progress in terms of 3D vasculature formation techniques are lacking. This article provides a brief overview of the 3D biofabrication of vascular networks with EB, laser, electrospinning, stacking of micropattern or modules, and cell sheet techniques; discusses the effect of prevascularization on the vascular network formed by the various fabrication techniques; summarizes the challenges, advantages, and shortcomings of different fabrication approaches; and proposes potential future research directions.

2. Rapid prototyping

2.1. Bio-printing vascular networks

Macro-scale tissue constructs require well connected vascular networks to ensure the viability of the large cell population embedded or seeded in the scaffold. Embedded tissue-/organ-specific cells require time to form functional tissues and, during this period, require nutrients, gas, and biomolecules to maintain metabolism, proliferation, and differentiation and enable remodeling. Therefore, researchers have attempted to form perfusable capillary networks within macro-engineered grafts seeded with different types of cells. Specifically, some researchers have used rapid prototyping (RP) or additive manufacturing techniques to form complex capillary networks with hydrogel-based, fugitive, and sacrificial ink. Extrusion- (e.g. 3D bioplotting, and inkjet printing) and laser-based (e.g. stereolithography) techniques in particular have achieved outstanding results with respect to printing vascular networks with intricate architecture.

2.1.1. Inkjet-based bioprinting

Bioprinting of cells ensures a higher cell density in the scaffold compared to post fabrication cell seeding. A number of studies conclude that higher cell densities in the scaffold promote tissue generation by secreting numerous bio-molecules. Therefore, researchers have emphasized 3D bioprinting to incorporate a huge cell population in the scaffold in a controlled and well-distributed fashion. For bioprinting mixtures of cells and hydrogels, extrusion-based RP approaches have been explored in many studies. In particular, inkjet printers and 3D bioplotters are commonly used for scaffold and vascular network printing due to some attractive features. In inkjet printing, bioink drops are dispensed layer-by-layer, while a bioplotting system extrudes continuous filaments to fabricate a predefined structure based on computer-generated (CAD) digital data. Thermal- and piezoelectric-based inkjet bioprinters can print a cell-crosslinking ion mixture at high resolution and speed on hydrogel precursors. In general, hydrogels with rapid gelation properties are used in inkjet systems to handle the high printing speed. Moreover, inkjet printers allow the deposition of multiple cell types in a controlled and organized fashion to mimic the distribution of multiple cells in native tissues. Different inkjet printing studies used alginate or its composites as a bioink and calcium chloride as a crosslinker [12–16], with vascular networks shown to grow after in vitro or in vivo culture. In one study, three bioinks containing canine

smooth muscle cells, human amniotic fluid-derived stem cells, and bovine aortic endothelial cells, respectively, were used to print an alginate-collagen scaffold layer-by-layer using a thermal inkjet printer; vascularized, mature, and functional tissues grew when the scaffolds were implanted in vivo [17]. Likewise, bioink composed of human microvascular endothelial cells (HMVECs) and thrombin solution and dispensed on fibrinogen using an inkjet printer resulted in the alignment and proliferation of the HMVECs and the formation of a capillary-like tubular structure inside the channels [18]. Although inkjet printers are economical and have several attractive features, shortcomings including nozzle clogging, cavitation bubbles, selective ink viscosity, and cell damage during dispensing limit their use for the fabrication of vascular networks [19].

2.1.2. Extrusion-based bioprinting

Several studies have explored both indirect and direct EB techniques in fabricating intricate vascular network to date. In indirect printing, tissue-specific, cell-incorporated hydrogels are used to encapsulate a prefabricated sacrificial vascular network, followed by the removal of the sacrificial ink using an appropriate solvent. ECs are then seeded around the capillary channels using an injection/microfluidic approach. The perfusion of the capillary network with media or blood forms a monolayer of ECs around the capillaries within a couple of days that facilitates diffusional mass transfer and eventual remodeling into blood vessels.

Cytocompatible sacrificial templates have been explored to avoid the use of cytotoxic organic solvents or processing conditions to eliminate the sacrificial filaments from engineered constructs [20] (Fig. 1). In one study, carbohydrate glass filaments were dispensed at 110 °C using a 3D printer to form a patterned 3D network, and then the network was encapsulated in an agarose polymer loaded with primary rat hepatocytes and fibroblast cells. The soluble sacrificial filaments were removed by the cell culture media, the vascular lumen then seeded with human umbilical vein endothelial cells (HUVECs), and the vascular network perfused with blood in vivo. This vascularized construct supported the metabolic function of primary rat hepatocytes, which maintained higher albumin secretion and urea synthesis than in gels without channels [21]. However, complexities related to high temperature dispensing, random distribution of multiple cell types, and hygroscopic behavior of carbohydrate filaments limit vascularization applications. A number of studies have investigated the efficacy of sacrificial networks with respect to generating vasculature. Rather than random incorporation of multiple types of tissue- or organ-specific cells in the matrix, capillary vessels and various types of cells were printed separately side-by-side to mimic the native tissue or organ. In one study, a 3D bioprinting technique was used to co-print fibroblast-laden GelMA, fugitive ink, and human neonatal dermal fibroblast-loaded GelMA strands layer-by-layer. The vascular network fabricated in this way was encapsulated into GelMA, and then the fugitive ink (Pluronic[®] F127) removed by liquifying at 4 °C. When the HUVECs were injected in the fugitive ink-removed lumen followed by gentle rocking, greater than 95% viability was achieved with a confluent EC layer identified 48 h after seeding [22].

Extrusion-based systems featuring coaxial or shell/core nozzles have been used to directly print hollow fibers or filaments with a microfluidic channel to form a vascular network [23,24]. In particular, Fig. 2 shows that the flow of ionic crosslinker (e.g. CaCl₂) is maintained in the core side of a coaxial nozzle while the flow of hydrogel is maintained in the shell side [25]. The flow rheology of the hydrogel precursor and crosslinker as well as the hydrogel percentage significantly affects the geometry of the core diameter, wall thickness, and microfluidic channels. Such 3D microfluidic networks can be encapsulated into hydrogels containing multiple cell types. In general, microfluidic channels fabricated with a coaxial nozzle-extrusion system are seeded with ECs, and then

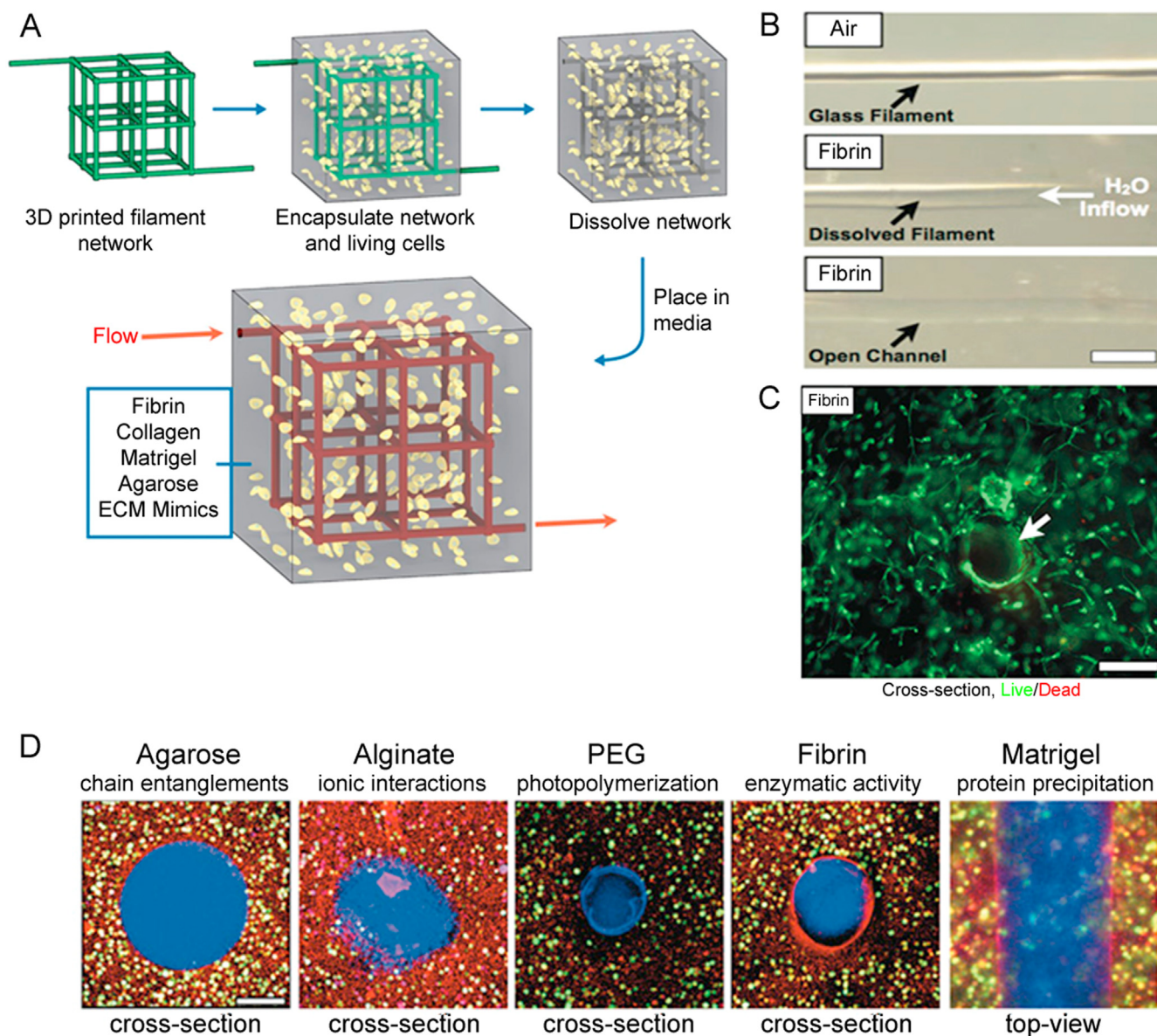


Fig. 1. (A) Carbohydrate glass lattice as the sacrificial structure for the creation of vascular architecture, (B) a single carbohydrate glass fiber encapsulated in a fibrin gel, (C) cross-section image of unlabeled HUVEC and 10T1/2 co-cultures (not expressing enhanced green fluorescent protein (EGFP)) encapsulated in the interstitial space of fibrin gel with perfusable channels, and (D) cross-section of cell-incorporated biomaterials (scale bars = 200 μ m) (reproduced with permission from [21]).

perfused with culture media or blood to promote capillary blood vessel formation. Alteration of shell/core size significantly affects the ultimate strength, compressive strength, and Young's modulus of the hollow fibers [26]. In addition to seeding, ECs can also be encapsulated in the shell of the hollow channel during fabrication to generate high cell densities [27]. In some studies, tissue spheroids composed of tissue-specific cells were dispensed simultaneously in the space between two successive hollow filaments using multiple robotic arms [28]. Several studies report the efficacy of microfluidic channels fabricated with a coaxial nozzle for promoting vasculature. When human bone marrow stromal cells (hBMSCs) were seeded on the inner walls of hollow alginate-poly(vinyl alcohol) (PVA) fibers extruded from a coaxial nozzle, they showed excellent attachment and spreading after 14 days of culture [26]. Similarly, cartilage progenitor cell (CPC)-encapsulated sodium alginate has been extruded from a coaxial nozzle to form the shell of a microfluidic channel. Initially, CPC viability decreased due to the dispensing pressure, coaxial nozzle geometry, and

alginate concentration, but improved significantly over 7 days of incubation [27].

To date, a wide range of natural, synthetic, and hybrid biomaterials have been used in bioprinting; however, none are free from shortcomings. Most biomaterials show uncontrolled degradation, immunogenicity, inflammation, and cytotoxicity in vivo or in vitro applications. In some cases, biomaterials inhibit ECM secretion, distribution, and organization as well as cell-cell communication. To address these issues, researchers have investigated self-assemble approaches in which scaffold-free multicellular spheroids or filaments are extruded using a bioprinter. In such systems, sacrificial spheroids and multicellular tissue spheroids are concurrently printed layer-by-layer as per the CAD design. Upon incubation in a bioreactor, the multicellular spheroids fuse together to form single- or double-layered microvascular tubes. The fusion process is time-consuming and causes non-uniform tubular surfaces, and the fabrication of long vascular tubes is a slow process and demonstrates poor spatial resolution. To tackle

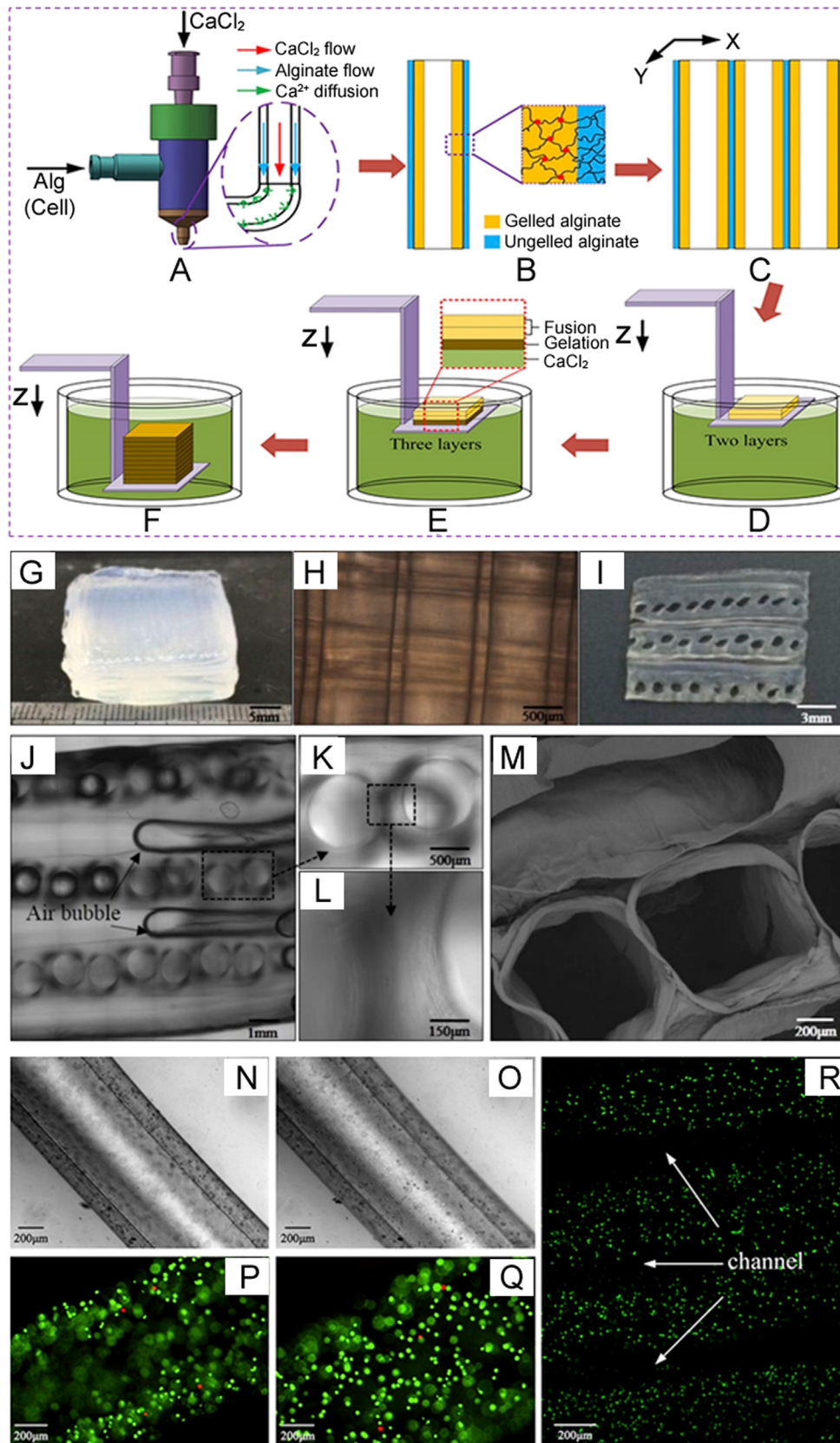


Fig. 2. Coaxial printing of scaffolds fabricated by an extrusion-based technique: (A) crosslinker diffusion while the biomaterial is extruding through the outer tube, (B) crosslinking of biomaterial, (C) deposition of numerous strands, (D–F) printing layers of scaffolds and immersing in crosslinker, and characterization of the fusion phenomenon between adjacent alginate hollow filaments: (G) macroscopic image of a cuboid scaffold containing six layers of hollow strands, (H) inverted microscopic image of longitudinal section of the scaffold, (I) macroscopic image of the scaffold cross-section, (J–L), confocal microscopic images at different magnifications showing the cross-section of the scaffold, (M) SEM image of fused filaments, with fibroblasts encapsulated in hollow alginate filaments, (N and O) microscopic images showing the lumen and wall of the hollow strands (white light), (P and Q) laser confocal images showing the lumen and wall of the hollow strands, and the live and dead cells as fluorescent green and fluorescent red, respectively, and (R) laser confocal image revealing the fused structure with channels (reproduced with permission from [29]).

these issues, RP technology has been used to bioprint cylindrical multicellular building blocks using collagen gel as a biopaper. However, vascular cells eventually integrate with the collagen rod in the fusion process, which causes complexities in the removal of the collagen gel from the vascular cell-fused hollow channels. Extruded inert agarose rods as a molding template solved the issues related to the collagen gel. When human umbilical vein smooth muscle cells and dermal fibroblasts were dispensed as a multicellular cylinder according to the CAD design, double-layered vascular walls formed 3 days after fusion [30].

2.2. Laser-based 3D printing

Laser-based bioprinting, particularly laser-guided direct writing (LGDW) and matrix-assisted pulsed laser evaporation direct writing (MAPLE DW), have been explored in different studies for 2D and 3D cell patterning [31]. This printing technique has some attractive features, including no nozzle clogging and the ability to print cells at high resolution and accuracy with high-viscosity bioink. Compared to laser-induced forward transfer (LIFT), the MAPLE DW technique uses a lower powered pulsed laser to deposit multiple cell types. In this technique, laser pulse-induced bubbles create shock waves that compel cells to move toward the collector substrate. A number of studies have used laser-based bioprinting to print patterned structures with vascular cells and observed capillary vessel formation. For example, a study using the LIFT-based cell printing technique to print HUVECs and human mesenchymal stem cells (hMSCs) in a defined pattern on a cardiac patch reported increased capillary vessel density and functional improvement of infarcted hearts [32]. Researchers have also used LGDW to print a 3D vascular network by stacking cell aggregates layer-by-layer, with a hydrogel layer placed on top of each deposited cell aggregate. LGDW-printed 3D patterned HUVEC on Matrigel™ formed elongated and tube-like structures in vitro [33]. However, shortcomings such as long fabrication time, laser-induced cell damage, and low scalability limit the application of the techniques in tissue vascularization.

Stereolithography, a maskless photolithography, has been investigated to generate complex 3D vascular patterns with photosensitive materials [34]. In particular, digital light projection (DLP) and laser-based stereolithography have been used to print intricate architectures based on designs developed from CAD software, computer tomographic, and magnetic resonance imaging (MRI) scanned information [35]. In a DLP system, a digital mirror device containing several million tiny mirrors regulates the movement of the mirrors via a digital signal. This rotation of mirrors causes a two-dimensional pixel-pattern that is projected on the photo-curable biomaterial to obtain intricate 3D structures. In a study, a DLP chip was used to generate active and reflective dynamic photomasks as per the CAD drawing. Then the cross-sectional images of the 3D microstructure were reproduced from photomasks and the images were projected onto the methacrylate (GelMA) solution using an ultraviolet (UV) light source. When the 3D intricate pattern was seeded with HUVECs, the HUVECs formed a confluent monolayer and maintained their phenotype for 4 days following dynamic seeding [36]. Similarly, another study reported that HUVECs formed cord-like structures after 4 days of culture in a scaffold fabricated with a DLP system [37]. While this technique can print 3D structures quickly with high resolution, shortcomings such as high costs, less detailed printing for large constructs, and cytotoxicity limit the application of the DLP technique.

Laser-based stereolithography (LS) was developed to eliminate the requirement of a photomask and assembly of multiple 2D planar surfaces to form 3D vascular networks. Although LS is suitable for printing large and detailed vascular constructs, the

lower printing speed of LS compared to the DLP technique needs to be improved [38]. In this technique, a computer-controlled ultraviolet laser beam generates a pattern on a photosensitive material as per the CAD design [39], as shown in Fig. 3. A number of researchers have printed complicated structures with LS and reported outstanding results with respect to forming vasculature. Post-fabrication seeding of ECs in the LS-printed scaffold showed improved viability, whereas incorporated cells in the photosensitive hydrogel demonstrated low viability due to laser (short wavelength)-induced cell damage. To avoid short wavelengths, researchers have employed two- or multi-photon laser systems to print intricate 3D structures with micro- or nano-scale precision [40]. Although the two- and multi-photon laser systems maintain a less harsh environment than LS during printing, use of a photo-initiator in the gelation process significantly decreases cell viability [38]. To address this issue, a multi-photon printing technique was used to fabricate 3D multi-scale patterns in soft silk protein hydrogels without using a photo-initiator; the 3D features supported the growth and penetration of human mesenchymal stem cells deep into the gel [41]. Several studies have investigated the efficacy of vascular patterns/networks printed with the LS technique with respect to promoting vascular tissue. In one study, polytetrahydrofuran diacrylate resin-based macro-scale vascular tubes and micro-scale bifurcating tubes were printed using LS and two-photon polymerization (2PP) techniques, respectively. Acellular vascular vessels printed using this method could be seeded with ECs to form vasculature, because the grafts demonstrated good cytocompatibility and mechanical properties similar to native capillaries [42]. Similarly, when granulosa cells were seeded on an epoxy-based acellular microcapillary vascular tree printed with the 2PP technique, improved cell growth and sustained cell-cell junctions were identified in vitro [43]. These studies demonstrate that EC monolayer formation is possible in an LS-printed vascular pattern.

3. Assembled scaffolds

3.1. Micro-patterning/microfluidics

Native tissue contains macro- and micro-blood vessels that supply nutrients, oxygen, and other bio-molecules to large cell populations. A number of studies have investigated micro-patterned substrates to create capillary bed-like structures that mimic native tissue as shown in Fig. 4. Biophysical factors, such as ECM stiffness, interstitial and shear flow have significant effects on capillary vessel formation in micropatterned substrates. In particular, interstitial flow regulates capillary morphogenesis [45], shear stress enhances angiogenesis [46], and material stiffness regulates the architecture of the capillary network in the developing tissue. In one study, bovine pulmonary microvascular ECs seeded in rigid collagen gels formed thick and deep vascular networks with large capillary lumens, while those seeded in a flexible hydrogel formed thin and intense networks with tiny lumen [47]. Researchers have used plasma etching [48], laser ablation [49], soft lithography [50], and replica molding [51] to generate microfluidic patterns on biocompatible substrates. Researchers have also used a direct write laser technique to prepare microchannels with various widths and depths following Murray's law to closely mimic the capillary architecture seen in vivo. Such micropatterns facilitate the uniform flow of fluid and achieve low resistance similar to that of physiological vascular systems [52].

To date, several methods have been developed to seed vascular and tissue-specific cells on patterned substrates. In one study, ECs and mural cells (i.e. smooth muscle cells (SMCs) and pericytes) were seeded in a single-layered substrate following a microfluidic

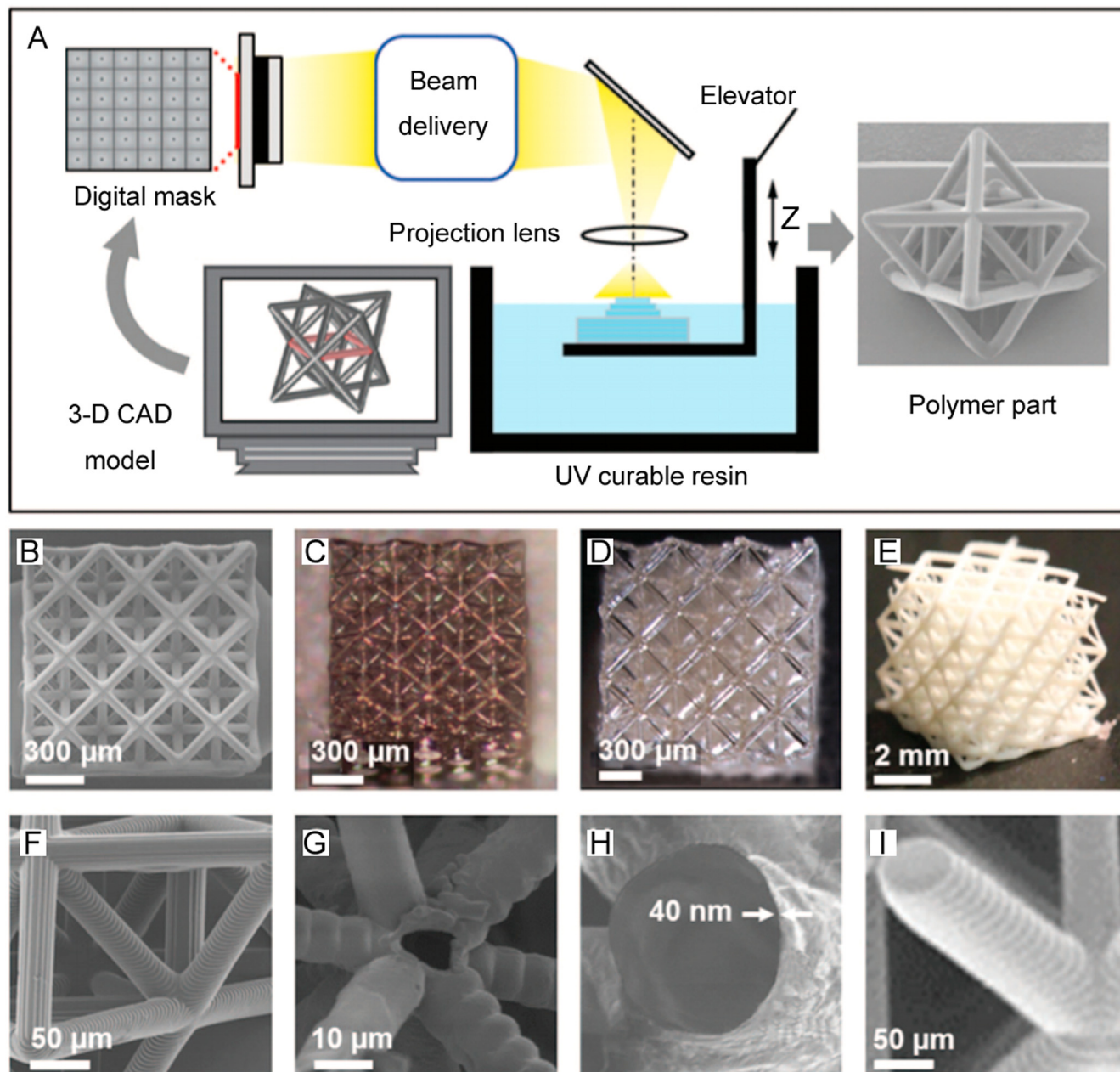


Fig. 3. Fabrication of scaffolds using a computer-controlled ultraviolet laser beam: (A) projection microstereolithography (SEM image at right is an octet-truss unit cell), (B–E) octet-truss structures with different patterns and biomaterials, and (F–I) SEM images of the struts of structures in (B–E) (reproduced with permission from [44]).

approach, and then cultured for a certain period of time to promote stable capillary formation [54]. Several studies report that microfluidics regulate the temporal and spatial distribution of cells, media, enzymes, and biomolecules within the micropattern [55]. Further, microfluidics facilitates the formation of patterned cell distribution and shear-induced endothelialization in a co-culture system [56]. Especially in a microfluidic system, circulating biomolecules and the applied gradient of shear stress into the microchannel regulate the morphology, reorganization, alignment, differentiation, and remodeling of ECs that are significant for capillary formation [57]. To regulate shear stress, researchers have applied computational microfluidics and different fluid flow patterns (e.g. laminar, pulsatile, and turbulent) that result in the formation of endothelial monolayers around the microchannels [58,59]. Micropatterned single planar layer substrates prepared in this way are compiled to form macro 3D tissue constructs. Because

the preparation and assembly of multiple layers is a time-consuming process, researchers have searched for alternative ways to fabricate 3D macro-sized substrates with microfluidic channels. Implementation of advanced technologies, such as direct write assembly (robotic deposition, fused deposition, and two-photon polymerization) [60], sacrificial material-based extrusion printing [21], modular assembly [61], omnidirectional printing (Figs. 5A–F) [62], and electrostatic discharge printing (Figs. 5G and H) [63] have demonstrated unprecedented success in generating complex 3D vascular patterns. Such complex patterns are often embedded in hydrogel-containing tissue-specific cells.

The success of microfluidics networks in terms of vasculature formation largely depends on the mechanical and biological properties of the biomaterial. A wide range of synthetic polymers, including poly(methylmethacrylate), poly(dimethyl siloxane), silicon, polycarbonate, polyvinyl chloride, polystyrene, poly(lactic-co-

glycolic) acid (PLGA), and poly(glycerol sebacate) have been used in microfluidics [64]. However, EC monolayers grown into micro-patterned synthetic substrates show poor barrier function in terms of transporting biomolecules, oxygen, and nutrients. Because patterned synthetic materials show poor biodegradation, barrier function, and biocompatibility and provoke cytotoxicity and inflammatory responses *in vivo*, researchers have explored a wide range of hydrogels for printing micropatterns for vasculature formation. A number of studies have used silk fibroin, Matrigel, type I collagen, and fibrin to form endothelial tubes in 3D scaffolds [65]. By nature, these hydrogels are biodegradable and biocompatible and can provide a 3D milieu for vascular network formation. In addition to the biomaterials, several parameters have been identified as potential factors in generating microvessels with microfluidics. For example, the combined effect of microfluidics and vasculogenesis from cell seeding grew perfusable and functional microvessels in a 3D fibrin gel system *in vitro* and showed strong barrier function and long-term stability [66]. Similarly, the collective effects of growth factors and fluid shear stress have also been investigated, with gradients of vascular endothelial growth factor (VEGF) and angiopoietin 1 (ANG-1) forming a stable and

connected 3D capillary network within a type-I collagen matrix embedded with microfluidic channels [67]. The success of such a strategy led researchers to further explore the synergistic effect of multiple parameters to promote and regulate capillary formation in a 3D microfluidics-hydrogel system. Co-culture of HUVECs and human lung fibroblasts (HLFs) in fibrin gels/microfluidics systems containing VEGF and sphingosine-1-phosphate (S1P) promoted the formation of a stable capillary network with smaller lumen diameters [68]. In addition, stem cell-incorporated gels/microfluidic systems have been investigated. For example, a co-culture of HUVECs and MSCs in a collagen gel/microfluidic system reduced capillary formation, but stabilized the newly formed capillaries [69].

3.2. Micromodule assembly

The success of a macro-scale tissue engineered construct depends on several factors, including the availability of a mass diffusion network within 100–200 μm from the cell population, uniform distribution of multiple cell types with reasonable density, and nonthrombogenic phenotype of ECs upon integration

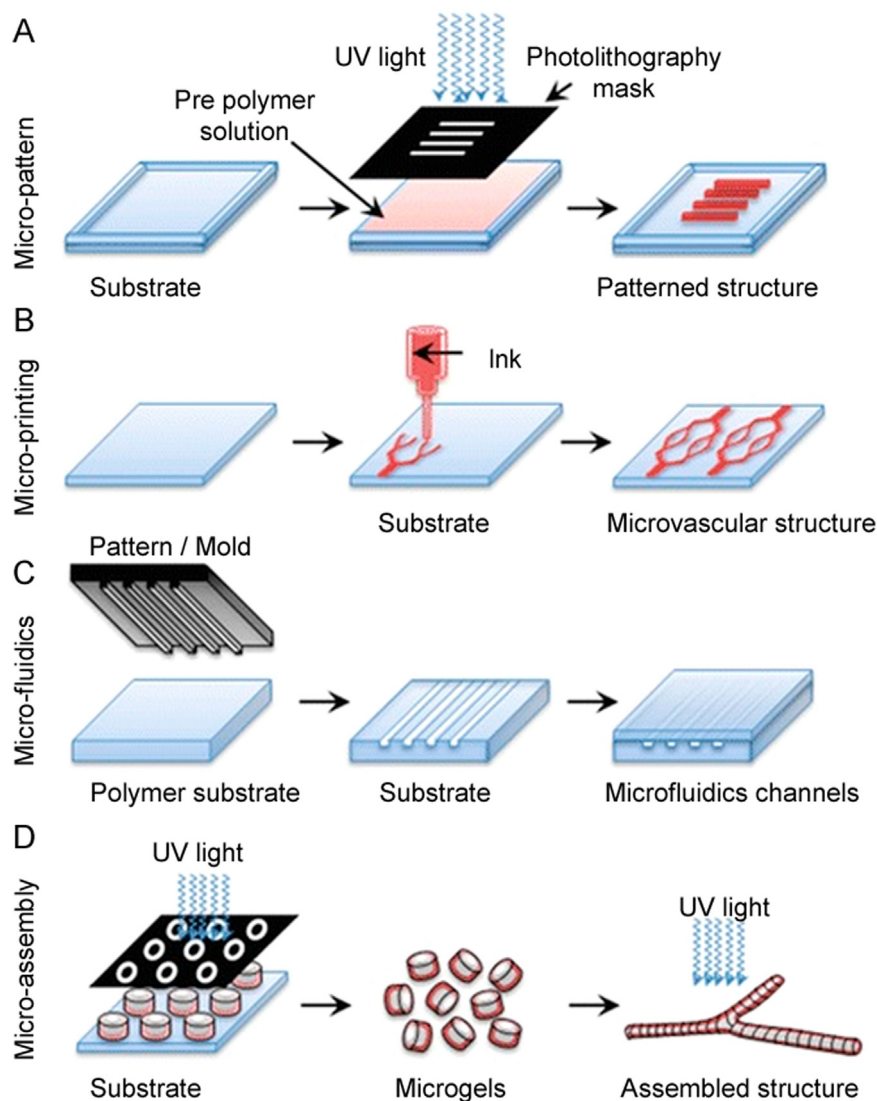


Fig. 4. Creation of a capillary bed-like structure mimicking native tissue: (A) fabrication of a micro-scale structure using a soft lithographic technique, (B) microprinting using conformational contact to form a pattern of ink on the surface, (C) microfluidic channels fabricated using micromolds (channels are used to form microfibers of a sacrificial substance that is then removed to form hollow fibers), and (D) complex vascularized structures fabricated using an assembly of microgels (reproduced with permission from [53]).

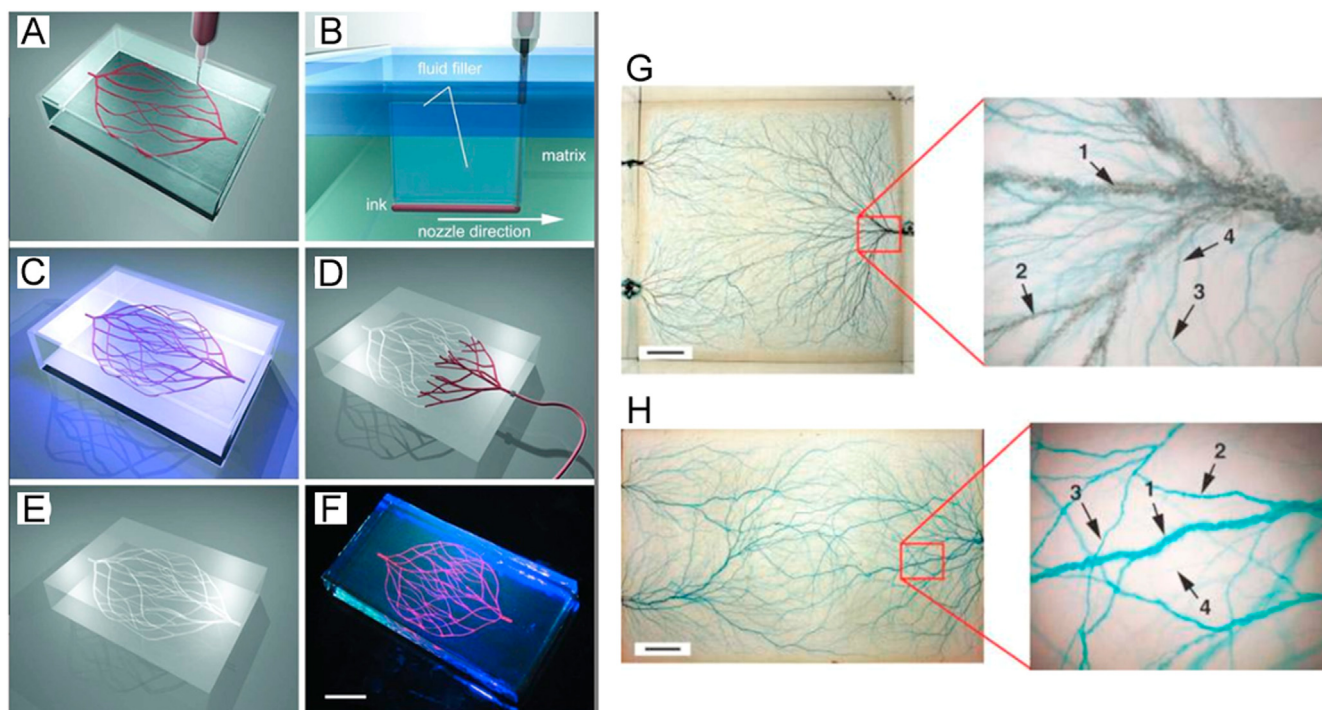


Fig. 5. Schematics of omnidirectional and electrostatic discharge fabrication of 3D microvascular networks: (A) extrusion of a fugitive ink into a gel in a hierarchical fashion, (B) migration of fluid from capping layer to the voids generated by nozzle translational speed, (C) photopolymerization of hydrogel matrix, (D and E) microvascular channels that are created by dissolving and removing the fugitive ink under a modest vacuum, (F) fluorescent image of a 3D microvascular network (scale bar = 10 mm), (G) blue food-dye injected microvascular networks in an acrylic block with three fluidic access points (scale bar = 1 cm), and (H) branched microvascular networks embedded in a molded PLA block incorporated with a hierarchy of microchannel diameters (scale bar = 2 cm) (reproduced with permission from [62,63]).

with the host vasculature [4,70]. To address this issue, researchers have taken a bottom-up approach to fabricate macro-scale scaffolds, and found that self-assembled micro-tissues or -modules were a possible solution for fabricating large engineered constructs, as shown in Fig. 6. When such micro-modules are loaded into large tissue constructs, the micro-dimensions of these modules facilitate the diffusion of nutrients, oxygen, and essential biomolecules to the cell population embedded in the gels [71]. To date, several methods have been investigated to generate micro-tissues or -modules. Micro-scale molding and UV crosslinking, directed self-assembly, and gravity-enforced self-assembly approaches have frequently been used to build micro-scale modules [72–74]. During preparation, tissue-specific cells are often encapsulated in the micro-modules, while a confluent layer of HUVECs is provided to coat their outer surface [75]. In some studies, the outer surface was further coated with protein molecules before EC seeding to improve the biofunctionality. Fibronectin-coated micro-collagen modules implanted in mice formed more stable, mature, and perfused capillaries 14 days postoperatively compared to collagen modules without the fibronectin coating [76]. Further, EC-coated microgels embedded with stem or progenitor cells showed impressive results with respect to stabilizing the newly formed capillary blood vessels relative to EC-coated modules; for example, implanted EC-coated collagen micro-modules containing BMSCs in the omental pouch in rats formed less leaky and more dense and mature capillaries [77].

A number of studies have used random packing, directed, or sequential assembly to accumulate cell-loaded micro-modules with different sizes and shapes to prepare macro-scale vascularized tissue constructs [78,79]. In random packing, EC-coated modules are perfused with blood or culture medium that causes interconnected channel formation in the interstitial spaces of the modules. In directional assembly, shape-controlled microgels spontaneously form

offset, linear, branched, or random aggregates depending on surfactant concentration, aspect ratio, agitation rate, and time [79]. The sequential assembly approach was investigated in an effort to control the organization of the microgels having internal microchannels [80]. Such microgels were prepared with photolithography and then assembled into a tubular construct where an interconnected and bifurcated structure resembling native vasculature was formed. In particular, SMCs and HUVECs were incorporated in the outer and inner layer of the microgel to form a biomimetic 3D vasculature. Variables including the thickness and diameter of the microgels, swiping speed of the needle, concentration of surfactants, and space between two successive microgels affected the length of the assembled 3D tubular construct. Although sequential assembly is economical and applicable with respect to the formation of a complex vascular network, shortcomings associated with the fabrication of thick microgels ($\geq 600 \mu\text{m}$) containing non-straight vertical cross-sections and with thin microgels ($\leq 150 \mu\text{m}$) showing poor mechanical strength limit the application of this method [81]. Overall, vascularized tissue formed with the modular approach shows poor tissue integration and capillary network formation in vivo.

4. Nano-fabrication

In the past decade, researchers have focused on fabricating nanofiber-based vascular constructs because nanofibers possess similar topographical cues to ECM [82]. Using different electrospinning techniques, random, aligned, and core/shell nanofibers have been printed and nanofiber-based matrices studied for tissue vascularization. A wide range of synthetic and natural materials, including polycaprolactone (PCL), poly(L-lactic acid) (PLLA), PLGA, poly(ethylene oxide) (PEO), PVA, chitosan, gelatin, and collagen, have been explored for nano-fabrication applications [83].

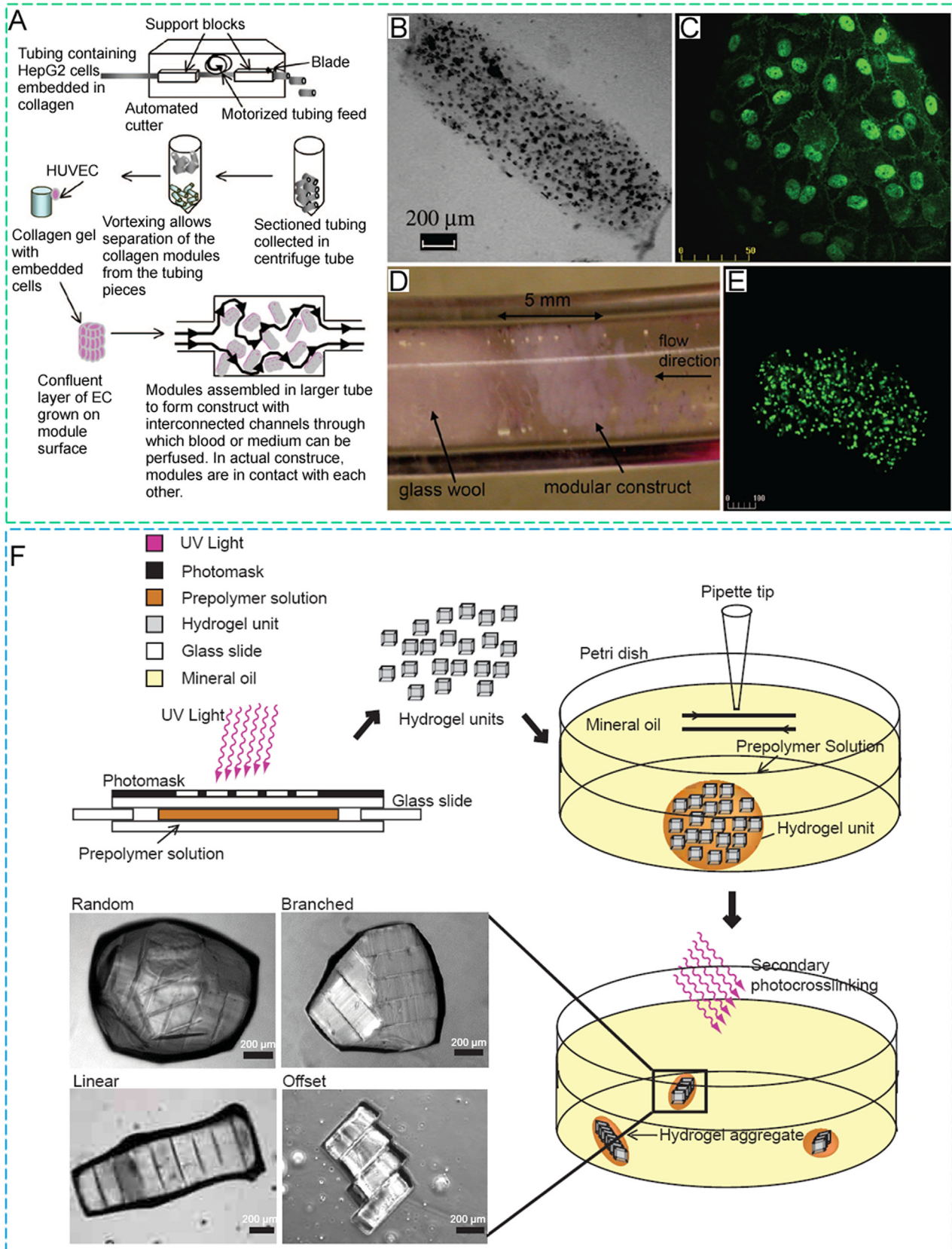


Fig. 6. Micromodule assembly: (A) collagen solution loaded with human hepatoma (HepG2) cells was gelled into ethylene oxide tube at 37°C for 30 min, the tube was then segmented into 2-mm length, and the collagen modules were collected after rotating in a centrifuge. Then HepG2 cell loaded modules were seeded with HUVECs, accumulated into a larger tube, and perfused with medium or blood, (B) light micrographic image of a collagen–HepG2 module without HUVECs, (C) confocal microscopic image of vascular endothelial (VE)-cadherin-stained module showing a confluent layer of HUVECs around the outer surface of module after 7 days of culture, (D) perfusion of a modular construct in a large tube with phosphate buffered saline (PBS), (E) confocal microscopic image of a collagen–HepG2–HUVEC module after 7 days of culture with HepG2 cells labeled with a Vybrant™ CFDA SE cell tracer kit, and (F) schematic diagram of the microgel assembly process (reproduced with permission from [75,79]).

Synthetic nanofibers show more mechanical stability compared to natural fibers, but hydrophobicity, the absence of cell binding motifs, and poor biodegradability limit their applications. Conversely, natural polymeric materials are hydrophilic, and biocompatible, and possess cell binding motifs, yet poor degradation and mechanical properties are major shortcomings that need to be overcome for nano-fabrication. To address these issues, researchers have explored composites, copolymers, and hybrid biopolymers to fabricate nano-fibers and achieved some remarkable successes in tissue vascularization [84]. In some studies, random or aligned fibers were effective in terms of vasculature formation. For example, when electrospun random PCL/collagen (rPCL/Col) and aligned PCL/collagen-PEO (aPCL/Col-PEO) nanofibers were implanted in the arterio-venous loop in rats, a larger number of blood vessels and better capillary density and branching hierarchy were seen in the rPCL/Col fiber-implanted group 8 weeks post-operatively compared to the aPCL/Col-PEO group. Moreover, rPCL/Col fibers facilitated the formation of small pore sized capillaries, whereas the aPCL/Col-PEO scaffold promoted early and evenly distributed blood vessels throughout the scaffold, resulting in a shorter prevascularization time [85]. Prevascularized and aligned nanofibers can also promote vascularization. Random or aligned poly (ϵ -caprolactone)/cellulose electrospun nanofibers have been used to fabricate a mesh structure in a layer-by-layer fashion. HUVECs seeded onto the aligned nanofibers promoted prevascularization in vitro compared to randomly oriented nanofibers by forming capillary-like structures. When the prevascularized and aligned nanofibers were implanted subcutaneously in rats, host blood vessels penetrated deep into the nano-meshes and integrated with the vascular network [86]. In an attempt to prevent thrombosis in a small-diameter blood vessel, graded chitosan/poly ϵ -caprolactone (CS/PCL) nanofibers fabricated with sequential co-electrospinning were heparinized to immobilize VEGF. HUVECs and SMCs were cultured on the top and bottom surfaces of the graded CS/PCL nanofibers, mimicking the lumen and adventitia of blood vessels, respectively. The graded and heparinized nanofibers demonstrated outstanding anti-thrombogenic properties. Further, better HUVEC attachment, proliferation, and monolayer formation have been identified on graded CS/PCL scaffolds compared to uniform CS/PCL scaffolds [87].

5. Creation of vascular networks with mechanical spacers

The shortcomings related to sacrificial filaments used to form microfluidic networks have led researchers to investigate alternative approaches. Incorporation of mechanical spacers into the 3D scaffold (Fig. 7) generates linear microchannels without causing any cytotoxicity. In particular, several studies have used mechanically removable spacers to create microchannels in a hydrogel matrix. In one study, linear wire arrays ranging from 152 to 787 μm in diameter were used to form microfluidic channels in a silk fibroin scaffold. Because the channels often lose uniformity after removal of the mechanical spacers, attempts have been made to introduce hollow tubes into the spacer-generated hollow channels. Hollow channels with open wall porosity, as well as silk tubes and porous silk tubes with incorporated channels were formed in the silk scaffolds, after which human arterial endothelial cells (hAECs) were seeded into the hollow channels in vitro with or without the presence of collagen-I or laminin. After 7 days of seeding, hAECs formed a nearly continuous layer around the spacer-generated hollow channel and ECM protein-loaded silk tubes [88]. Because the formation of confluent monolayers of ECs in spacer-generated hollow channels is difficult, researchers have attempted to transfer self-assembled

cell layers into the hollow channel to avoid the cell seeding approach. In one study, HUVECs were seeded on oligopeptide-adsorbed micrometric gold rods to form self-assembled monolayers (SAMs), and then the SAM-attached gold rods were encapsulated in photocrosslinked GelMA. The SAMs of ECs were transferred into the GelMA by applying an electrical potential, followed by the perfusion of SAM with medium at 2 $\mu\text{L}/\text{min}$. This approach was further explored to transfer double layers of assembled cells from gold rods into GelMA to mimic native blood vessels. To form double layers of vascular cells, HUVEC-coated gold rods were dipped into GelMA solution containing NIH 3T3 fibroblast cells, and then encapsulated in the GelMA hydrogel. By applying an electrical potential, the double layers of assembled cells were transferred into the bulk gel, and then the layers were perfused with media for stabilization [31]. Although promising, mechanical spacers have not to date been able to generate complicated and branched structures that resemble native blood vessels.

6. Scaffolds with natural architecture

Tissue-specific acellular matrix contains biological, structural, functional, and topographical cues that promote vascular tissue growth through the upregulation of signaling pathways, phenotype, mechano-transduction, and differentiation and proliferation of the repopulated vascular cells [89,90]. Different studies have prepared decellularized vascular tissue with chemical (acid, base, detergent, hypotonic and hypertonic solutions), biological (e.g. trypsin, dispase, etc.), or physical (e.g. temperature, pressure, electroporation, agitation, pressure gradient, etc.) agents in consideration of tissue properties (e.g. size, lipid content, density, thickness, cellularity, etc.). However, such processes often disrupt the ultrastructure of ECM, remove ECM and growth factors, and provoke immune responses [91–93]. A number of studies have successfully grown functional macro blood vessels with decellularized matrix. For example, in one study a recellularized tissue-engineered vessel with autologous EPCs prevented clotting and intimal hyperplasia for 30 days in a porcine model [94]. When decellularized rat iliac arteries seeded with ECs were implanted in the abdominal aorta of rats, native vessel-like structures were observed at 3 months [95]. Similarly, the inner layer of decellularized pig arteries were repopulated with human ECs and implanted in the pigs as iliac artery substitutes; the inner layer of the recellularized matrix was covered by ECs, and no thrombi formation was reported 70 days postoperatively [96]. Apart from EC seeding, the success of decellularized matrix vascularization largely depends on the implementation of physical stimuli. For example, decellularized rat hearts were repopulated with cardiac cells or ECs, and then cultured in a bioreactor maintaining simulated cardiac physiology over 28 days. In both larger and smaller coronary vessels, EC layer formation was identified 7 days after recellularization. Interestingly, cell-seeded heart tissue showed contraction and expansion under electrical stimulation 8 days after cell seeding [97]. Decellularized cadaveric lungs containing intact internal structures (e.g. perfusable vascular network, airways, and alveolar geometry) were seeded with ECs and then cultured in a bioreactor simulating developmental physiological conditions. When such lungs were transplanted and perfused by the recipient's blood circulation in vivo, gas exchange was observed up to 6 h after extubation. However, the success of this approach largely depends on the use of progenitor cells, prolonged in vitro and in vivo culture, and an ideal post-operative ventilation regimen for the regenerated lungs [98].

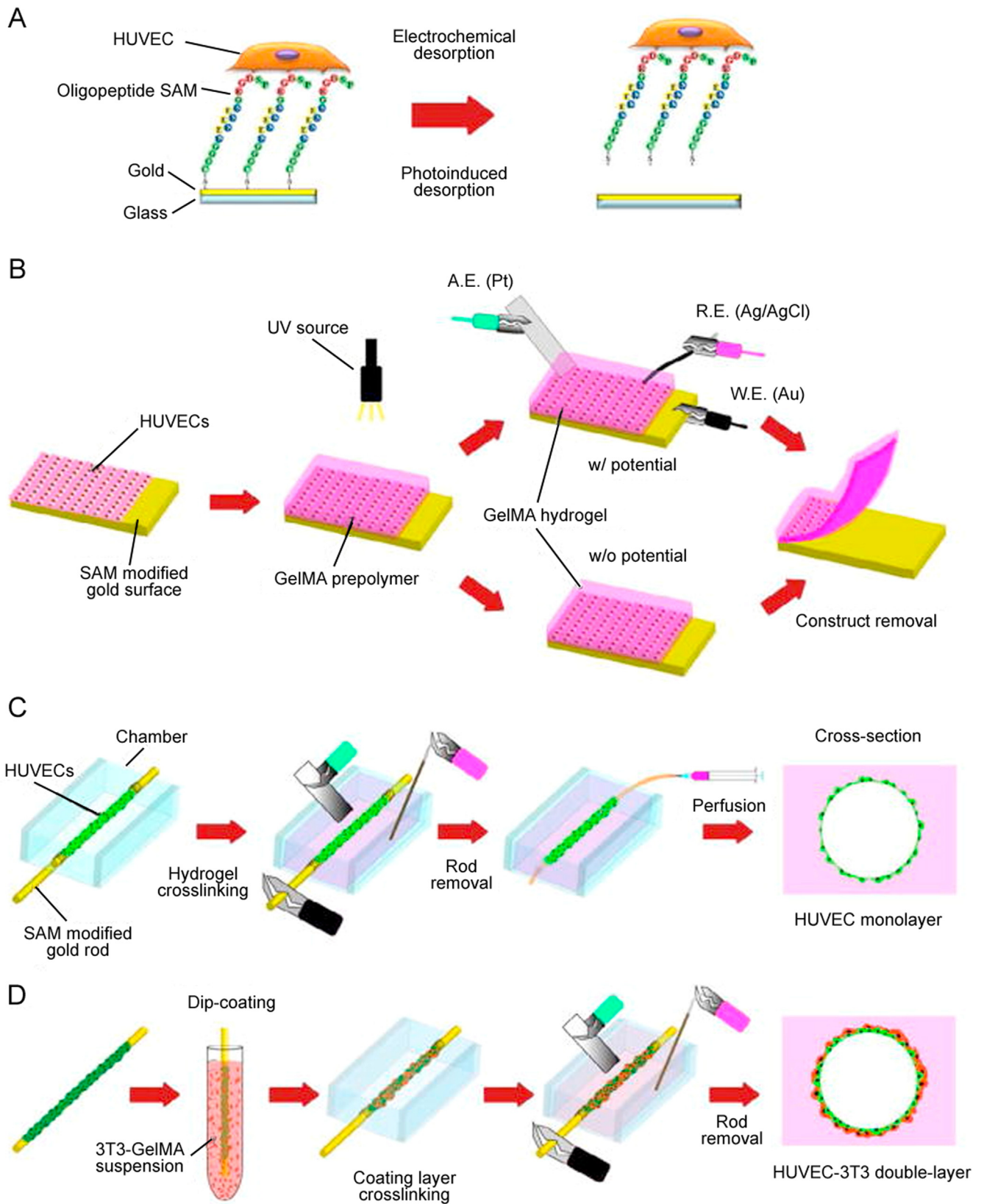


Fig. 7. Schematic of cell transfer, and vascular network formation mechanism by mechanical spacers: (A) oligopeptide modified gold surface was seeded with HUVECs, (B) HUVECs seeded on gold substrate were transferred to photocrosslinked GelMA hydrogel with or without electrical potential, (C) HUVECs coated micrometric gold rod was placed in a culture chamber and encapsulated in GelMA hydrogel, and the layer of HUVECs was transferred to GelMA by using an electrical potential. Then the rod was taken out and the hollow lumen was cultured under perfusion, and (D) HUVECs coated gold rod was dipped into 3T3 fibroblast cell loaded GelMA solution to form double-layered microvascular structures. The rod was then encapsulated in hydrogel, the double-layer of vascular cells was transferred by an electrical potential, the rod was removed, and the hollow channel was cultured under perfusion (reproduced with permission from [31]).

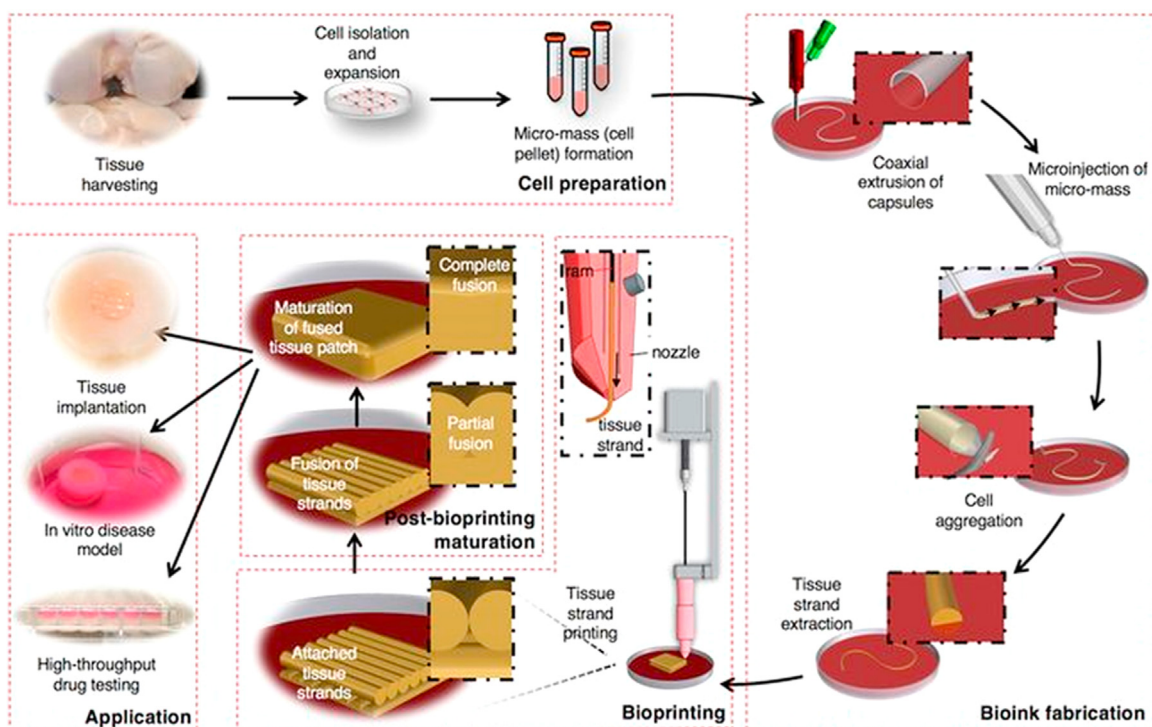


Fig. 8. Schematic elucidating the concept of tissue printing using tissue strands as a new bioink (reproduced with permission from [102]).

7. Biopolymer-free fabrication

7.1. Cell aggregates as bioink

In vivo, tissues or organs develop due to the self-assembly and self-organization of multiple cell types without the influence of scaffolds. Although it was established decades ago that tissue regeneration requires engineered constructs, several complexities related to the scaffolding biomaterial have led researchers in recent years to harness the in vivo mechanism of tissue regeneration. A number of studies report that bioprinted cell aggregates form pre-designed tissue constructs through self-organization and tissue fusion [99]. Cell aggregates composed of single cell or multiple cell types can be bio-printed as cell pellets, tissue spheroids, or tissue filaments (Fig. 8). Tissue spheroids must be prepared in a controlled fashion to avoid clogging and cell damage in the bioprinting process [100]. In contrast, bioprinting of cell pellets ensures high cell densities and does not cause nozzle clogging or cell damage. However, bio-dispensing of cell pellets requires a supportive hydrogel in which they can accumulate, organize, and fuse to form tissue [101]. Tissue strands can also be formed by injecting cell pellets into tubular molds prepared with a co-axial nozzle system. In one study, injected cell pellets in permeable alginate capsules organized and fused to form tissue strands in an in vitro culture. Tissue strands were loaded into a custom-made bioplotter and then extruded layer-by-layer to form a pre-defined 3D structure [102]. These cell aggregate approaches can be applied to form tissue with vascular networks.

7.2. Rolled up cell sheet

In recent years, a number of studies have printed cell aggregates instead of 3D tissue scaffolds to create vascularized functional tissue, as scaffolding material inhibits cell-cell interactions and causes various complexities including inflammation, cytotoxicity, and tissue remodeling. In the cell sheet technique,

tissue-specific cells are cultured on a temperature-responsive material to create a cell-ECM matrix. To form vascularized tissue, a single monolayer sheet of ECs can be stacked with cell sheets of interest in a sandwich fashion or vascular cells can be co-cultured with tissue-specific cells to form vascularized multiple cell sheets. As an illustration, Fig. 9 shows an overall experimental scheme for fabricating an hMSC-based scaffold-free tissue engineered blood vessels. In general, cell sheets can be attached and detached from a temperature-responsive culture dish incubating at either a higher (37 °C) or lower temperature (< 25 °C). Nanometer-scale coating of poly(*N*-isopropylacrylamide) on polystyrene tissue culture surfaces facilitates attachment and detachment of endothelial cells and hepatocytes by shifting from hydrophobic to hydrophilic conditions at temperatures below 25 °C [103]. Vascularized cell sheets prepared in this way can be compiled to form thick tissue. For instance, triple-layered cell sheets were produced from co-culture of endothelial and cardiac cells overlaid on a resected tissue containing a vascular bed and perfused in a bioreactor. After 3 days of perfusion culture, ECs formed luminal capillaries throughout the cardiac sheet upon connection with the vascular bed. The triple-layered vascularized cardiac tissues prepared in this way could beat and were transplantable. For increased tissue thickness, a six-layered cell sheet was prepared by compiling either two triple-layered or six single-layered cell sheets together and then the stack overlaid on the vascular bed. The combined two-triple layered sheets created thicker cardiac tissues with greater cell density compared to the compiled six-layer sheets due to improved cell viability and vascularization [104]. Further, functional and vascularized tissue was obtained with 12 stacked cell sheets, indicating the efficacy of this approach to create vascularized thick tissue in vitro. Multiple transplantation of thin (~ 80 μm) cardiac cell sheets in vivo has also been found effective with respect to developing thick (~ 1 mm) vascularized tissues. In one study, cell sheets grown from neonatal rat cardiomyocytes were repeatedly transplanted into rats at 1-, 2-, or 3-day intervals. This poly-surgical approach created a thick (~ 1 mm), well-

vascularized, and perfused myocardium tissue [105]. Although vascularized tissue formation is possible with cell sheets, poor mechanical strength and tissue integrity of stacked cell sheets are major challenges that require further research.

8. Scaffold pre-vascularization

A macro-scale tissue engineered construct containing a large cell population requires a sufficient supply of nutrients, oxygen gas, and biomolecules to maintain the metabolic activity, viability, and proliferation of embedded/seeded cells. In vitro, tissue scaffolds featuring a microfluidic network can be perfused with culture media to supply the necessary elements to the large cell population. However, the situation becomes complicated when scaffolds are implanted in vivo. Extrinsic vascular networks develop in the tissue construct by angiogenesis and vasculogenesis mechanisms that take time. This time delay can cause ischemia in the large embedded cell population in a scaffold, and reduce cell viability by triggering apoptosis or necrosis. To address this issue, researchers have incorporated a microfluidic network into the tissue graft and then formed a monolayer of ECs by seeding (Fig. 10). Such microfluidic network-embedded grafts were then sutured with host arteries/veins during in vivo implantation. Because thrombopoiesis-induced restenosis is often seen in tiny blood vessels, nutrient supply throughout the scaffold might be hindered due to the blockage of the microfluidic network in vivo. Therefore, different studies have adapted several techniques to prevascularize the engineered construct, and then seed the graft with multiple cell types. In particular, scaffolds loaded with microvessel fragments, angiogenic factors, or vascular cells (ECs, SMCs) have been cultured in vitro or in vivo (e.g. arterio-venus loop) to form vascular networks prior to tissue-specific cell seeding [107,108]. The prevascularized grafts take less time to inoscultate with host vasculature, and thus support tissue growth, modeling, and integration. For example, when prevascularized collagen grafts seeded with fibroblasts, keratinocytes, and ECs were transplanted into mice, it took only 4 days to anastomose with host capillaries. In contrast, non-prevascularized scaffolds took 14 days to perfuse with native blood vessels [109]. In a co-culture system, prevascularization of tissue grafts largely depends on media composition, cell seeding technique, and ratio of

multiple cell types. In a multiculture system, tri-culture of myoblasts, fibroblasts, and endothelial cells at certain ratios enhances capillaries compared to co-culture of myoblasts and endothelial cells after 4 weeks of culture [110]. Furthermore, the tri-culture graft incubated with VEGF grew more blood vessels compared to those incubated with PDGF after 2 weeks of in vitro culture. While these cell-incorporated scaffolds achieved significant success in terms of prevascularization, formation of rapid, dense, mature, and functional capillary beds remains challenging. Apart from in vitro prevascularization, scaffolds incorporating microvessel fragments have been used as prevascularized constructs. In fact, these ECM matrices contain tissue-specific bio-chemical and topographic cues that regulate numerous cell-functions to form functional capillary beds. Implanted collagen gel containing microvessel fragments in immunocompromised mice formed neovessels with lumen by day 11 and a mature functional microvascular bed by day 28 [111]. Although promising, allogeneic or xenogeneic microvessel fragments can cause immunological complexities in the host body. The success of in vitro prevascularization largely depends on the artificial physiological conditions applied during tissue culture. A number of studies maintained dynamic culture conditions including pulsation, variable flow rate, and dynamic pressure to form vascular networks. For example, cyclic mechanical strain and stress for 8 weeks promoted the proliferation, alignment, and collagen production of rabbit aortic SMCs seeded onto poly(L-lactide-co-caprolactone) (PLCL) scaffolds [112]; dynamic sequential seeding of aortic SMCs and ECs onto poly(glycolic acid) (PGA) scaffolds and biomechanical stimulation for 25 days enhanced capillary formation and ECM deposition [113]; and a controlled hypoxic environment influenced cells to secrete VEGF, which promoted vascularization in vitro [114]. However, modulation of oxygen concentration in a co-culture system can alter the differentiation of stem cells into different lineages [115]. Moreover, bidirectional flow in the biaxial bioreactor of a co-culture system (e.g. EPCs and MSCs) significantly reduces hypoxia-induced VEGF expression by eliminating the oxygen gradient. Thus, blood vessel formation is hindered in a bidirectional flow system compared to static culture and unidirectional flow systems [116].

In vitro tissue prevascularization requires well-connected and porous scaffolds, microfluidic networks, complex bioreactors, and culture media; however, the long-term fate of the capillary bed formed remains unknown. To address this issue, researchers have

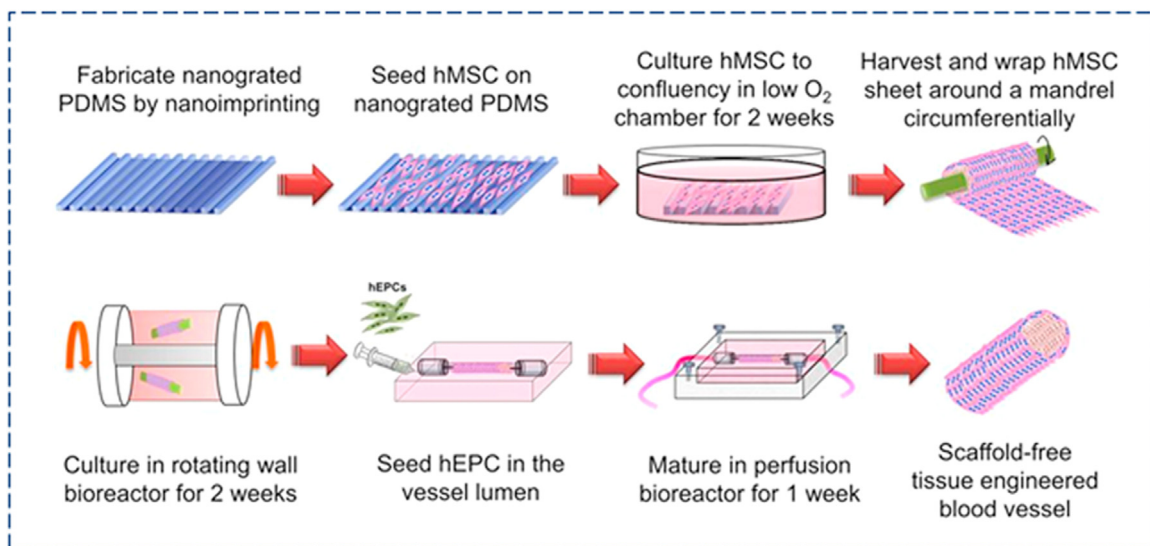


Fig. 9. Vasculature formation with cell sheets: scaffold-free fabrication approach of hMSC-based tissue engineered blood vessel (TEBV), incorporation of human EPC in the vessel lumen, and culture and maturation of TEBV in a perfusion bioreactor (reproduced with permission from [106]).

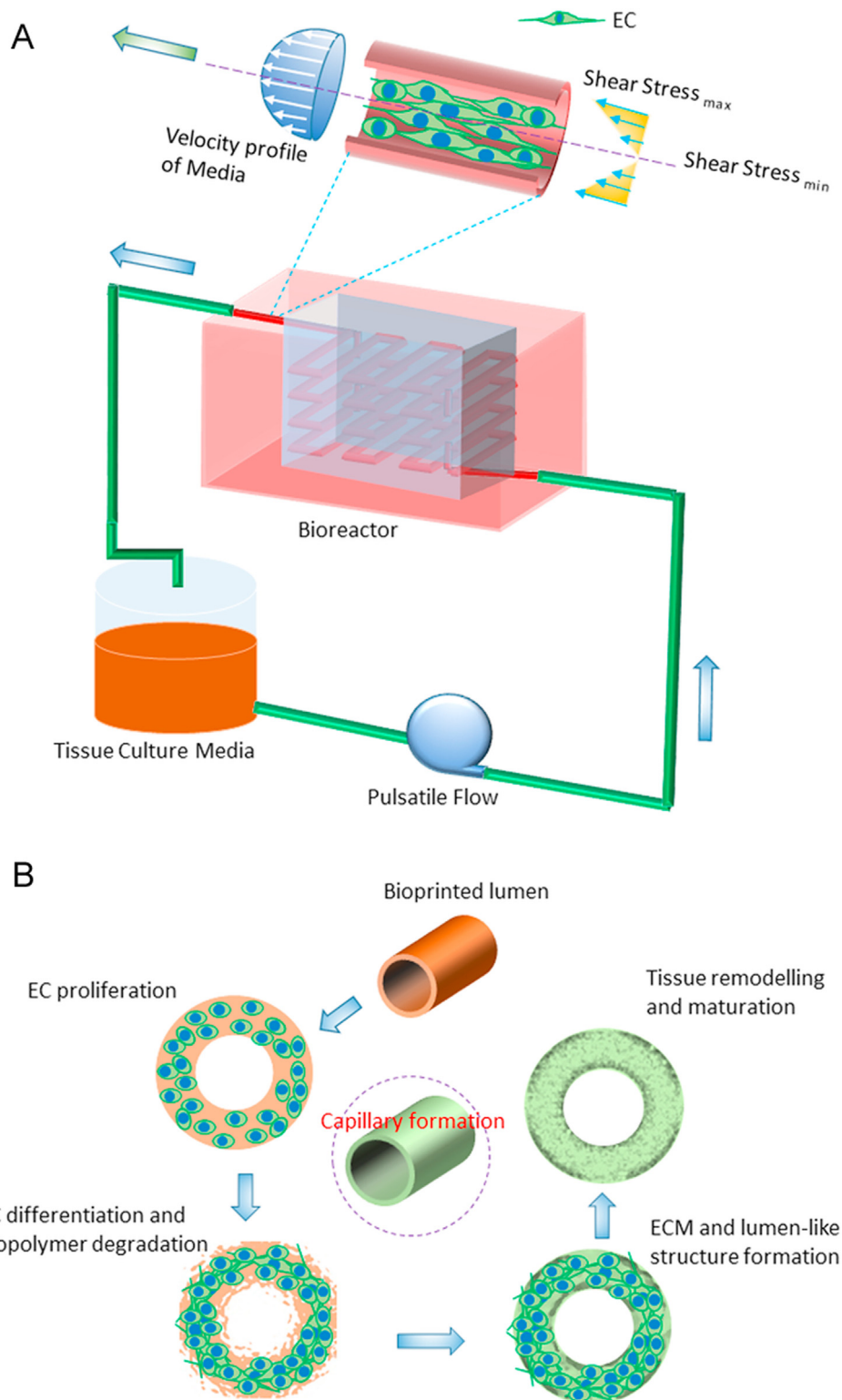


Fig. 10. Mechanism of blood vessel formation and maturation within a scaffold cultured in a bioreactor: (A) effect of shear stress on ECs and (B) step-wise demonstration of blood vessel formation by ECs in a scaffold.

paid attention to *in vivo* prevascularization of engineered constructs. In this approach, cell/angiogenic factor-loaded tissue constructs are implanted into a temporary site within the host body, and then transplanted into a specific location. In the case of angiogenic factor-embedded scaffolds, angiogenic sprouting takes place due to the controlled release of VEGF. Because angiogenic

factors demonstrate short half-lives *in vivo*, autologous cells are incorporated in the scaffold to express VEGF. In particular, scaffolds are initially implanted close to an arteriovenous loop in the host body to promote vasculature [117]. When a well-perfused capillary bed is formed within the matrix after a certain time, scaffolds are explanted, seeded with multiple cell types, and then

transplanted into the target location. In one study, an FGF-2-enriched Matrigel chamber was implanted around the epigastric pedicle of a diabetic mouse. The Matrigel was replaced by highly vascularized adipose tissue after 21 days of culture. Seeding of pancreatic islets into the prevascularized chambers in diabetic mice significantly reduced the blood glucose levels, indicating the better survival and function of islets in the prevascularized chamber compared to non-prevascularized chambers [118]. Likewise, neonatal cardiac cells seeded onto prevascularized cardiac patches and transplanted onto infarcted rat hearts enhanced cardiac function after 28 days [107].

9. Summary and future research directions

The success of tissue and organ regeneration largely depends on the formation of a mature and well-perfused vascular network within the developing tissue. To date, significant progress has been achieved in the printing of vascular constructs (Table 1).

In recent decades, technological advancements in 3D bioprinting systems have made it possible to print cell aggregates, tissue strands, or cell/GF-loaded biomaterials layer-by-layer as per a predefined geometry developed by CAD software. In particular, inkjet- and 3D-bioplotting-based techniques have been recurrently used in different studies [119,120]. Each technique has advantages and drawbacks. For example, 3D inkjet printers are cheap and fast but can result in cell damage and clogged nozzles while 3D bioplotting is suitable for printing intricate networks with sacrificial materials but at the expense of printing resolution. Recently, bioplotting with a coaxial nozzle has attracted significant attention due to the ability to print capillary strands with lumen. Using microfluidics, EC monolayers can be developed inside the hollow strands. Over the last decade, the rapid advancement of laser technology has brought significant changes to 3D scaffold printing in terms of accuracy and resolution. The LGDW and MAPLE DW methods, as nozzle-free techniques, can handle high-viscosity bioink and pattern 3D vascular cells with high printing resolution and accuracy. Unfortunately, research in this direction has not advanced far because these techniques are time-consuming and cause significant cell damage during fabrication. In contrast, DLP and LS methods are comparatively biocompatible and capable of printing intricate architecture. The DLP technique can print 3D capillary networks promptly with high resolution, but the technique is costly, compromises details for a large construct, and causes resin cytotoxicity. In contrast, the LS approach (particularly two- or multi-photon laser systems) is capable of printing complicated 3D vascular patterns with details, although at a lower printing speed compared to the DLP technique. Nonetheless, the effect of the laser on cell damage remains controversial, and both LS and DLP techniques are only applicable to photo-crosslinkable hydrogels.

Based on an understanding of physiology, researchers have reached a common agreement that micro-scale capillary networks are needed to maintain the viability of large cell populations incorporated in engineered constructs. Different fabrication techniques have been applied to form capillaries and ECs have been seeded in the micro-lumen using microfluidic approaches. Plasma etching, laser ablation, soft lithography, and replica molding have been frequently used to generate patterned vascular networks on a single layer planar surface. Although capillary bed-embedded 3D tissue constructs can be constructed by stacking multiple single layers, assembling complexities and the requirements of long processing time limit their application. However, significant success in 2D capillary formation has been achieved when advanced computational approaches have been applied to manipulate the shear stress, medium circulation, and bio-molecule distribution in

micro-lumen seeded with ECs and mural cells. The success in 2D has been further translated to 3D microfluidic systems to promote EC monolayer formation on the lumen. To achieve a self-assembled capillary network rather than a pre-designed one, EC-coated micromodules containing tissue-specific cells have been loaded into engineered constructs and then perfused with medium in a bioreactor. Unfortunately, this approach grows vascular networks that are dissimilar to those of native tissue and demonstrate poor tissue integration. In recent years, the introduction of omni-directional printing has enabled the fabrication of native tissue-like capillary networks instead of 3D periodic lattice structures. This approach needs further improvement as inefficient removal of pluronic acid can significantly reduce EC viability. Similarly, highly branched or fractal-like structures have been generated in plastic materials with high energy electron beam irradiation. This approach is suitable for post EC seeding, while tissue-specific cell incorporation in the plastic material requires further study. Linear channels with varying diameter and linear 3D patterns have also been generated, with double layers of vascular cells transferred in the hydrogel using mechanical spacers. However, the capillary vessels formed by mechanical spacers are not continuous and cannot mimic the native vascular network.

To date, the formation of micro-capillary beds in developing tissue remains challenging. ECM-cell interactions are essential in vasculogenesis and angiogenesis processes, where ECM features a specific geometry close to that of nano-filaments. Therefore, researchers have recently conducted several experiments to form micro- and macro-blood vessels using nanofiber-based engineered constructs. Structures similar to native blood vessels containing lumen and adventitia have been grown by seeding cells on nanofiber-made tubular structures. Likewise, micro-capillaries have been successfully grown in implanted nano-filaments.

Efforts have also been made to vascularize tissue with decellularized matrix, which contains all of the necessary biological and biophysical cues for capillary formation. Because the approach is related to the decellularization and recellularization methods, destruction of proteins, difficulties in cell removal and seeding, and aggravation of immunological complexities are quite common outcomes. However, several studies have reported outstanding results in terms of vascular network formation and research is continuing to address the shortcomings of this approach.

While artificial structures have shown substantial progress with respect to generating vasculature, the long-term fate of such vascularized tissue remains controversial. The tissue forming mechanism in the embryonic stage suggests that cells are capable of creating their own matrix, and incorporation of foreign material in the tissue significantly impedes cell-cell interactions. Inspired by the theory, several studies have recently been conducted based on the scaffold-free approach. In recent times, macro-scale blood vessels have been grown successfully by dispensing cell aggregates and sacrificial material, and micro-patterned structures have been printed using tissue strands. Likewise, capillary vessel-embedded cell sheets are prepared and outstanding blood perfusion has been reported *in vivo*. Repeated implantation in multiple surgeries has been found to enhance the development of vascularized thick tissue with thin cell sheets. The mechanical stability of such self-assembled structures is a major issue that needs to be further addressed.

One of the major problems of culturing macro-scale tissue constructs is the development of tissue ischemia, which triggers necrosis and apoptosis in the large embedded cell population in the scaffold. In this regard, the strategy of adding cells to the *in vitro* or *in vivo* prevascularized construct has proven effective in terms of obtaining better cell viability compared to non-prevascularized constructs. The requirement of multiple surgeries for prevascularization and for biodegradable filaments need to be addressed to make the approach applicable to vasculature

Table 1
Fabrication of vascular networks using different techniques for tissue engineering applications.

Fabrication technique	Biopolymer	Scaffold geometry	Embedded cells and other factors	In vitro/In vivo	Study period	Results of vascularization	Ref.
Ink-jet printing (HP Desk-Jet 550C printer)	Alginate-collagen	3D pie construct (~ 7 mm in diameter), and rectangular samples (2.5 cm × 0.5 cm × 0.3 cm)	Canine smooth muscle cells, human amniotic fluid-derived stem cells, and bovine aortic endothelial cells	In vivo: pie shaped scaffolds were implanted subcutaneously into the backs of outbred athymic nude mice	Up to 18 weeks	Vascularized, mature, and functional tissues	[17]
Ink-jet printing (HP Desk-jet 500 printer and HP 51626A cartridges)	Fibrinogen and thrombin	Around 9 mm × 1.8 mm rectangular scaffolds	HMVECs	In vitro: The patterns were then cultured at 37 °C with 5% CO ₂	Up to 21 days	Cells were seen to align, proliferate, and form a capillary-like tubular structure inside the channels	[18]
Extrusion-based printing	Carbohydrate glass encapsulated in the agarose, alginate, fibrin, Matrigel, and poly(ethylene glycol)-based hydrogel	Rectangular structure (20 mm × 10 mm × 2.4 mm); varying filament diameters (150–750 μm)	Primary rat hepatocytes, fibroblast cells, and HUVECs	HUVECs were seeded in the micro-lumen by injection method; channels were perfused with blood in vivo	Varying by experiment (up to 9 days)	Supported the metabolic function of primary rat hepatocytes by maintaining higher albumin secretion and urea synthesis than gels without channels	[21]
Extrusion-based printing	GelMA and fugitive ink (Pluronic F127)	200–300 μm thick	Human neonatal dermal fibroblasts, 10T1/2 fibroblast, and HUVECs	In vitro	Up to 7 days	HUVECs showed greater than 95% viability and formed a confluent layer around the lumens after 48 h	[22]
Extrusion-based printing	Alginate-PVA	Inner diameter of channels: 150–450 μm; Strand diameter: 400–1190 μm	hBMSC	In vitro	14 days	Excellent attachment and spreading of hBMSCs on the outer and inner walls of the hollow fibers	[26]
Laser-based printing	Polyester urethane urea (PEUU)	Two layers of HUVECs were printed following orthogonal grid pattern with 900 μm grid-line distance; two layers of hMSCs were printed at right angles with 600 μm side length between the HUVEC lines; 300 μm thick cardiac patch made of PEUU was sliced to circles of 8 mm diameter	HUVECs and hMSCs	In vitro and in vivo, patches were transplanted to the infarcted zone of rat hearts after ligation of left anterior descending coronary artery	8 weeks	An increased capillary vessel density and functional improvement of infarcted hearts was reported	[32]
Laser-based printing: projection stereolithography	GelMA	3D rectangular scaffolds (5 mm × 5 mm × 1 mm)	HUVECs	In vitro	7 days	Even distribution and proliferation of the HUVECs in the scaffolds caused high cell density and confluency as well as improved biological functionality	[36]
Laser-based printing: stereolithography, DLP technique	GelMA and poly(ethylene glycol) diacrylate (PEDGA)	Different micro-structured wells including stepwise, spiral, embryo-like and flower-like wells	HUVECs and NIH-3T3 fibroblast	In vitro	4 days of culture	Scaffolds enhanced cell-cell interactions and multicellular organizations; HUVECs aligned around the boundary of the fabricated geometry and formed cord-like structures	[37]

Laser-based printing: stereolithography (LS and 2PP techniques)	Polytetrahydrofuran ether-diacrylate	Tubes and branched tubular structure with a diameter smaller than 2 mm	Human dermal fibroblasts	In vitro	48 h after cell seeding	Grafts demonstrated good cyto-compatibility, and mechanical properties similar to native capillaries	[42]
Laser-based printing: stereolithography (2PP technique)	Photosensitive organically modified ceramics	Epoxy-based acellular micro-capillary vascular tree with μm features	Granulosa cells	In vitro	Up to 4 days	Improved cell growth and sustained cell-cell junctions	[43]
Micro-patterning/micro-fluidics	Collagen hydrogels of various stiffness	Hydrogel-based scaffold	Bovine pulmonary microvascular ECs	In vitro	–	ECs formed thicker and deeper vascular networks in the rigid gel than in the flexible gel; the lumen size of the capillaries grew in the rigid gel was larger than in the flexible gel	[47]
Micromodule assembly	Collagen modules and fibronectin-coated collagen modules	Micromodule with 760 μm internal diameter	HUVECs	In vivo and in vitro; modules were injected subcutaneously on the back of mice using 18 gauge needles and implanted through a micropipette in a subcutaneous pocket	In vivo: 7, 14, and 21 days; In vitro: 42 days	Coated collagen modules had more stable, mature, and perfused capillaries than sole collagen modules	[76]
Nano-fabrication	Random PCL/collagen and aligned PCL/collagen-PEO nanofibers	Average thickness, pore size, and filament diameter of randomly spun scaffolds are 300 μm , 1.2 μm , and 250 nm \pm 73 nm, respectively	–	In vivo: implantation inside the arterio-venous loop in rats (male Lewis)	8 weeks	A larger number of blood vessels, capillary density, and branching hierarchy were observed in random vs. aligned nanofibers	[85]
Vascular network by mechanical spacer	Silk fibroin, collagen-I, and laminin	Linear wire array ranging from 152 to 787 μm in diameter	hAECs	In vitro	7 days	Cells formed a nearly continuous layer around the spacer-generated hollow channel and ECM protein-loaded silk tubes	[88]
Scaffolds with natural architecture	Decellularized rat iliac arteries	–	ECs	In vivo: implantation in the abdominal aorta of rats	3 months	Native vessel-like structure was observed	[95]
Custom-made bioplotter and co-axial printer	Tubular alginate capsules and cell aggregate as bioink	Around 8-cm long tissue strands, 3 mm \times 3 mm tissue patch	Primary chondrocytes	In vitro: a bovine in vitro cartilage defect model (square chondral defects)	up to 4 weeks	A significant amount of cartilage ECM was found around tissue strands over time, and this approach can be used to form vascularized tissue	[102]
Molding	Alginate, Matrigel	Diameter, thickness, and average pore size of cardiac patch were 5 mm, 2 mm, and 100 μm , respectively	Neonatal rat cardiac cells	In vitro culture, in vivo pre-vascularization of cardiac patch onto rat omentum, and transplantation onto the infarcted rat hearts	28 days post-transplantation	Cardiac patch showed structural and electrical integration with native tissue as well as prevented dilatation and ventricular dysfunction of rat heart	[107]

formation. The future success of this approach requires improvements in terms of bioreactor design, culture and conditioning, cell seeding, microfluidics, and the need for multiple surgeries.

It is anticipated that a combined inkjet and 3D bioplotter bioprinting system will eventually emerge as a smart approach for printing cell aggregates, tissue strands, and capillary network simultaneously to form a complex vascularized tissue or organ.

Conflicts of interest

The authors declare that there are no conflicts of interest.

Acknowledgments

This work was financially supported by the Natural Sciences and Engineering Research Council of Canada [NSERC RGPIN-2014-05648].

References

- M. Nomi, A. Atala, P. De Coppi, et al., Principals of neovascularization for tissue engineering, *Mol. Aspects Med.* 23 (2002) 463–483.
- M. Sarker, S. Naghieh, A.D. McInnes, et al., Strategic design and fabrication of nerve guidance conduits for peripheral nerve regeneration, *Biotechnol. J.* 13 (2018) e1700635.
- B. Frerich, N. Lindemann, J. Kurtz-Hoffmann, et al., In vitro model of a vascular stroma for the engineering of vascularized tissues, *Int. J. Oral Maxillofac. Surg.* 30 (2001) 414–420.
- M. Sarker, X.B. Chen, D.J. Schreyer, Experimental approaches to vascularisation within tissue engineering constructs, *J. Biomater. Sci. Polym. Ed.* 26 (2015) 683–734.
- J. Folkman, P.A. D'Amore, Blood vessel formation: what is its molecular basis? *Cell* 87 (1996) 1153–1155.
- W. Risau, I. Flamme, Vasculogenesis, *Annu. Rev. Cell Dev. Biol.* 11 (1995) 73–91.
- S. Soker, M. Machado, A. Atala, Systems for therapeutic angiogenesis in tissue engineering, *World J. Urol.* 18 (2000) 10–18.
- S. Naghieh, E. Foroomezeh, M. Badrossamay, et al., Combinational processing of 3D printing and electrospinning of hierarchical poly(lactic acid)/gelatin-forsterite scaffolds as a biocomposite: mechanical and biological assessment, *Mater. Des.* 133 (2017) 128–135.
- S. Naghieh, M. Badrossamay, E. Foroomezeh, et al., Combination of PLA micro-fibers and PCL-gelatin nano-fibers for development of bone tissue engineering scaffolds, *Int. J. Swarm Intell. Evol. Comput.* 06 (2017) 1–4.
- M. Kharaziha, M.H. Fathi, H. Edris, Tunable cellular interactions and physical properties of nanofibrous PCL-forsterite: gelatin scaffold through sequential electrospinning, *Compos. Sci. Technol.* 87 (2013) 182–188.
- Y. Hosseini, R. Emadi, M. Kharaziha, Surface modification of PCL-diopside fibrous membrane via gelatin immobilization for bone tissue engineering, *Mater. Chem. Phys.* 194 (2017) 356–366.
- S. Naghieh, M.R. Karamooz-Ravari, M. Sarker, et al., Influence of crosslinking on the mechanical behavior of 3D printed alginate scaffolds: experimental and numerical approaches, *J. Mech. Behav. Biomed. Mater.* 80 (2018) 111–118.
- M. Sarker, X.B. Chen, Modeling the flow behavior and flow rate of medium viscosity alginate for scaffold fabrication with a three-dimensional bioplotter, *J. Manuf. Sci. Eng.* 139 (2017) 081002.
- Z. Izadifar, T. Chang, W.M. Kulyk, et al., Analyzing biological performance of 3D-printed, cell-impregnated hybrid constructs for cartilage tissue engineering, *Tissue Eng. Part C Methods* 22 (2016) 173–188.
- F. You, X. Wu, N. Zhu, et al., 3D printing of porous cell-laden hydrogel constructs for potential applications in cartilage tissue engineering, *ACS Biomater. Sci. Eng.* 2 (2016) 1200–1210.
- M. Sarker, M. Izadifar, D. Schreyer, et al., Influence of ionic crosslinkers (Ca^{2+} / Ba^{2+} / Zn^{2+}) on the mechanical and biological properties of 3D bioprinted hydrogel scaffolds, *J. Biomater. Sci. Polym. Ed.* 29 (2018) 1126–1154.
- T. Xu, W. Zhao, J.-M. Zhu, et al., Complex heterogeneous tissue constructs containing multiple cell types prepared by inkjet printing technology, *Biomaterials* 34 (2013) 130–139.
- X. Cui, T. Boland, Human microvasculature fabrication using thermal inkjet printing technology, *Biomaterials* 30 (2009) 6221–6227.
- F. Yanagawa, S. Sugiura, T. Kanamori, Hydrogel microfabrication technology toward three dimensional tissue engineering, *Regen. Ther.* 3 (2016) 45–57.
- S. Naghieh, M.R. Karamooz-Ravari, M. Badrossamay, et al., Numerical investigation of the mechanical properties of the additive manufactured bone scaffolds fabricated by FDM: the effect of layer penetration and post-heating, *J. Mech. Behav. Biomed. Mater.* 59 (2016) 241–250.
- J.S. Miller, K.R. Stevens, M.T. Yang, et al., Rapid casting of patterned vascular networks for perfusable engineered three-dimensional tissues, *Nat. Mater.* 11 (2012) 768–774.
- D.B. Kolesky, R.L. Truby, A.S. Gladman, et al., 3D bioprinting of vascularized, heterogeneous cell-laden tissue constructs, *Adv. Mater.* 26 (2014) 3124–3130.
- Y. Zhang, Y. Yu, H. Chen, et al., Characterization of printable cellular microfluidic channels for tissue engineering, *Biofabrication* 5 (2013) 025004.
- S. Naghieh, M. Sarker, M. Izadifar, et al., Dispensing-based bioprinting of mechanically-functional hybrid scaffolds with vessel-like channels for tissue engineering applications – a brief review, *J. Mech. Behav. Biomed. Mater.* 78 (2018) 298–314.
- Y. Zhang, Y. Yu, I.T. Ozbolat, Direct bioprinting of vessel-like tubular microfluidic channels, *J. Nanotechnol. Eng. Med.* 4 (2013) 020902.
- Y. Luo, A. Lode, M. Gelinsky, Direct plotting of three-dimensional hollow fiber scaffolds based on concentrated alginate pastes for tissue engineering, *Adv. Healthc. Mater.* 2 (2013) 777–783.
- Y. Yu, Y. Zhang, J.A. Martin, et al., Evaluation of cell viability and functionality in vessel-like bioprintable cell-laden tubular channels, *J. Biomech. Eng.* 135 (2013) 91011.
- I.T. Ozbolat, Yin Yu, Bioprinting toward organ fabrication: challenges and future trends, *IEEE Trans. Biomed. Eng.* 60 (2013) 691–699.
- Q. Gao, Y. He, J.Z. Fu, et al., Coaxial nozzle-assisted 3D bioprinting with built-in microchannels for nutrients delivery, *Biomaterials* 61 (2015) 203–215, <http://dx.doi.org/10.1016/j.biomaterials.2015.05.031>.
- C. Norotte, F.S. Marga, L.E. Niklason, et al., Scaffold-free vascular tissue engineering using bioprinting, *Biomaterials* 30 (2009) 5910–5917.
- N. Sadr, M. Zhu, T. Osaki, et al., SAM-based cell transfer to photopatterned hydrogels for microengineering vascular-like structures, *Biomaterials* 32 (2011) 7479–7490.
- R. Gaebel, N. Ma, J. Liu, et al., Patterning human stem cells and endothelial cells with laser printing for cardiac regeneration, *Biomaterials* 32 (2011) 9218–9230.
- Y. Nahmias, R.E. Schwartz, C.M. Verfaillie, et al., Laser-guided direct writing for three-dimensional tissue engineering, *Biotechnol. Bioeng.* 92 (2005) 129–136.
- F.P. Melchels, J. Feijen, D.W. Grijpma, A review on stereolithography and its applications in biomedical engineering, *Biomaterials* 31 (2010) 6121–6130.
- N.J. Mankovich, D. Samson, W. Pratt, et al., Surgical planning using three-dimensional imaging and computer modeling, *Otolaryngol. Clin. North Am.* 27 (1994) 875–889.
- R. Gauvin, Y.-C. Chen, J.W. Lee, et al., Microfabrication of complex porous tissue engineering scaffolds using 3D projection stereolithography, *Biomaterials* 33 (2012) 3824–3834.
- A.P. Zhang, X. Qu, P. Soman, et al., Rapid fabrication of complex 3D extracellular microenvironments by dynamic optical projection stereolithography, *Adv. Mater.* 24 (2012) 4266–4270.
- J. Torgersen, X. Qin, Z. Li, et al., Hydrogels for two-photon polymerization: a toolbox for mimicking the extracellular matrix, *Adv. Funct. Mater.* 23 (2013) 4542–4554.
- J.W. Lee, G. Ahn, D.S. Kim, et al., Development of nano-and microscale composite 3D scaffolds using PPF/DEF-HA and micro-stereolithography, *Microelectron. Eng.* 86 (2009) 1465–1467.
- J.F. Xing, M.L. Zheng, X.M. Duan, Two-photon polymerization microfabrication of hydrogels: an advanced 3D printing technology for tissue engineering and drug delivery, *Chem. Soc. Rev.* 44 (2015) 5031–5039.
- M.B. Applegate, J. Coburn, B.P. Partlow, et al., Laser-based three-dimensional multiscale micropatterning of biocompatible hydrogels for customized tissue engineering scaffolds, *Proc. Natl. Acad. Sci. USA* 112 (2015) 12052–12057.
- W. Meyer, S. Engelhardt, E. Novosel, et al., Soft polymers for building up small and smallest blood supplying systems by stereolithography, *J. Funct. Biomater.* 3 (2012) 257–268.
- A. Ovsianikov, S. Schlie, A. Ngezhayay, et al., Two-photon polymerization technique for microfabrication of CAD-designed 3D scaffolds from commercially available photosensitive materials, *J. Tissue Eng. Regen. Med.* 1 (2007) 443–449.
- X. Zheng, H. Lee, T.H. Weisgraber, et al., Ultralight, ultrastiff mechanical metamaterials, *Science* (80-) 344 (2014) 1373–1377.
- C.P. Ng, C.-L.E. Helm, M.A. Swartz, Interstitial flow differentially stimulates blood and lymphatic endothelial cell morphogenesis in vitro, *Microvasc. Res.* 68 (2004) 258–264.
- A. Ueda, M. Koga, M. Ikeda, et al., Effect of shear stress on microvessel network formation of endothelial cells with in vitro three-dimensional model, *Am. J. Physiol. Circ. Physiol.* 287 (2004) H994–H1002.
- N. Yamamura, R. Sudo, M. Ikeda, et al., Effects of the mechanical properties of collagen gel on the in vitro formation of microvessel networks by endothelial cells, *Tissue Eng.* 13 (2007) 1443–1453.
- D.F. Weston, T. Smekal, D.B. Rhine, et al., Fabrication of microfluidic devices in silicon and plastic using plasma etching, *J. Vac. Sci. Technol. B Microelectron. Nanometer Struct. Process. Meas. Phenom.* 19 (2001) 2846–2851.
- Y.-K. Hsieh, S.-C. Chen, W.-L. Huang, et al., Direct micromachining of microfluidic channels on biodegradable materials using laser ablation, *Polymers* 9 (2017) 242.
- A.S. Hansen, N. Hao, E.K. O'shea, High-throughput microfluidics to control and measure signaling dynamics in single yeast cells, *Nat. Protoc.* 10 (2015) 1181–1197.

- [51] J. He, M. Mao, Y. Liu, et al., Fabrication of nature-inspired microfluidic network for perfusable tissue constructs, *Adv. Healthc. Mater.* 2 (2013) 1108–1113.
- [52] D. Lim, Y. Kamotani, B. Cho, et al., Fabrication of microfluidic mixers and artificial vasculatures using a high-brightness diode-pumped Nd: YAG laser direct write method, *Lab Chip* 3 (2003) 318–323.
- [53] C.W. Peak, L. Cross, A. Singh, et al., Microscale technologies for engineering complex tissue structures, in: *Microscale Technol. Cell Eng.*, Springer, 2016, pp. 3–25.
- [54] D.R. Myers, Y. Sakurai, R. Tran, et al., Endothelialized microfluidics for studying microvascular interactions in hematologic diseases, *J. Vis. Exp. JoVE* (2012).
- [55] S. Takayama, E. Ostuni, P. LeDuc, et al., Laminar flows: subcellular positioning of small molecules, *Nature* 411 (2001) 1016.
- [56] H. Kaji, G. Camci-Unal, R. Langer, et al., Engineering systems for the generation of patterned co-cultures for controlling cell–cell interactions, *Biochim. Biophys. Acta* 1810 (2011) 239–250.
- [57] Y. Tardy, N. Resnick, T. Nagel, et al., Shear stress gradients remodel endothelial monolayers in vitro via a cell proliferation–migration–loss cycle, *Arterioscler. Thromb. Vasc. Biol.* 17 (1997) 3102–3106.
- [58] J. Shao, L. Wu, J. Wu, et al., Integrated microfluidic chip for endothelial cells culture and analysis exposed to a pulsatile and oscillatory shear stress, *Lab Chip* 9 (2009) 3118–3125.
- [59] J.W. Song, W. Gu, N. Futai, et al., Computer-controlled microcirculatory support system for endothelial cell culture and shearing, *Anal. Chem.* 77 (2005) 3993–3999.
- [60] D. Theriault, S.R. White, J.A. Lewis, Chaotic mixing in three-dimensional microvascular networks fabricated by direct-write assembly, *Nat. Mater.* 2 (2003) 265–271.
- [61] A. Chen, T. Pan, Three-dimensional fit-to-flow microfluidic assembly, *Bio-microfluidics* 5 (2011) 46505.
- [62] W. Wu, A. DeConinck, J.A. Lewis, Omnidirectional printing of 3D microvascular networks, *Adv. Mater.* 23 (2011) H178–H183.
- [63] J. Huang, J. Kim, N. Agrawal, et al., Rapid fabrication of bio-inspired 3D microfluidic vascular networks, *Networks* 77845 (2009) 3567–3571.
- [64] C.-W. Tsao, Polymer microfluidics: simple, low-cost fabrication process bridging academic lab research to commercialized production, *Micro-machines* 7 (2016) 225.
- [65] B.M. Baker, B. Trappmann, S.C. Stapleton, et al., Microfluidics embedded within extracellular matrix to define vascular architectures and pattern diffusive gradients, *Lab Chip* 13 (2013) 3246–3252.
- [66] S. Kim, H. Lee, M. Chung, et al., Engineering of functional, perfusable 3D microvascular networks on a chip, *Lab Chip* 13 (2013) 1489–1500.
- [67] Y. Shin, J.S. Jeon, S. Han, et al., In vitro 3D collective sprouting angiogenesis under orchestrated ANG-1 and VEGF gradients, *Lab Chip* 11 (2011) 2175–2181.
- [68] J.A. Whisler, M.B. Chen, R.D. Kamm, Control of perfusable microvascular network morphology using a multiculture microfluidic system, *Tissue Eng. Part C Methods* 20 (2014) 543–552.
- [69] K. Yamamoto, K. Tanimura, Y. Mabuchi, et al., The stabilization effect of mesenchymal stem cells on the formation of microvascular networks in a microfluidic device, *J. Biomech. Sci. Eng.* 8 (2013) 114–128.
- [70] B.S. Kim, A.J. Putnam, T.J. Kulik, et al., Optimizing seeding and culture methods to engineer smooth muscle tissue on biodegradable polymer matrices, *Biotechnol. Bioeng.* 57 (1998) 46–54.
- [71] L. Corstorphine, M.V. Sefton, Effectiveness factor and diffusion limitations in collagen gel modules containing HepG2 cells, *J. Tissue Eng. Regen. Med.* 5 (2011) 119–129.
- [72] D.M. Dean, A.P. Napolitano, J. Youssef, et al., Rods, tori, and honeycombs: the directed self-assembly of microtissues with prescribed microscale geometries, *FASEB J.* 21 (2007) 4005–4012.
- [73] J.M. Kelm, V. Djonov, L.M. Ittner, et al., Design of custom-shaped vascularized tissues using microtissue spheroids as minimal building units, *Tissue Eng.* 12 (2006) 2151–2160.
- [74] J. Yeh, Y. Ling, J.M. Karp, et al., Micromolding of shape-controlled, harvestable cell-laden hydrogels, *Biomaterials* 27 (2006) 5391–5398.
- [75] A.P. McGuigan, M.V. Sefton, Vascularized organoid engineered by modular assembly enables blood perfusion, *Proc. Natl. Acad. Sci. USA* 103 (2006) 11461–11466.
- [76] T.P. Cooper, M.V. Sefton, Fibronectin coating of collagen modules increases in vivo HUVEC survival and vessel formation in SCID mice, *Acta Biomater.* 7 (2011) 1072–1083.
- [77] M.D. Chamberlain, R. Gupta, M.V. Sefton, Bone marrow-derived mesenchymal stromal cells enhance chimeric vessel development driven by endothelial cell-coated microtissues, *Tissue Eng. Part A* 18 (2011) 285–294.
- [78] A.P. McGuigan, B. Leung, M.V. Sefton, Fabrication of cells containing gel modules to assemble modular tissue-engineered constructs, *Nat. Protoc.* 1 (2006) 2963–2969.
- [79] Y. Du, E. Lo, S. Ali, et al., Directed assembly of cell-laden microgels for fabrication of 3D tissue constructs, *Proc. Natl. Acad. Sci. USA* 105 (2008) 9522–9527.
- [80] J.W. Nichol, A. Khademhosseini, Modular tissue engineering: engineering biological tissues from the bottom up, *Soft Matter* 5 (2009) 1312–1319.
- [81] Y. Du, M. Ghodousi, H. Qi, et al., Sequential assembly of cell-laden hydrogel constructs to engineer vascular-like microchannels, *Biotechnol. Bioeng.* 108 (2011) 1693–1703.
- [82] W. He, Z. Ma, W.E. Teo, et al., Tubular nanofiber scaffolds for tissue engineered small-diameter vascular grafts, *J. Biomed. Mater. Res. Part A* 90 (2009) 205–216.
- [83] I.O. Smith, X.H. Liu, L.A. Smith, et al., Nanostructured polymer scaffolds for tissue engineering and regenerative medicine, *Wiley Interdiscip. Rev. Nanomed. Nanobiotechnol.* 1 (2009) 226–236.
- [84] L. Ghasemi-Mobarakeh, M.P. Prabhakaran, M. Morshed, et al., Electrospun poly (ϵ -caprolactone)/gelatin nanofibrous scaffolds for nerve tissue engineering, *Biomaterials* 29 (2008) 4532–4539.
- [85] D. Klumpp, M. Rudisile, R.I. Kühnle, et al., Three-dimensional vascularization of electrospun PCL/collagen-blend nanofibrous scaffolds in vivo, *J. Biomed. Mater. Res. A* 100 (2012) 2302–2311.
- [86] L. Cui, J. Li, Y. Long, et al., Vascularization of LBL structured nanofibrous matrices with endothelial cells for tissue regeneration, *RSC Adv.* 7 (2017) 11462–11477.
- [87] F. Du, H. Wang, W. Zhao, et al., Gradient nanofibrous chitosan/poly ϵ -caprolactone scaffolds as extracellular microenvironments for vascular tissue engineering, *Biomaterials* 33 (2012) 762–770.
- [88] L.S. Wray, J. Rnjak-Kovacina, B.B. Mandal, et al., A silk-based scaffold platform with tunable architecture for engineering critically-sized tissue constructs, *Biomaterials* 33 (2012) 9214–9224.
- [89] S.F. Badyal, D. Taylor, K. Uygun, Whole-organ tissue engineering: decellularization and recellularization of three-dimensional matrix scaffolds, *Annu. Rev. Biomed. Eng.* 13 (2011) 27–53.
- [90] M. Chiquet, Regulation of extracellular matrix gene expression by mechanical stress, *Matrix Biol.* 18 (1999) 417–426.
- [91] M. Yang, C. Chen, X. Wang, et al., Favorable effects of the detergent and enzyme extraction method for preparing decellularized bovine pericardium scaffold for tissue engineered heart valves, *J. Biomed. Mater. Res. Part B Appl. Biomater.* 91 (2009) 354–361.
- [92] P.M. Crapo, T.W. Gilbert, S.F. Badyal, An overview of tissue and whole organ decellularization processes, *Biomaterials* 32 (2011) 3233–3243.
- [93] R.-H. Fu, Y.-C. Wang, S.-P. Liu, et al., Decellularization and recellularization technologies in tissue engineering, *Cell Transplant.* 23 (2014) 621–630.
- [94] C. Quint, Y. Kondo, R.J. Manson, et al., Decellularized tissue-engineered blood vessel as an arterial conduit, *Proc. Natl. Acad. Sci. USA* 108 (2011) 9214–9219.
- [95] L. Dall’Omo, I. Zanusso, R. Di Liddo, et al., Blood vessel-derived acellular matrix for vascular graft application, *Biomed. Res. Int.* 2014 (2014) 685426.
- [96] A.F. Pellegata, T. Dominioni, F. Ballo, et al., Arterial decellularized scaffolds produced using an innovative automatic system, *Cells Tissues Organs* 200 (2015) 363–373.
- [97] H.C. Ott, T.S. Matthiesen, S.-K. Goh, et al., Perfusion-decellularized matrix: using nature’s platform to engineer a bioartificial heart, *Nat. Med.* 14 (2008) 213–221.
- [98] H.C. Ott, B. Clippinger, C. Conrad, et al., Regeneration and orthotopic transplantation of a bioartificial lung, *Nat. Med.* 16 (2010) 927–933.
- [99] K. Jakab, C. Norotte, B. Damon, et al., Tissue engineering by self-assembly of cells printed into topologically defined structures, *Tissue Eng. Part A* 14 (2008) 413–421.
- [100] F. Marga, A. Neagu, I. Kosztin, et al., Developmental biology and tissue engineering, *Birth Defects Res. C Embryo Today* 81 (2007) 320–328.
- [101] C.M. Owens, F. Marga, G. Forgacs, et al., Biofabrication and testing of a fully cellular nerve graft, *Biofabrication* 5 (2013) 045007.
- [102] Y. Yu, K.K. Moncal, J. Li, et al., Three-dimensional bioprinting using self-assembling scalable scaffold-free “tissue strands” as a new bioink, *Sci. Rep.* 6 (2016) 28714.
- [103] T. Okano, N. Yamada, M. Okuhara, et al., Mechanism of cell detachment from temperature-modulated, hydrophilic-hydrophobic polymer surfaces, *Biomaterials* 16 (1995) 297–303.
- [104] H. Sekine, T. Shimizu, K. Sakaguchi, et al., In vitro fabrication of functional three-dimensional tissues with perfusable blood vessels, *Nat. Commun.* 4 (2013) 1399.
- [105] T. Shimizu, H. Sekine, J. Yang, et al., Polysurgery of cell sheet grafts overcomes diffusion limits to produce thick, vascularized myocardial tissues, *FASEB J.* 20 (2006) 708–710.
- [106] Y. Jung, H. Ji, Z. Chen, et al., Scaffold-free, human mesenchymal stem cell-based tissue engineered blood vessels, *Sci. Rep.* 5 (2015) 15116.
- [107] T. Dvir, A. Kedem, E. Ruvinov, et al., Prevascularization of cardiac patch on the omentum improves its therapeutic outcome, *Proc. Natl. Acad. Sci. USA* 106 (2009) 14990–14995.
- [108] A.M. Hiscoc, A.L. Stone, S. Limesand, et al., An islet-stabilizing implant constructed using a preformed vasculature, *Tissue Eng. Part A* 14 (2008) 433–440.
- [109] P. Tremblay, V. Hudon, F. Berthod, et al., Inoculation of tissue-engineered capillaries with the host’s vasculature in a reconstructed skin transplanted on mice, *Am. J. Transplant.* 5 (2005) 1002–1010.
- [110] S. Levenberg, J. Rouwkema, M. Macdonald, et al., Engineering vascularized skeletal muscle tissue, *Nat. Biotechnol.* 23 (2005) 879–884.
- [111] B.R. Shepherd, H.Y. Chen, C.M. Smith, et al., Rapid perfusion and network remodeling in a microvascular construct after implantation, *Arterioscler. Thromb. Vasc. Biol.* 24 (2004) 898–904.

- [112] S.I. Jeong, J.H. Kwon, J.I. Lim, et al., Mechano-active tissue engineering of vascular smooth muscle using pulsatile perfusion bioreactors and elastic PLCL scaffolds, *Biomaterials* 26 (2005) 1405–1411.
- [113] C. Williams, T.M. Wick, Perfusion bioreactor for small diameter tissue-engineered arteries, *Tissue Eng.* 10 (2004) 930–941.
- [114] D. Shweiki, A. Itin, D. Soffer, et al., Vascular endothelial growth factor induced by hypoxia may mediate hypoxia-initiated angiogenesis, *Nature* 359 (1992) 843–845.
- [115] N. Xu, H. Liu, F. Qu, et al., Hypoxia inhibits the differentiation of mesenchymal stem cells into osteoblasts by activation of Notch signaling, *Exp. Mol. Pathol.* 94 (2013) 33–39.
- [116] Y. Liu, S.H. Teoh, M.S. Chong, et al., Contrasting effects of vasculogenic induction upon biaxial bioreactor stimulation of mesenchymal stem cells and endothelial progenitor cells cocultures in three-dimensional scaffolds under in vitro and in vivo paradigms for vascularized bone tissue engineering, *Tissue Eng. Part A* 19 (2013) 893–904.
- [117] K.J. Cronin, A. Messina, K.R. Knight, et al., New murine model of spontaneous autologous tissue engineering, combining an arteriovenous pedicle with matrix materials, *Plast. Reconstr. Surg.* 113 (2004) 260–269.
- [118] A.J. Hussey, M. Winardi, X.-L. Han, et al., Seeding of pancreatic islets into prevascularized tissue engineering chambers, *Tissue Eng. Part A* 15 (2009) 3823–3833.
- [119] S. Naghieh, M. Sarker, M. Karamooz-Ravari, et al., Modeling of the mechanical behavior of 3D bioplotted scaffolds considering the penetration in inter-locked strands, *Appl. Sci.* 8 (2018) 1422, <http://dx.doi.org/10.3390/app8091422>.
- [120] M.D. Sarker, S. aghieh, A.D. McInnes, et al., Regeneration of peripheral nerves by nerve guidance conduits: Influence of design, biopolymers, cells, growth factors, and physical stimuli, *Prog. Neurobiol.* (2018), <http://dx.doi.org/10.1016/j.pneurobio.2018.07.002>.



Contents lists available at ScienceDirect

Journal of Pharmaceutical Analysis

journal homepage: www.elsevier.com/locate/jpa
www.sciencedirect.com

Original Research Article

A rapid reporter assay for recombinant human brain natriuretic peptide (rhBNP) by GloSensor technology

Lei Yu^{a,1}, Xinchang Shi^{a,1}, Chunmei Han^a, Chunming Rao^{a,*}, Junzhi Wang^{a,b,**}^a National Institutes for Food and Drug Control, Beijing 100050, China^b WHO Collaboration Centre for Biologicals Standardization and Evaluation, Beijing 100050, China

ARTICLE INFO

Article history:

Received 29 November 2017

Received in revised form

17 April 2018

Accepted 18 April 2018

Available online 20 April 2018

Keywords:

RhBNP

cGMP

GloSensor technology

Reporter assay

ABSTRACT

Accurate determination of biological activity is essential in quality control of recombinant human brain natriuretic peptide (rhBNP). In previous study, we successfully developed a genetically modified cell line 293GCAC3-based ELISA assay for rhBNP. But ELISA procedure is still tedious, so this study was aimed to develop a rapid and simple bioassay for rhBNP using GloSensor technology, which provides a platform of flexible luciferase-based biosensors for real-time detection of signaling events in live cells, including cGMP production. A reporter cell line 293GCAGlo-G1 was constructed by transfecting pGloSensor™ 40 F plasmid into 293GCAC3. The reporter assay based on 293GCAGlo-G1 showed high precision with intra-assay CV being 8.3% and inter-assay CV being 14.1%; high accuracy with 80%, 100% and 120% recovery rate being 99.2%, 102.4% and 99.0% respectively; and great linearity with R^2 of linear fitting equation being 0.99. Besides, no significant difference was found in test results of reporter assay and 293GCAC3-based ELISA assay (paired t test, $p = 0.630$). All these results suggested that the reporter assay was a viable assay for biological determination of rhBNP.

© 2018 Xi'an Jiaotong University. Production and hosting by Elsevier B.V. This is an open access article under the CC BY-NC-ND license (<http://creativecommons.org/licenses/by-nc-nd/4.0/>).

1. Introduction

B-type natriuretic peptide (BNP), also called brain natriuretic peptide, is produced primarily by the ventricular myocardium in response to volume and pressure overload [1–3]. Recombinant human B-type natriuretic peptide (rhBNP) was approved by FDA in 2001 to treat severe congestive heart failure and recommended in the acute decompensated heart failure (ADHF) treatment guidelines by the European Society of Cardiology (ESC) in 2005 [4–6]. It also obtained a China national new drug certificate and production license in 2005. It can mediate natriuretic, diuretic and smooth muscle relaxant effects, and thus decrease in preload and afterload by venous and arterial vasodilation, which results in increased cardiac output [7–9]. A recent clinical study found that continuous administration of rhBNP can improve heart and renal function in patients after cardiopulmonary bypass surgery as well as accelerate the recovery from myocardial injury [10].

As rhBNP is used more and more widely in clinic, it is imperative to improve the quality standards of relevant pharmaceutical products. In previous study, we developed a 293GCAC3 cell-based ELISA assay to replace rabbit aortic strips test (RAST), which simplifies the experiment and improves accuracy and precision, and this cell-based assay has been widely applied within the industry in China [11]. But ELISA procedure is still very tedious, with repeated washing of plate, which surely would bring variation in measurements. Besides, since the concentration of different batches of commercial anti-cGMP antibodies and HRP-cGMP is not uniform, the dilution rates of working solutions need to be reconfirmed by pre-experiments when new batches of reagents are used. Here we introduce a rapid bioassay for rhBNP using GloSensor technology, which provides a platform of flexible luciferase-based biosensors for real-time detection of signaling events in live cells, including cAMP, cGMP and protease activity. pGloSensor™ cGMP (Promega) uses genetically encoded biosensor variant with cGMP binding domain fused to mutant form of Photinus pyralis luciferase [12,13]. Upon binding to cGMP, conformational changes occur, promoting large increases in light output. The magnitude of the luminescence increase is directly proportional to the amount of rhBNP. This Glo-Sensor technology was developed ten years ago and primarily applied in research on cellular signaling mechanism in the past few years. This is the first time for this technology to be used in bioactivity determination of bio-drugs, and our study provides a

Peer review under responsibility of Xi'an Jiaotong University.

* Corresponding author.

** Corresponding author at: National Institutes for Food and Drug Control, Beijing 100050, China.

E-mail addresses: raocm@nifdc.org.cn (C. Rao),
wangjz_nifdc2014@163.com (J. Wang).¹ These authors contributed equally to this work.<https://doi.org/10.1016/j.jpha.2018.04.003>2095-1779/© 2018 Xi'an Jiaotong University. Production and hosting by Elsevier B.V. This is an open access article under the CC BY-NC-ND license (<http://creativecommons.org/licenses/by-nc-nd/4.0/>).

new way to detect agonists of guanylate cyclase / adenylylase cyclase receptors and G protein-coupled receptors.

In this study we developed a reporter cell line 293GCAGlo-G1 by transfecting the plasmid pGloSensor™ cGMP into 293GCAC3 cells, which could produce increased light output to rhBNP stimulation. A reporter assay based on 293GCAGlo-G1 was subsequently established and validated, as well as compared with 293GCAC3 cell-based ELISA assay.

2. Materials and methods

2.1. Materials

293GCAC3 cell line was constructed by National Institute for the Control of Pharmaceutical and Biological Products, Beijing, China. DMEM-high glucose, fetal calf serum, 0.25% trypsin-EDTA and G418 were from Thermo Fisher Scientific (Waltham, MA, USA). GloSensor™ cAMP reagent and pGloSensor™ 40F plasmid were from Promega (Madison, Wisconsin, USA). X-transgene 9 transfection reagent was from Roche (Basel, Switzerland). Hygromycin B was from Amresco (Englewood, Colorado, USA). 3-Isobutyl-1-Methylxanthine (IBMX) was from Sigma-Aldrich (Stockholm, Sweden). rhBNP reference (500 units per vial) and rhBNP samples were supplied by manufacturers (China).

2.2. Cell culture, transfection and clone selection

2.2.1. Cell culture

293GCAC3 cells were grown in DMEM-high glucose supplemented with 10% fetal calf serum and 200 µg/mL G418. Cell passaging was achieved by detaching the cells in 0.25% trypsin-EDTA and splitting the cells every 3 days.

2.2.2. Transfection

293GCAC3 cells (approximately 80% confluence) in 6-well plate were transfected with the plasmid using X-transgene 9 transfection reagent according to the protocol. After cultured in growth media for 48 h, cells were collected for next test.

2.2.3. Clone selection

293GCAC3 cells transfected with pGloSensor™ 40F were cultured in growth media for 48 h. Then the growth media was replaced with selective media containing 200 µg/mL G418 and 100 µg/mL hygromycin B. After growth in selective media for 4 weeks, resistant clones were subcloned by limited dilution and screened for the induction of light output by treatment of cells with gradient concentrations of rhBNP. The clone exhibiting the highest responsiveness to rhBNP was further characterized.

2.3. 293GCAC3-based ELISA assay

293GCAC3 cells in DMEM without antibiotics and serum were seeded in 96-well costar plates (1.8×10^4 /well in a total volume of 180 µL) and incubated at 37 °C in a CO₂ incubator for 16–18 h. RhBNP reference or samples were gradiently diluted by 4 times in PBS buffer containing 1 mM IBMX and 0.1% BSA, and 20 µL rhBNP serial dilutions were added to the cell plate, which was then incubated at 37 °C in a CO₂ incubator for 1.5–2 h. Protein G pre-coated microtiter plate was incubated with 100 µL cGMP antibodies for 1 h. 50 µL culture supernatant and 50 µL HRP-cGMP conjugate were mixed, and put into cGMP antibody coated plate, shaking at room temperature for 3 h. Then the mixtures were discarded, and the plate was washed 4 times. 100 µL TMD substrates were put into the plate, reacting at room temperature for 10 min, and terminated by 100 µL stop buffer. OD₄₅₀ values were then determined by reading on a SPECTRAMax plate reader.

2.4. Reporter assay

293GCAGlo-G1 cells in analysis medium (IMDM supplemented with 10% fetal calf serum) were seeded in 96-well white plates (4×10^4 /well in a total volume of 50 µL), and incubated at 37 °C in a CO₂ incubator for 16–18 h. 30 µL equilibration medium (3 mL analysis medium supplemented with 200 µL of GloSensor™ cAMP reagent stock solution) was put into the cell plate and incubated at room temperature for 2 h. rhBNP reference or samples was gradiently diluted 2 times in analysis medium, and 20 µL rhBNP serial dilutions were added to the cell plate, which was then incubated at room temperature for 30–60 min. Luminescence values were determined by reading on a SPECTRAMax plate reader at set intervals.

2.5. Statistical analysis

Analyses of the data consisted of statistical models used to calculate EC₅₀ value as well as statistical techniques for method validation. In order to calculate the EC₅₀ values, dose response and linear range, we used the 4-PL model. Analyses were carried out using GraphPad Prism 5 and SigmaPlot 12 for EC₅₀ calculations and method validation.

3. Results

3.1. Responsiveness of 293GCAC3 transfected with pGloSensor™ 40F to rhBNP stimulation

As the initial step, we transiently transfected 293GCAC3 cells with the plasmid pGloSensor™ 40F and tested whether it could produce increased light output to rhBNP stimulation. 5 h after transfection, equilibration medium was added and incubated at room temperature for 2 h, followed by rhBNP stimulation (serial concentrations) for 90 min and the light output was detected at set intervals. The results are shown in Fig. 1. The results indicated that pGloSensor™ 40F transfected 293GCAC3 cells produced increased levels of light output in response to the ascending concentrations of rhBNP, and the increase of light output was the highest between 30 and 40 min. As the cells transiently transfected with pGloSensor™ 40F demonstrated excellent responsiveness to rhBNP treatment, we then set out to develop a stable reporter cell line.

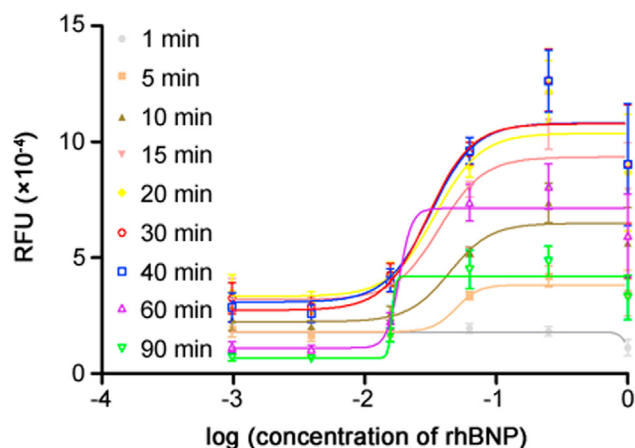


Fig. 1. Responsiveness of 293GCAC3 transfected with pGloSensor™ 40F to rhBNP stimulation. 293GCAC3 cells transfected with pGloSensor™ 40F were stimulated by rhBNP dilutions and the light output was determined at set intervals (5, 10, 15, 20, 25, 30, 40, 60 and 90 min). Each point and error bar represents the mean and standard deviation of three replicates, respectively.

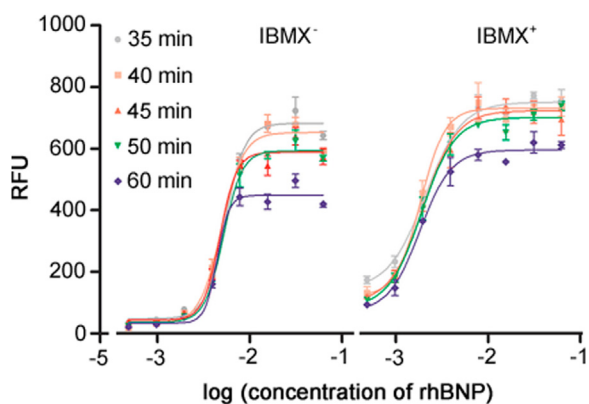


Fig. 2. The effect of IBMX on the reporter assay. 293GCAGlo-G1 cells were stimulated by rhBNP dilutions with or without the presence of IBMX (1 mM). Each point and error bar represents the mean and standard deviation of two replicates, respectively.

3.2. Development of a reporter assay for rhBNP

293GCAC3 cells were transfected with pGloSensor™ 40F, and cultured in selective media containing 100 µg/mL hygromycin B for 4 weeks. Positive clones were obtained by limited dilution. As shown in Fig. S1, clone G1 was found to produce highest level of light output in response to rhBNP treatment, which was next employed to develop a reporter assay for rhBNP. Various parameters of the assay were optimized, including cell number (40,000 per well), concentration range of rhBNP (.002–0.25 µg/mL), and stimulation time (30–40 min). Given the presence of IBMX, an inhibitor of phosphodiesterase (PDE), is essential in ELISA assay, we tested the influence of IBMX (1 mM) in this reporter assay. As shown in Fig. 2, with the presence of IBMX, the magnitude and stability of light output improved slightly, but the background light output was significantly increased (about 3 times), which was against the accuracy and precision of the assay. So for the reporter assay, IBMX was unnecessary. The parameters of dose-response curves of 293GCAGlo-G1 cells stimulated by rhBNP dilutions with or without the presence of IBMX are also listed in Table 1, including slope, minimum and maximum light outputs, EC₅₀ and R². Although the light outputs changed over time, the EC₅₀ values were relatively stable (CV was 7.7% for IBMX⁻ and 5.8% for IBMX⁺).

3.3. Precision, linearity, and accuracy

To validate the reporter assay, all tests were conducted according to ICH Guidelines, including precision, linearity, and

accuracy. Five repeated analyses of rhBNP sample in one test or five different tests were conducted to evaluate intra- or inter-assay precision. Intra-assay CV was 8.3% and inter-assay CV was 14.1%, demonstrating high precision. Accuracy was evaluated by testing recovery rates, and the specific approach was that 80%, 100% and 120% rhBNP references were mixed with 100% rhBNP sample and tested simultaneously. The recovery rate was represented by the percentage rate of the difference between measured value of mixture and measured value of 100% rhBNP sample to expected value of rhBNP reference in mixture. The 80%, 100% and 120% recovery rates were 99.2%, 102.4% and 99.0% respectively, demonstrating great accuracy of the assay. Linearity was evaluated by testing 25%, 50%, 75%, 100% and 125% of rhBNP samples, and the linear fitting equation ($y = 0.99x - 0.01$, $R^2 = 0.99$) represents the correlation between them, where x is expected value and y is measured value. The slope of 0.99 suggested high correlations between expected values and measured values, and R² of 0.99 showed great linearity.

3.4. Comparison of reporter assay with ELISA assay

The agreement between reporter assay and ELISA assay was assessed by testing various samples using both methods. Three rhBNP bulks and three rhBNP products were tested by both methods, and the results are listed in Table 2. Paired T test showed no significant difference between two methods ($p = 0.630$), suggesting the consistency of two methods in test results. Then we compared two methods in materials, operation steps, sensitivity, signal to noise ratio (SNR) and precision (Table 3). The two methods were similar in sensitivity and precision, but the reporter assay was more rapid and simpler.

4. Discussion

Bioactivity determination is a critical quality attribute (CQA) for quality control of biological drugs, including rhBNP. The biological activity of this peptide drug was determined by RAST earlier, which is known to be laborious and time-consuming, with poor reproducibility and isolation of fresh aortic strip from sacrificed rabbit [14,15]. Numerous attempts have been made over decades to develop alternative assays aiming at reduced use of animals and improved precision and robustness. The biological action of BNP is mediated by its main receptor natriuretic peptide receptor-A (NPR-A)/ guanylyl cyclase site (GC-A), which has a guanylyl cyclase site. Activated GC-A receptor could catalyze the conversion of guanosine triphosphate (GTP) to cyclic guanosine monophosphate (cGMP), a second messenger triggering potent physiological actions [16–19]. Given the well-characterized pathways

Table 1.

The parameters of dose-response curves of 293GCAGlo-G1 cells stimulated by rhBNP dilutions with or without the presence of IBMX.

IBMX	Parameter	35 min	40 min	45 min	50 min	60 min	Average	RSD (%)
IBMX ⁻	Hillslope	3.98	3.63	4.30	4.42	7.57	4.78	33.3
	Min light output	43.41	32.35	37.75	35.92	31.70	36.22	13.1
	Max light output	663.52	634.83	557.64	558.72	422.15	567.37	16.5
	EC ₅₀ (ng/mL)	5.38	5.09	4.76	5.02	4.37	4.92	7.7
	R ²	0.98	0.97	0.95	0.96	0.95	0.96	1.4
IBMX ⁺	Hillslope	2.44	3.09	2.27	2.75	2.62	2.63	11.8
	Min light output	150.22	106.59	88.75	87.83	65.31	99.74	31.9
	Max light output	724.20	716.13	709.02	666.20	575.60	678.23	9.1
	EC ₅₀ (ng/mL)	2.04	1.85	1.97	1.82	1.77	1.89	5.8
	R ²	0.93	0.95	0.95	0.95	0.96	0.95	0.9

Table 2.
Test results of rhBNP samples by ELISA assay and reporter assay.

Sample	ELISA assay (units/mL)	Reporter assay (units/mL)
Bulk 01	2588	2714
Bulk 02	2835	2666
Bulk 03	2040	2102
Product 01	341	382
Product 02	616	668
Product 03	514	528

Paired *T* test, $p = 0.630$.

activated by BNP, quantification of cGMP in cells exposed to rhBNP has been explored as attractive alternative assay. Indeed, several types of cGMP-involved assays for rhBNPs have been reported in recent years, including the measurement of cGMP in human umbilical vein endothelial cells (HUVEC) or PC12 cells by radioimmunoassay, as well as a modified cell line 293GCAC3 by ELISA assay, which was developed by our previous work [11].

In this study, a new reporter assay was explored based on GloSensor technology, a platform technology of biosensors for the intracellular detection of signal transduction in living cells developed by Promega Corporation [13,14,20]. The plasmid pGloSensor™ 40F encodes a biosensor variant with cGMP binding domain fused to a mutant form of *Photinus pyralis* luciferase. Upon binding to cGMP, conformational changes occur, promoting large increases in light output. A reporter cell line was constructed by transfecting pGloSensor™ 40F into GCA-overexpressing cell line 293GCAC3. Fig. 3 describes the principle of this new reporter assay. Method validation was conducted according to ICH Guidelines, including precision, linearity, and accuracy. The reporter assay showed high precision with intra-assay CV being 8.3% and inter-assay CV being 14.1%; high accuracy with 80%, 100% and 120% recovery rate being 99.2%, 102.4% and 99.0% respectively; and great linearity with R^2 of linear fitting equation being 0.99. Given the specificity of reporter assay was consistent with ELISA assay, which has been validated in former study [11], it is unnecessary to evaluate it again. Besides, no significant difference was found in results of reporter assay and 293GCAC3-based ELISA assay (paired *T* test, $p = 0.630$). The two methods were similar on sensitivity and precision, but the reporter assay is more rapid and simpler for avoidance of ELISA steps.

5. Conclusion

Collectively, all our results suggested that the reporter assay was a viable assay for biological determination of rhBNP products,

Table 3.
Comparison between ELISA assay and reporter assay.

Materials, method and result	ELISA assay	Reporter assay
Cell line	293GCAC3	293GCAGlo-G1
Extra materials	IBMX, HRP-cGMP, anti-cGMP antibody, dilution buffer, wash buffer, TMB substrate, stop solution, Protein G-coated plate	GloSensor™ cAMP Reagent, White cell plate
Experiment steps	<ol style="list-style-type: none"> 1. Preparation of cell plate (16–18 h) 2. Preparation of BNP samples and stimulation for 1.5–2 h 3. Immobilization of anti-cGMP antibody (1 h) 4. Competitive ELISA test (3–4 h) 5. Determination 	<ol style="list-style-type: none"> 1. Preparation of cell plate (16–18 h) 2. Equilibration for 2 h 3. Preparation of BNP samples and stimulation for 0.5–1.5 h 4. Determination
Sensitivity(EC_{50})	~5 ng/mL	~5 ng/mL
SNR (signal to noise ratio)	> 2.5	> 10
Intra-assay CV	< 10%	< 10%
Inter-assay CV	< 20%	< 20%

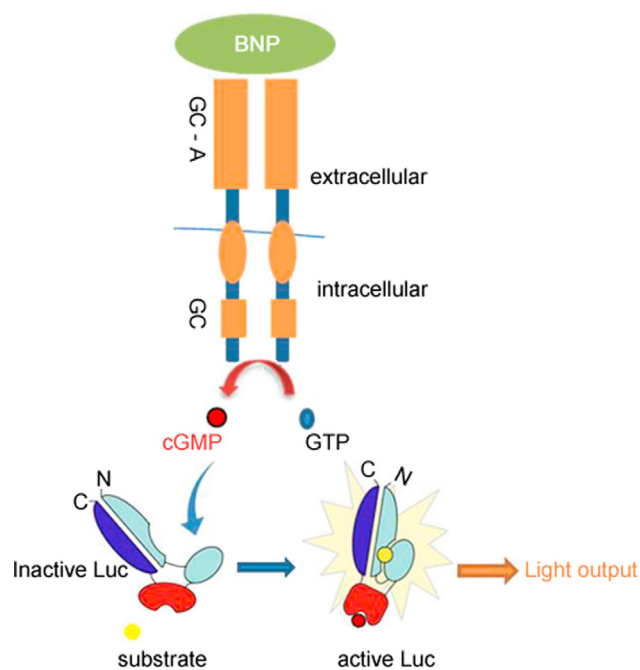


Fig. 3. A sketch for the principle of new reporter assay.

and single-reagent and one-step determination made the assay more controlled and suitable in routine inspection compared with former ELISA assay. What is more, our study provides a new way to detect agonists of guanylate cyclase/adenylate cyclase receptors and G protein-coupled receptors, which would promote the research and development (R&D) of these types of bio-drugs.

Conflicts of interest

The authors declare that there are no conflicts of interest.

Acknowledgments

This work was financially supported by grants from the National Science and Technology Major Project (No. 2015ZX09501008-001) and the Middle-aged and Young Development Research Foundation of NIFDC (No. 2017B3). The funders had no role in study design, data collection and analysis, decision to publish, or preparation of the manuscript.

Appendix A. Supplementary material

Supplementary data associated with this article can be found in the online version at doi:10.1016/j.jpha.2018.04.003.

References

- [1] K. Hosoda, K. Nakao, M. Mukoyama, et al., Expression of brain natriuretic peptide gene in human heart. Production in the ventricle, *Hypertension* 17 (1991) 1152–1155.
- [2] B. Cauliez, M.C. Berthe, A. Lavoinne, Brain natriuretic peptide: physiological, biological and clinical aspects, *Ann. Biol. Clin. (Paris)* 63 (2005) 15–25.
- [3] K.S. Misono, J.S. Philo, T. Arakawa, et al., Structure, signaling mechanism and regulation of the natriuretic peptide receptor guanylate cyclase, *FEBS J.* 278 (2011) 1818–1829.
- [4] M.S. Nieminen, M. Bohm, M.R. Cowie, et al., Executive summary of the guidelines on the diagnosis and treatment of acute heart failure: the task force on acute heart failure of the European Society of Cardiology, *Eur. Heart J.* 26 (2005) 384–416.
- [5] G.M. Keating, K.L. Goa, Nesiritide: a review of its use in acute decompensated heart failure, *Drugs* 63 (2003) 47–70.
- [6] S. Iyengar, D.S. Feldman, R. Trupp, et al., Nesiritide for the treatment of congestive heart failure, *Exp. Opin. Pharm.* 5 (2004) 901–907.
- [7] A.D. Michaels, A. Klein, J.A. Madden, et al., Effects of intravenous nesiritide on human coronary vasomotor regulation and myocardial oxygen uptake, *Circulation* 107 (2003) 2697–2701.
- [8] S. Dunavant, Nesiritide vs nitroglycerin for decompensated congestive heart failure, *JAMA* 288 (2002) 571–572 (author reply 572–573).
- [9] S.G. Weeks, Nesiritide: the clinical experience, *Can. J. Cardiol.* 24 (Suppl B) (2008) 19B–21B.
- [10] S. Le, J. Xiao, W. Li, et al., Continuous administration of recombinant human B-type natriuretic peptide can improve heart and renal function in patients after cardiopulmonary bypass surgery, *J. Thorac. Dis.* 9 (2017) 692–701.
- [11] L. Yu, C. Rao, X. Shi, et al., A novel bioassay for the activity determination of therapeutic human brain natriuretic peptide (BNP), *PLoS One* 7 (2012) e49934.
- [12] F. Fan, B.F. Binkowski, B.L. Butler, et al., Novel genetically encoded biosensors using firefly luciferase, *ACS Chem. Biol.* 3 (2008) 346–351.
- [13] B. Binkowski, F. Fan, K. Wood, Engineered luciferases for molecular sensing in living cells, *Curr. Opin. Biotechnol.* 20 (2009) 14–18.
- [14] R. C-M, W.J. Z, Z. Y, et al., Study of the requirements and methods for quality control of recombinant human brain natriuretic peptide, *Chin. J. Pharm. Anal.* 05 (2002) 346–349.
- [15] Z. Sun, J. Chen, H. Yao, et al., Use of Ssp dnaB derived mini-intein as a fusion partner for production of recombinant human brain natriuretic peptide in *Escherichia coli*, *Protein Expr. Purif.* 43 (2005) 26–32.
- [16] I. Kishimoto, T. Tokudome, T. Horio, et al., Natriuretic peptide signaling via guanylyl cyclase (GC)-A: an endogenous protective mechanism of the heart, *Curr. Cardiol. Rev.* 5 (2009) 45–51.
- [17] K.N. Pandey, Guanylyl cyclase / atrial natriuretic peptide receptor-A: role in the pathophysiology of cardiovascular regulation, *Can. J. Physiol. Pharmacol.* 89 (2011) 557–573.
- [18] K.S. Misono, Natriuretic peptide receptor: structure and signaling, *Mol. Cell. Biochem.* 230 (2002) 49–60.
- [19] J. Tremblay, R. Desjardins, D. Hum, et al., Biochemistry and physiology of the natriuretic peptide receptor guanylyl cyclases, *Mol. Cell. Biochem.* 230 (2002) 31–47.
- [20] S.J. Hill, C. Williams, L.T. May, Insights into GPCR pharmacology from the measurement of changes in intracellular cyclic AMP: advantages and pitfalls of differing methodologies, *Br. J. Pharmacol.* 161 (2010) 1266–1275.



Original Research Article

Solution pH jump during antibody and Fc-fusion protein thaw leads to increased aggregation

Kevin P. Kent, Chad E. Schroeder*, Chandana Sharma

Upstream R&D, MilliporeSigma, 13804 W 107th St, Lenexa, KS 66215, USA

ARTICLE INFO

Article history:

Received 1 June 2017

Received in revised form

14 September 2017

Accepted 14 September 2017

Available online 18 September 2017

Keywords:

Monoclonal antibodies

Freeze–thaw

Protein aggregation

Protein stability

ABSTRACT

Freeze–thaw cycles impact the amount of aggregation observed in antibodies and Fc-fusion proteins. Various formulation strategies are used to mitigate the amount of aggregation that occurs upon putting a protein solution through a freeze–thaw cycle. Additionally, low pH solutions cause native antibodies to unfold, which are prone to aggregate upon pH neutralization. There is great interest in the mechanism that causes therapeutic proteins to aggregate since aggregate species can cause unwanted immunogenicity in patients. Herein, an increase in aggregation is reported when the pH is adjusted from pH 3 up to a pH ranging from pH 4 to pH 7 during the thaw process of a frozen antibody solution. Raising the pH during the thaw process caused a significant increase in the percent aggregation observed. Two antibodies and one Fc-fusion protein were evaluated during the pH jump thaw process and similar effects were observed. The results provide a new tool to study the kinetics of therapeutic protein aggregation upon pH increase.

© 2017 Xi'an Jiaotong University. Production and hosting by Elsevier B.V. This is an open access article under the CC BY-NC-ND license (<http://creativecommons.org/licenses/by-nc-nd/4.0/>).

1. Introduction

Aggregation is a critical quality attribute of therapeutic proteins such as monoclonal antibodies (mAbs). It is important to understand the mechanism of protein aggregation since aggregate species often elicit an unwanted immunogenic response in patients. Therefore, reproducibility of manufactured therapeutic proteins with very low levels of aggregates is highly desired in the pharmaceutical industry so that safe products can be delivered. Aggregate formation during the therapeutic protein production process can potentially be the result of any one of many different steps in a typical commercial process [1]. The impact of freeze–thaw on aggregate formation and stability of antibodies has been studied extensively. The pH [2–4], excipients [5–7], ionic strength, containers [2], and heating and cooling rates [8,9] have been shown to impact the stability of antibodies during the freeze–thaw process.

In this work, we describe how an increase in aggregation occurs upon thawing an antibody solution, stored at pH 3 and $-80\text{ }^{\circ}\text{C}$, with a solution that is at a higher pH. The impacts of pH, antibody concentration, buffer, rate of thaw and stabilizing molecules were investigated. In order to ensure this phenomenon was not specific to one particular antibody, key experiments were

repeated with another antibody and an Fc-fusion protein. All three of the proteins contained the Fc region of IgG1, which is implicated in aggregate formation when the pH is increased during thaw. The results are explained by a model for kinetically trapped aggregation that is promoted under these conditions.

2. Materials and methods

2.1. Samples

All protein samples were either produced at MilliporeSigma from CHOZN[®] cell lines grown in chemically defined media (mAb 1 and mAb 2) or purchased commercially (Fc-fusion protein). Unless otherwise noted, all reagents were purchased from Sigma-Aldrich (USA). Buffered solutions were prepared using deionized water (18.2 M Ω -cm) and were filtered (0.22 μm) prior to use. Frozen protein samples were stored in 0.2 mL Greiner Sapphire PCR vials at $-80\text{ }^{\circ}\text{C}$. For protein purifications, 200 μL per sample of Poros[®] MAbCapture[™] Protein A resin (Thermo) was used and rinsed with pH 7 wash buffer (20 mM citrate, 150 mM NaCl) prior to use. Protein samples produced at MilliporeSigma were purified by mixing the centrifuged supernatant (900 μL) with protein A resin for 10 min. The samples were washed twice with 900 μL of pH 7 wash buffer and eluted with 150 μL of pH 3 elution buffer (25 mM citrate).

Following purification, mAb 1 was frozen at $-80\text{ }^{\circ}\text{C}$ in 40 μL aliquots, unless otherwise noted in the text. The second protein, mAb 2, was further processed following the standard purification

Peer review under responsibility of Xi'an Jiaotong University.

* Corresponding author.

E-mail address: chad.schroeder@sial.com (C.E. Schroeder).

procedure at MilliporeSigma. Namely, it was adjusted to pH 5.5 using 50 μ L of additive buffer (2 M L-arginine, 400 mM acetate, pH 8.12) and subsequently frozen at -80 °C. For the purpose of this study, the mAb 2 solution was thawed and subsequently exchanged into pH 3 elution buffer using Amicon[®] 30 K molecular weight cutoff filters for buffer exchange, and then frozen in either 20 μ L or 40 μ L aliquots at -80 °C. The Fc-fusion protein was received as a solid lyophilized formulation. The lyophilized Fc-fusion powder was hydrated with water, exchanged into 25 mM citrate buffer at pH 3 and subsequently frozen in either 20 μ L or 40 μ L aliquots at -80 °C. Both mAb 1 and mAb 2 are IgG1 antibodies and the Fc-fusion protein contains the Fc region of human IgG1. The samples were analyzed for identification and purity using SDS-PAGE analysis (Fig. S1), and the major impurities observed were typically fragments of fusion proteins and mAbs (missing heavy or light chain, Table S1).

2.2. Thaw process

The samples were either allowed to thaw completely at room temperature (RT) and then adjusted with buffers at the specified conditions, or were mixed immediately with buffers at the specified conditions during thaw. Unless otherwise noted, all dilution buffers contained 100 mM citrate. The dilution factor was kept at 7 to 1 for all samples. Unless otherwise noted, 40 μ L samples were used with 240 μ L dilution buffer. For experiments where the samples were mixed after the thaw process, the frozen aliquots were allowed to completely thaw at RT (3 min) and then mixed with buffer at RT using continuous aspiration (10 aspiration cycles with micro-pipette set at 240 μ L for 10 s, 1 aspiration cycle per second). For experiments where the samples were mixed during the thaw process, the frozen aliquots were immediately mixed with buffer at RT using continuous aspiration until the sample completely dissolved (10 aspiration cycles with micro-pipette set at 240 μ L for 10 s, 1 aspiration cycle per second). For samples that were frozen in 20 μ L aliquots, 120 μ L dilution buffer was used (10 aspiration cycles with micro-pipette set at 120 μ L for 10 s, 1 aspiration cycle per second). Care was taken to avoid bubble formation. All samples were filtered through 0.45 μ m GHP filters (Pall) and immediately analyzed by size exclusion chromatography (SEC) for aggregation levels.

2.3. Aggregation assessment

Aggregation was assessed with a Waters Acquity H-Class UPLC system. A Waters UPLC BEH200 SEC column (200 Å, 1.7 μ m, 4.6 mm \times 150 mm) was used for analysis. Peak resolution and aggregate recoveries were increased by adding arginine to the mobile phase in accordance with previous work by Ejima et al. [10]. After further optimization, reproducible recoveries of the aggregates were maximized when the arginine concentration was increased to 500 mM in the mobile phase. The column temperature was also optimized for peak resolution and a temperature of 35 °C gave ideal peak separation while showing no effect on aggregate recoveries. All of the samples were analyzed using an isocratic mobile phase of pH 7.6, 500 mM arginine, 100 mM sodium phosphate, and 200 mM NaCl. The flow rate was 0.4 mL/min. The column temperature was 35 °C, and the samples were stored at 10 °C during analysis. The injection volume was 15 μ L, and the runtime of the method was 7.5 min. The chromatograms were extracted at a wavelength of 280 nm.

3. Results

3.1. Initial observations of mAb 1 aggregation during thaw

When an mAb 1 sample, stored frozen at pH 3, was allowed to completely thaw before being mixed with a higher pH buffer (pH 7), there was no increase in aggregation (Fig. 1). However, when the same sample was immediately mixed with pH 7 buffer during the thaw process, aggregation levels were significantly increased. In order to test whether the induced aggregation was due to a rapid increase in pH or temperature, a control experiment was performed where the mAb 1 sample was mixed with the same storage buffer (pH 3) during the thaw process. The results in Fig. 1 confirm that a rapid increase in temperature alone, was not responsible for causing aggregation since mixing the protein sample with buffer at pH 3 while the sample was still thawing did not result in aggregation. Note that when the frozen protein sample was allowed to completely thaw prior to addition of pH 7 buffer there was no increase in aggregation, which suggests that a rapid increase in pH alone was not responsible for aggregation since the pH change was also relatively fast in this case. There was clearly no difference in aggregation levels when the sample was mixed with either pH 3 buffer during thaw, or pH 7 buffer after the sample was allowed to completely thaw, indicating there was no effect of pH on aggregate formation when the samples were allowed to completely thaw prior to pH adjustment. Taken together, these results show the impact on mAb aggregation was both pH- and thaw-dependent, and not attributable to just a rapid pH increase or the thaw process alone.

3.2. Effect of dilution process on aggregation

3.2.1. Rate of thaw

The temperature of the thawing buffer during the pH jump with mAb 1 was evaluated to see how big of an effect the rate of thaw would have on aggregation levels. The following temperature experiments were performed to investigate this effect on aggregation levels. Frozen samples of mAb 1 were thawed with pH 7 buffer at different rates (with or without aspiration) or with buffer kept at different temperatures (RT or 4 °C). The mAb 1 samples were also allowed to completely thaw before being mixed with pH 7 buffer at RT or 4 °C (Fig. 2).

Different aggregation levels were observed with mAb 1 depending on both the temperature of the dilution buffer and the thawing rate of the sample. In the sample aspirated immediately

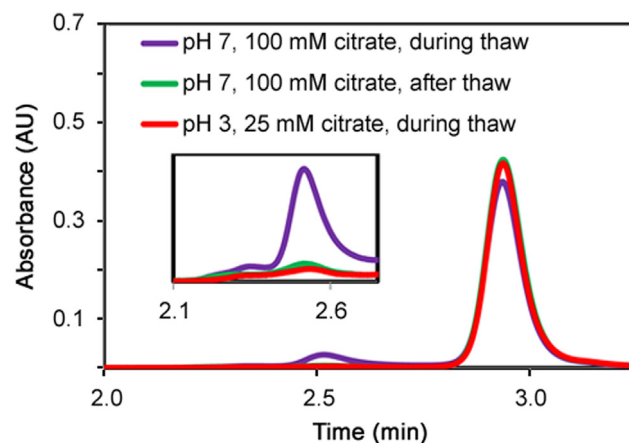


Fig. 1. Size exclusion chromatograms of three mAb 1 samples thawed in different conditions (absorbance at 280 nm). For each sample, the peak observed at 2.8 min was the monomer peak of mAb 1, and anything eluting earlier was considered aggregates. **Inset:** Zoom-in on the chromatogram of the aggregate species.

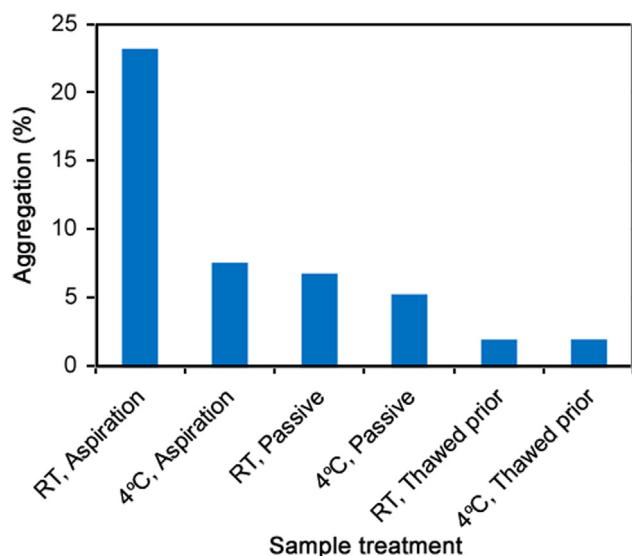


Fig. 2. The percent of aggregation observed when frozen mAb 1 samples were thawed in six different conditions with pH 7, 100 mM citrate (dilution buffer). In the first two conditions, samples were aspirated with dilution buffer stored at the specified temperature. In the third and fourth conditions, the samples were allowed to thaw passively with dilution buffer stored at RT or 4 °C and without aspiration. In the last two conditions, the samples were allowed to completely thaw and then mixed with the dilution buffer at RT or 4 °C.

with RT buffer, the aggregation level was significantly higher than that of the sample aspirated with buffer at 4 °C. When the buffer was added without aspiration (passive), aggregation still occurred, but there was no difference in aggregation levels when the dilution buffer was at 4 °C or RT. The amount of time required for complete thaw of the mAb 1 samples was in the following order: RT Aspiration < 4 °C Aspiration < RT Passive < 4 °C Passive. When the samples were allowed to completely thaw prior to buffer addition, aggregation levels were even lower than that of passive addition, but the temperature of the dilution buffer had no impact on aggregation levels in this case. The results illustrate how the kinetics of protein thawing has an impact on induced aggregation levels when the protein is exposed to higher pH.

3.2.2. pH of dilution buffer

Knowing that the rate of thaw has an effect on aggregation levels, attention was shifted to the role of pH on aggregate formation. In order to further investigate the impact of pH on aggregate formation during the thaw process, pH titration experiments were performed on mAb 1. The pH titration was performed by thawing mAb 1 samples (stored at pH 3) in dilution buffers containing 100 mM citrate at a pH ranging from pH 3 to pH 7. The frozen samples were immediately aspirated with the corresponding dilution buffer at RT. A clear sigmoidal relationship exists between the amount of aggregate formed and the solution pH (Fig. 3). This sigmoidal fit suggests that a titratable group with a pKa of 4.5 is involved in the aggregation process (Fig. 3 inset). Aspiration of the frozen sample with an alternative dilution buffer consisting of 100 mM acetate at pH 5 gave similar results to the corresponding citrate buffer at pH 5.

3.3. Effect of storage buffer on aggregation

3.3.1. pH of storage buffer

In an effort to determine whether the temperature and pH jump on the thaw-induced aggregation process was also dependent on the pH of the frozen solution, samples of mAb 1 were frozen in other solution at pH values of 4–7 (each with 25 mM

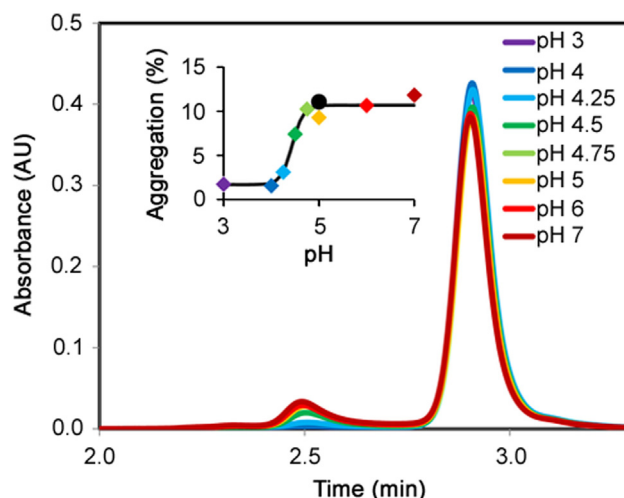


Fig. 3. Size exclusion chromatograms (SEC) of mAb 1 thawed in dilution buffers (100 mM citrate) of varying pH (pH 3 to pH 7). **Inset:** The percent aggregation observed when SEC are plotted vs. solution pH. The colors of the data points coordinate with the colors in the chromatograms. • represents the measurement when pH 5, 100 mM acetate was used.

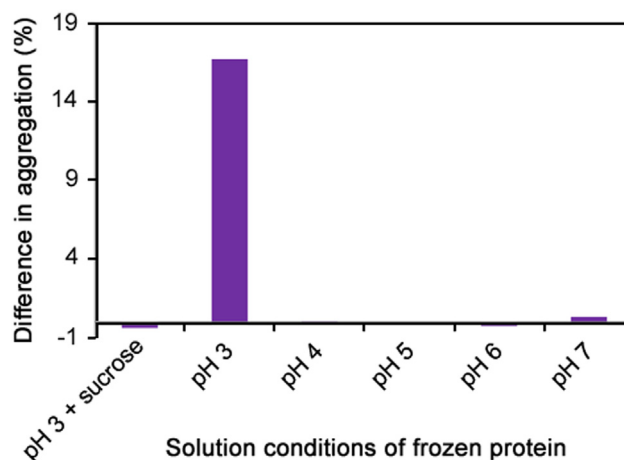


Fig. 4. Difference in percent aggregation when samples were mixed with pH 7 buffer during and after the thaw process. The mAb 1 samples were stored frozen at the pH indicated (with 25 mM citrate). In the experiments with sucrose, the protein sample was frozen with 25 mM citrate and 500 mM sucrose. All of the frozen samples (stored at 2 mg/mL) were adjusted to pH 7 with 7:1 dilution into pH 7, 100 mM citrate solution.

citrate) and again adjusted with pH 7 dilution buffer. All of the samples were mixed with dilution buffer at RT using continuous aspiration either during or after the protein thawed. The results (Fig. 4) are shown as a difference in percent aggregation (difference between when the sample was allowed to thaw completely and when the sample was mixed during thaw). The largest increase in aggregation was observed when the pH 3, protein sample was thawed (aspirated) with pH 7, 100 mM citrate buffer, as previously shown. When the pH of the mAb storage solution was adjusted to a higher pH (pH 4–7) prior to freezing, no increase in aggregation was observed upon thawing with pH 7 buffer. This shows that storing the samples at pH 3 is significant upon thawing at higher pH.

3.3.2. Effect of sucrose

Sucrose is known to protect frozen proteins by serving as a cryoprotectant [6,7] and plays a role in protecting mAb 1 from induced aggregation upon thawing with a higher pH buffer. To test this hypothesis, sucrose was added at a final concentration of

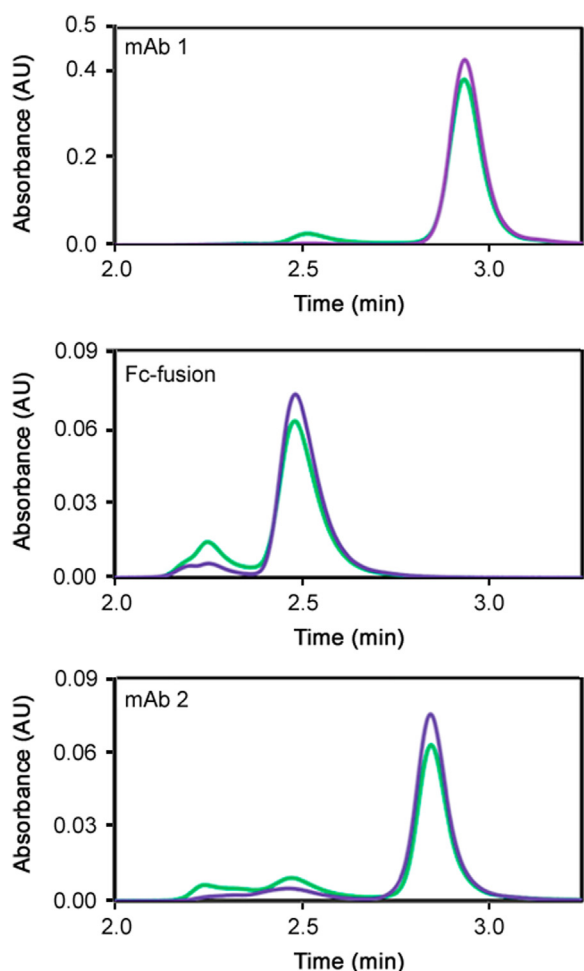


Fig. 5. Absorbance chromatograms of mAb 1, an Fc-fusion protein and mAb 2 when the pH was adjusted during thaw (green) and after thaw (purple). The pH was adjusted from pH 3 in the frozen sample to pH 7 in the final solution. An increase in aggregation is observed for all three proteins. The Fc-fusion and mAb 2 proteins were both at 2 mg/mL in the frozen samples, and the mAb 1 protein was at 7 mg/mL in the frozen sample.

500 mM to the mAb 1 sample and frozen at pH 3 (25 mM citrate). Upon aspirated thawing with pH 7 buffer, no increase in aggregation was observed (Fig. 4), showing that sucrose protects mAb 1 from induced aggregation when samples stored at pH 3 were thawed with a higher pH buffer.

3.4. Generality of protein aggregation during thaw

In order to ensure the aggregation induced phenomenon was not isolated to a single mAb, two other therapeutic proteins were evaluated. An Fc-fusion protein and mAb 2 were exchanged into pH 3, 25 mM citrate buffer and then frozen at -80°C in 20 μL aliquots. The samples were either thawed with mixing in the presence of pH 7 buffer, or allowed to completely thaw before being mixed with the pH 7 buffer. The results (Fig. 5) show that the phenomenon of induced aggregation upon thawing low pH protein samples with higher pH buffers at RT is not isolated to mAb 1 alone. Both the Fc-fusion protein and mAb 2 exhibited an increase in aggregate levels when the samples were subjected to a rapid elevation in pH and temperature. However, in order to fully generalize the kinetic model observed for mAb 1 with other Fc-containing proteins, additional experiments are needed with the Fc-fusion protein and mAb 2, including the effect of thaw rates on aggregation levels.

4. Discussion

4.1. Proposed model for pH jump induced aggregation during thaw

4.1.1. C_{H2} unfolding at low pH

Numerous studies have reported in recent years the mechanism of therapeutic antibody aggregation at low pH [3,4,11–15]. Previous work by Latypov *et al.* [4] showed that IgG1 and IgG2 Fc fragments are largely unfolded at low pH (2.5) and become more ordered in secondary and tertiary structure as the pH is increased to pH 4.7. They discovered unfolding of the C_{H2} domain precluded unfolding in the C_{H3} domain as the pH is lowered. From pH 3.1 to 3.5, the C_{H2} domain is completely unfolded, while the C_{H3} domain is partially unfolded. The driving force for unfolding at low pH is largely influenced by protonation of side residues that are involved in stabilizing secondary and tertiary structures in the native protein at neutral pH [16]. In the native conformation, these residues are oppositely charged and held together through electrostatic attractions, with the native protein having a net neutral charge. At low pH, the non-native protein has an increased net charge due to multiple, positively charged residues [12,17]. The electrostatic repulsions between intramolecular charged residues cause the protein to unfold, exposing hydrophobic segments to the solvent that is usually buried in the core of the folded, native protein. As a result, hydrophobic attractions between adjacent monomers become possible and are strong enough to compete with the energetically unfavorable intermolecular repulsions that exist between positively charged residues on the opposite binding partner [16]. The association of unfolded monomers to form larger oligomers in this manner represents the foundation for non-native protein aggregation, which is a plausible mechanism for explaining the aggregation results observed in this study.

The requirement that the solution pH must be as low as pH 3 to achieve complete unfolding of the native C_{H2} region can explain the results in Fig. 4. The non-native conformation of the monomer that is capable of self-association will only be present when enough side residues have become protonated, which is only possible when the pH is at pH 3. When the pH is at pH 3.5 or above, the C_{H2} domain is partially folded and incapable of binding neighboring monomers. This explains why the frozen proteins must be at pH 3 in order to achieve aggregation upon a pH jump to neutral pH. The pH limit for achieving adequate neutralization of net charge in the non-native monomer appears to be pH 4.5 based on the aggregation results shown in Fig. 3. This result fits the net charge calculations of an IgG1-derived Fc fragment reported by Wu *et al.* [12], in which the net charge was positive at pH 4 and neutral at pH 5.

4.1.2. Kinetically trapped aggregates

In current models for non-native protein aggregation, reversible pathways are used to explain aggregate formation starting from the native monomer [16,18]. Unfolding of the monomer at pH 3 is not considered rate-limiting. Once unfolded, the monomer can associate with adjacent monomers, as mentioned earlier, to form dimer and trimer clusters, which are reversible. However, as the pH is increased towards the isoelectric point of the protein, the dispersed charges that are repelled between monomers in close proximity are neutralized and the hydrophobic attractions become significant. At this point, the protein will either re-fold into the native conformation (thermodynamically reversible formation) or form strong hydrophobic interactions with another monomer in the form of β -sheets, leading to aggregate species which are irreversible [19,20]. The unfolded, neutralized proteins are transiently formed upon exposure to increased pH. The population of monomers that overcome the energy barrier for self-association will reach a local energy minimum and will be kinetically trapped

as an aggregate [13,21]. Although the corresponding aggregates are considered energetically stable with high energy barriers to dissociation, the trapped aggregates formed in this study were found to be slowly reversible (Fig. S2).

4.1.3. Concentration influence on aggregation

As discussed in the previous section, an increase in pH from pH 3 to above pH 4.5 affected the amount of aggregates observed in mAb 1 and was attributed to the stability of the C_{H2} domain in the unfolded protein. However, aggregation levels were not influenced by a pH jump alone. As shown in Fig. 2, the rate at which the frozen sample thawed showed an influence on aggregation. When the sample, frozen at pH 3, was thawed with neutral buffer at pH 7, aggregation levels were appreciably higher when the samples were thawed faster. Cryoconcentration, in which proteins are concentrated into localized sections of a frozen sample, can occur upon freezing [8]. Higher concentrated protein when exposed to a rapid pH shift during the thaw process would lead to unfolded C_{H2} domains being neutralized in closer proximity to other proteins, thus leading to higher aggregation. This model can be used to explain the results in Fig. 2, in which frozen samples that were thawed with aspiration showed higher aggregation levels compared to samples that were passively thawed. The samples that were thawed prior to addition of neutral buffer would have been diluted by the time the pH was increased and expected to show less aggregation, as was the case in this study.

The hypothesis for cryoconcentration as the cause of increased aggregation with increased thaw rate is supported by the observation that sucrose was able to decrease aggregation during rapid thaw with neutral buffer, when it was present in the frozen mAb 1 sample at pH 3 (Fig. 4). Sucrose has the ability to act as a cryoprotectant when added to frozen protein samples [6,7] and as a result, local protein concentrations would change less during the freezing process. Additional experiments were performed to test concentration dependence, in which samples of mAb 1 were frozen in pH 3 buffer at different protein concentrations (Fig. S3). Upon aspirated dilution with neutral buffer, increased aggregation was observed that was proportional to the concentration of frozen protein, further supporting this hypothesis.

5. Conclusions

Frozen samples of three different therapeutic proteins stored at pH 3 showed appreciable amounts of aggregation upon a pH jump and rapid thaw with neutral buffer. The Fc region, common to all three proteins, was implicated in the aggregation process. The stability of the C_{H2} domain within the Fc region was used to explain the kinetic results obtained with mAb 1 and complements the findings of recent reports on the mechanism of aggregation by non-native therapeutic proteins. In particular, aggregates formed by the pH jump thaw process are attributed to a kinetically trapped intermediate that is formed. Various factors promoted the aggregation process such as the rate of thaw and the pH of the frozen protein sample and dilution buffer. Cryoconcentration and pH increase are the proposed root causes to explain the observed phenomenon. Altogether, the findings can be used as a research tool to further study the aggregation kinetics of therapeutic proteins.

Conflicts of interest

The authors declare that there are no conflicts of interest.

Appendix A. Supplementary material

Supplementary data associated with this article can be found in the online version at doi:10.1016/j.jpha.2017.09.002.

References

- [1] M. Vázquez-Ray, D.A. Lang, Aggregates in monoclonal antibody manufacturing processes, *Biotech. Bioeng.* 108 (2011) 1494–1508.
- [2] L.A. Kuelzto, W. Wang, T.W. Randolph, et al., Effects of solution conditions, processing parameters, and container materials on aggregation of a monoclonal antibody during freeze-thawing, *J. Pharm. Sci.* 97 (2008) 1801–1812.
- [3] S.B. Hari, H. Lau, V.I. Razinkov, et al., Acid-induced aggregation of human monoclonal IgG1 and IgG2: molecular mechanism and the effect of solution composition, *Biochemistry* 49 (2010) 9328–9338.
- [4] R.F. Latypov, S. Hogan, H. Lau, et al., Elucidation of acid-induced unfolding and aggregation of human immunoglobulin IgG1 and IgG2 Fc, *J. Biol. Chem.* 287 (2012) 1381–1396.
- [5] L. Kreilgaard, L.S. Jones, T.W. Randolph, et al., Effect of Tween 20 on freeze-thawing- and agitation-induced aggregation of recombinant human factor XIII, *J. Pharm. Sci.* 87 (1998) 1597–1603.
- [6] B.S. Kendrick, B.S. Chang, T. Arakawa, et al., Preferential exclusion of sucrose from recombinant interleukin-1 receptor antagonist: role in restricted conformational mobility and compaction of native state, *Proc. Natl. Acad. Sci. USA* 94 (1997) 11917–11922.
- [7] J.C. Lee, S.N. Timasheff, The stabilization of proteins by sucrose, *J. Biol. Chem.* 256 (1981) 7193–7201.
- [8] P. Kohle, A. Badkar, Protein and solute distribution in drug substance containers during frozen storage and post-thawing: a tool to understand and define freezing-thawing parameters in biotechnology process development, *Biotechnol. Prog.* 27 (2011) 494–504.
- [9] E.Y. Chi, S. Krishnan, T.W. Randolph, et al., Physical stability of proteins in aqueous solution: mechanism and driving forces in nonnative protein aggregation, *Pharm. Res.* 20 (2003) 1325–1336.
- [10] D. Ejima, R. Yumioka, T. Arakawa, et al., Arginine as an effective additive in gel permeation chromatography, *J. Chromatogr. A* 1094 (2005) 49–55.
- [11] P. Arosio, S. Rima, M. Morbidelli, Aggregation mechanism of an IgG2 and two IgG1 monoclonal antibodies at low pH: from oligomers to larger aggregates, *Pharm. Res.* 30 (2013) 641–654.
- [12] H. Wu, K. Truncali, J. Ritchie, et al., Weak protein interactions and pH- and temperature-dependent aggregation of human Fc1, *mAbs* 7 (2015) 1072–1083.
- [13] H. Imamura, S. Honda, Kinetics of antibody aggregation at neutral pH and ambient temperatures triggered by temporal exposure to acid, *J. Phys. Chem. B* 120 (2016) 9581–9589.
- [14] B. Liu, H. Guo, J. Xu, et al., Acid-induced aggregation propensity of nivolumab is dependent on the Fc, *mAbs* 8 (2016) 1107–1117.
- [15] T. Skamris, X. Tian, M. Thorolfsson, et al., Monoclonal antibodies follow distinct aggregation pathways during production-relevant acidic incubation and neutralization, *Pharm. Res.* 33 (2016) 716–728.
- [16] C.J. Roberts, Therapeutic protein aggregation: mechanisms, design, and control, *Trends Biotechnol.* 32 (2014) 372–380.
- [17] H. Wu, R. Kroe-Barrett, S. Singh, et al., Competing aggregation pathways for monoclonal antibodies, *FEBS Lett.* 588 (2014) 936–941.
- [18] S. Saha, S. Deep, Protein aggregation: elucidation of the mechanism and determination of associated thermodynamic and kinetic parameters, *Curr. Phys. Chem.* 4 (2014) 114–136.
- [19] D. Baker, D.A. Agard, Kinetics versus thermodynamics in protein folding, *Biochemistry* 33 (1994) 7505–7509.
- [20] A.L. Fink, Protein aggregation: folding aggregates, inclusion bodies and amyloid, *Fold. Des.* 3 (1998) R9–R23.
- [21] V. Filipe, B. Kukrer, A. Hawe, et al., Transient molten globules and metastable aggregates induced by brief exposure of a monoclonal IgG to low pH, *J. Pharm. Sci.* 101 (2012) 2327–2339.



Contents lists available at ScienceDirect

Journal of Pharmaceutical Analysis

journal homepage: www.elsevier.com/locate/jpa
www.sciencedirect.com

Original Research Article

Primula vulgaris extract induces cell cycle arrest and apoptosis in human cervix cancer cellsSelim Demir^{a,*}, Ibrahim Turan^b, Rezzan Aliyazicioglu^c, Serap Ozer Yaman^d, Yuksel Aliyazicioglu^d^a Department of Nutrition and Dietetics, Faculty of Health Sciences, Karadeniz Technical University, 61080 Trabzon, Turkiye^b Department of Genetic and Bioengineering, Faculty of Engineering and Natural Sciences, Gumushane University, 29100 Gumushane, Turkiye^c Department of Biochemistry, Faculty of Pharmacy, Karadeniz Technical University, 61080 Trabzon, Turkiye^d Department of Medical Biochemistry, Faculty of Medicine, Karadeniz Technical University, 61080 Trabzon, Turkiye

ARTICLE INFO

Article history:

Received 31 January 2018

Received in revised form

9 May 2018

Accepted 14 May 2018

Available online 28 June 2018

Keywords:

Apoptosis

Cell cycle

Cervical cancer

Cytotoxicity

Primula vulgaris

ABSTRACT

Primula vulgaris belongs to the genus *Primula*, members of which are frequently used in folk medicine. Various studies have investigated the cytotoxic effect of different *Primula* species, but there have been limited studies on the cytotoxic effect of *P. vulgaris*. The aim of this study was to investigate the cytotoxic effects, and possible mechanisms involved, of *P. vulgaris* flower extract on human cervical cancer (HeLa) cells. The cytotoxic effect of the extract on HeLa cells was revealed using the MTT assay. Mechanisms involved in the extract's cytotoxic effect were then investigated in terms of apoptosis, mitochondrial membrane potential, and the cell cycle, using fluorometric methods. *P. vulgaris* flower extract exhibited selective cytotoxic effects against HeLa cells by arresting their cell cycle at the S phase, and inducing the number of apoptotic cells compared to normal fibroblast cells by reducing mitochondrial membrane potential in a concentration-dependent manner. This is the first study to reveal the antiproliferative effect of *P. vulgaris* flower extract. Further studies are now needed to identify the cytotoxic molecules in the extract and their mechanisms.

© 2018 Xi'an Jiaotong University. Production and hosting by Elsevier B.V. This is an open access article under the CC BY-NC-ND license (<http://creativecommons.org/licenses/by-nc-nd/4.0/>).

1. Introduction

Cancer is a global health problem, and 21% and 9% of deaths in developed and developing countries, respectively, are reported to be cancer-related. The World Health Organization (WHO) predicts approximately 27 million new cases of cancer and 17.5 million deaths from cancer annually by 2050 [1]. Cervical cancer is the second most common cancer type in women worldwide, and failure to detect the condition at an early stage and/or the development of treatment resistance can lead to fatal outcomes [2]. While the treatment of many cancer patients often involves the use of chemotherapy and radiotherapy, these treatments gradually cause damage to normal cells, and resistance to targeted cancer cells reduces the success rate of these therapies [3]. Current research therefore focuses on developing new generation drugs with fewer side-effects [4].

Plants have been used to treat and prevent many human and animal diseases since ancient times. Today, approximately 50% of the anticancer drugs used in chemotherapy are obtained from

plants. According to the WHO data, more than 80% of people living in developing countries use natural products for primary health problems. Recent surveys show that more than 60% of cancer patients use natural products for therapeutic purposes. However, very few of these medicinal plants have been scientifically evaluated in terms of their anticancer properties. The idea of producing new generation anticancer drugs from natural products has therefore attracted great interest in both the scientific and commercial spheres in recent years [4–6]. *Primula* belongs to the family *Primulaceae*, and more than 400 species are found in the Northern hemisphere, growing in moist and temperate climatic regions [7]. *Primula* species are used in traditional medicine against bronchitis, asthma, and insomnia [6]. *Primula* species are reported to be rich in saponins, alkaloids, tannins, terpenes, and phenolic compounds [7,8]. The antioxidant, antimicrobial, antigenotoxic, anti-inflammatory, hypoglycemic, cytotoxic, and wound healing properties of *Primula* species have been extensively studied, and these useful biological properties are attributed to the presence of the above-mentioned compounds [6–10]. Commercial interest in *Primula* species is growing all the time, especially in the food, cosmetic, and drug industries, due to their beneficial biological properties [6].

Numerous studies have investigated the antiproliferative effect of different *Primula* species. The cytotoxic effect of aqueous

Peer review under responsibility of Xi'an Jiaotong University.

* Corresponding author.

E-mail address: selim-demir@hotmail.com (S. Demir).

extracts of *P. vulgaris* flowers and leaves was examined using the brine shrimp method, and LC₅₀ values of 311 and 40 µg/mL were determined respectively, in one study [11]. Behzad et al. [3] showed that the methanol extract of *Primula auriculata* exhibits apoptotic properties via caspase activation in the human colon cancer (HT-29) cell line. However, no previous studies have investigated the cytotoxic effect of *P. vulgaris* flower extract on cervical cancer cells. The aim of this study was to investigate the cytotoxic effect of *P. vulgaris* flower extract on HeLa cells, together with the mechanism involved.

2. Experimental

2.1. Chemicals and reagents

Gentamicin and trypsin/EDTA solutions were obtained from Biological Industries (Kibbutz Beit Haemek, Israel), Eagle's minimum essential medium (EMEM) from Lonza (Verviers, Belgium), and fetal bovine serum (FBS) from Biochrom (Berlin, Germany). All flow cytometry kits were purchased from Becton Dickinson (San Diego, CA, USA). The other principal chemicals used were obtained from Sigma (St. Louis, MO, USA).

2.2. Sample collection and extract preparation

P. vulgaris plant samples used in the study were collected from Trabzon, Turkiye in the Spring of 2015. The plant samples were dried at room temperature for 20 days. The flower parts were then carefully separated and converted into a fine powder using a blender and milling procedures. Next, 0.5 g of the powdered samples was mixed with 10 mL of dimethyl sulfoxide (DMSO). After thorough vortexing, the mixture was left to incubate for 24 h with continuous shaking at 150 rpm at 45 °C. After incubation, the mixture was centrifuged at 2000 g for 10 min. The supernatant was filtered with Whatman No. 1 filter paper and then passed through 0.2 µm filters. The resulting DMSO extract of *P. vulgaris* flower was aliquoted for use in experiments and stored in the dark at – 20 °C.

2.3. Drug preparation and treatment

Cisplatin was dissolved in DMSO and used as a reference compound in cytotoxicity experiments due to its use in cervical cancer treatment [12]. Final solvent concentrations of compounds were no higher than 0.5% in culture media in any experiment. That concentration was not sufficient to affect cell morphology or viability.

2.4. Cell culture

Human cervix adenocarcinoma (HeLa, ATCC-CCL-2) cancer and human normal foreskin fibroblast (ATCC-CRL-2522) cells were supplied by the American Type Culture Collection (Manassas, VA, USA). Both cells were cultured in EMEM supplemented with 10% heat inactivated FBS and 1% gentamicin solution with a 5% CO₂ supply at 37 °C.

2.4.1. Cytotoxicity experiments

MTT assay with a 72 h treatment time was employed to measure the cytotoxic effects of *P. vulgaris* flower extract and cisplatin on human cervical cancer and normal fibroblast cells [13,14]. Briefly, HeLa and fibroblast cells were seeded into flat-bottomed 96-well cell culture plates at 1×10^4 and 2×10^3 cells per well, respectively. The cells were then treated with varying concentrations of *P. vulgaris* flower extract (0–500 µg/mL) and cisplatin

(0–10 µg/mL) for 72 h in a triplicate manner. Subsequently, 10 µL of MTT dye (0.25 mg/mL) was placed inside each well. The crystals that emerged were then dissolved in DMSO. Finally, absorbance was measured at 570 nm with a microplate reader (Molecular Devices Versamax, California, USA). Optical densities were employed to calculate percentage viabilities in treated cells compared to untreated control cells. Log-concentrations versus % cell viabilities were plotted with a logarithmic graph, which was then used to determine the IC₅₀ values. The IC₅₀ values of the extract and cisplatin in the both cell lines were used to elicit a selectivity index [5] with the following formula:

$$\text{Selectivity Index} = \frac{\text{Fibroblast cells IC}_{50}}{\text{HeLa cells IC}_{50}}$$

2.4.2. Cell cycle analysis

Cell cycle analysis was performed using a commercial kit (BD Cycletest™ Plus, Cat No: 340242, San Diego, CA, USA) following the manufacturer's recommendations. HeLa cells were treated with 90, 180, and 270 µg/mL concentrations of *P. vulgaris* flower extract for 72 h, then harvested, and washed twice with buffer solution. The cells were incubated with trypsin solution for 10 min followed by trypsin inhibitor and RNase solution for 10 min. Finally, the cells were further treated with propidium iodide (PI) staining on ice for 10 min. Data from 30,000 cells per sample were collected and analyzed on a flow cytometer (BD Accuri C6, MI, USA). The percentage of the cells in cycle phases was determined using MODFIT 3.0 verity software. The results were finally compared with the untreated negative control cells.

2.4.3. Apoptosis analysis

Apoptosis analysis was performed using a commercial kit (BD Pharmingen™, Cat No: 559763, San Diego, CA, USA) following the manufacturer's recommendations. HeLa cells were treated with 90, 180, and 270 µg/mL concentrations of *P. vulgaris* flower extract for 72 h, then harvested, and washed twice with ice-cold phosphate-buffered saline solution. The cells were then resuspended with the binding buffer. Next, they were incubated with PE-Annexin V and 7-AAD for 10 min at room temperature in the dark. Data from 10,000 cells per sample were collected and analyzed on a flow cytometer (BD Accuri C6, MI, USA). The results were compared with the untreated negative control cells.

2.4.4. Mitochondrial membrane potential (MMP) analysis

3,3'-dihexyloxycarbocyanine iodide DiOC₆(3) was used to determine the changes in MMP in this study. Normally, this tends to remain in the mitochondria. The decrease in the intensity of this dye is indicative of a decrease in MMP [15]. Cells were seeded into a flat-bottomed 96-well black-walled plate at 1×10^3 cells per well. The cells were then treated with different concentrations of *P. vulgaris* flower extract (90–270 µg/mL) for 72 h. After treatment, the cells were washed with phosphate-buffered saline solution and loaded with 10 nM DiOC₆(3) for 30 min at 37 °C in the dark. Finally, fluorescence measurement was performed on a plate-reading fluorometer (Molecular Devices SpectraMax Paradigm Multi-Mode, Sunnyvale, CA, USA) with an excitation wavelength of 484 nm and an emission wavelength of 525 nm. Results are given as relative MMP compared to untreated negative control cells.

2.5. Statistical analysis

All experiments were performed at least three times, the results being expressed as mean ± standard deviation. Normal distribution was determined using the Kolmogorov-Smirnov test. One-Way ANOVA was used to analyze intergroup differences and

Tukey's test was performed for post-hoc comparisons. $p < 0.05$ was regarded as significant.

3. Results

P. vulgaris flower extract exhibited selective cytotoxic effects on the HeLa cells compared to normal fibroblast cells. The IC_{50} value of the extract in HeLa cells was 182.4 $\mu\text{g/mL}$, while the IC_{50} value of the extract in fibroblast cells was calculated as 493.9 $\mu\text{g/mL}$ (Fig. 1 and Table 1).

The results of the cell cycle analysis are presented in Fig. 2. All the concentrations of *P. vulgaris* flower extract significantly reduced the cell number at the G_2/M phase ($p = 0.0001$). Additionally, 180 and 270 $\mu\text{g/mL}$ extract concentrations significantly reduced the cell number at the G_1 phase and increased the cell number at the S phase compared to the untreated cells ($p = 0.0001$).

The results of the apoptosis analysis are presented in Fig. 3. *P. vulgaris* flower extract significantly reduced the number of viable cells and increased the numbers of apoptotic cells compared to untreated cells in a dose-dependent manner ($p < 0.05$).

MMP analysis results are presented in Fig. 4. The 180 and 270 $\mu\text{g/mL}$ extract concentrations significantly reduced the MMP in HeLa cells ($p = 0.001$). The percentage reductions in MMP caused by *P. vulgaris* flower extract at concentrations of 90, 180, and 270 $\mu\text{g/mL}$ were 8%, 64%, and 72%, respectively.

4. Discussion

Cancer is one of the most important causes of disease-related mortality in the world. The WHO reports that between 2005 and 2015 approximately 84 million people lost their lives due to cancer [3]. Chemotherapy is frequently used in cancer treatment, but the toxic effects that occur over time limit the use of these drugs. Both the high mortality rate in cancer cases and the serious side-effects of chemotherapy and radiotherapy have encouraged the search for alternative and/or complementary treatments [4,5]. Natural products are today regarded as potential raw materials for new drug discoveries, and phenolic compounds found in natural products are particularly significant in this context due to their structures and activities. Investigation of the anticancer effects of both natural product extracts and compounds isolated from such products has become one of the popular research fields in recent years. Various criteria need to be met for an effective and acceptable anticancer agent, including its effects on normal cells being harmless [5,15]. We therefore planned cytotoxicity experiments in HeLa cells coupled with human normal foreskin fibroblast cells.

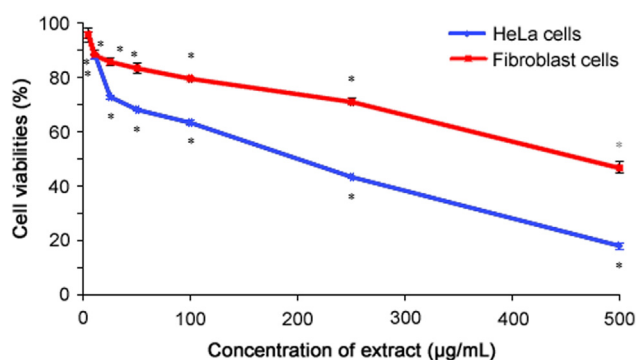


Fig. 1. Effects of different concentrations of *P. vulgaris* flower extract on cell viability during a 72 h incubation period ($n=3$). *There was a statistically significant decrease compared to normal fibroblast cells.

Table 1
Cytotoxic effects (IC_{50} , $\mu\text{g/mL}$) and selectivity index of the test compounds.

Test compound	IC_{50} ($\mu\text{g/mL}$)		Selectivity index
	HeLa cells	Fibroblast cells	
<i>P. vulgaris</i> flower extract	182.4 \pm 5.5	493.9 \pm 2.1	2.7
Cisplatin	0.73 \pm 0.05	4.87 \pm 0.24	6.7

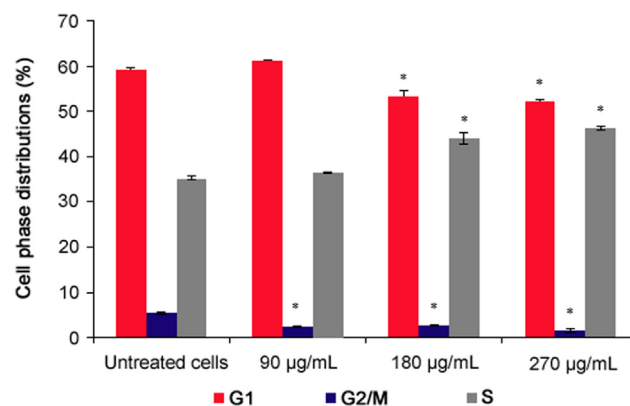


Fig. 2. Cell cycle analysis of *P. vulgaris* flower extract-treated HeLa cells after 72 h ($n=6$). *Represents significant result ($p < 0.05$) compared with untreated cells.

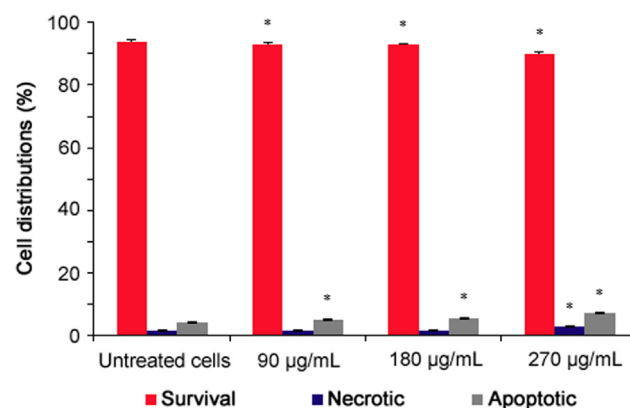


Fig. 3. Apoptosis analysis of *P. vulgaris* flower extract-treated HeLa cells after 72 h ($n=4$). *Represents significant result ($p < 0.05$) compared with untreated cells.

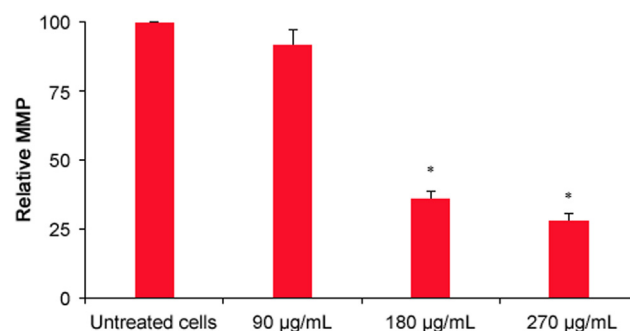


Fig. 4. Effects of *P. vulgaris* flower extract on the integrity of the mitochondrial membrane of HeLa cells after 72 h ($n=3$). *Represents significant result ($p < 0.05$) compared with untreated cells.

Numerous methods, such as trypan blue, MTT assay, neutral red, and lactate dehydrogenase, are frequently used for the determination of cell viability, proliferation rates, and cytotoxicity. In order to determine the cytotoxic effect of the extract, we employ the

MTT, a reliable, sensitive, quantitative, and colorimetric method, previously used in similar studies [5,14,15]. *P. vulgaris* flower extract exhibited selective toxicity (2.7-fold) against HeLa cells compared to normal fibroblast cells. Deterioration of cell cycle control and decreased apoptosis are two of the characteristic features of cancer cells. Anticancer activity studies investigating novel agents therefore focus on the ability to halt the cell cycle and increase apoptosis [5,15,16]. We therefore investigated the mechanism involved in the cytotoxic effect of the extract on HeLa cells in terms of the cell cycle, MMP, and apoptosis using fluorometric methods. Our results show that *P. vulgaris* flower extract exhibited antiproliferative features in HeLa cells by stopping the cell cycle in the S phase and inducing apoptosis by reducing mitochondrial membrane potential in a concentration-dependent manner. Other studies involving the cytotoxic effect of *Primula* species have examined the cytotoxic effect of the ethanolic crude extract of *Primula macrophylla* and its ethyl acetate, chloroform, and benzene fractions using brine shrimp methods, with the most effective cytotoxic activity being observed in the crude extract [17]. Behzad et al. reported that the methanol extract of *Primula auriculata* exhibited a selective cytotoxic effect on human breast (MCF-7), liver (HepG2), and HT-29 cancer cell lines compared to normal bovine kidney cells. No cytotoxic effect was observed in that study in the human lung (A549) cancer cell line up to an extract concentration of 100 µg/mL [18]. Turan et al. [6] demonstrated that *P. vulgaris* leaf extract exhibits selective cytotoxic effects against human A549, HepG2, MCF-7, prostate (PC-3), and colon (WiDr) cancer cell lines compared to human normal fibroblast cells. Few studies have examined the cytotoxic activity of *Primula* species. However, the methanolic extract of *Dionysia termedia*, a member of the *Primulaceae* family, has been reported to exhibit cytotoxic effects in human myelogenous leukemia (K562), T-lymphocytic leukemia (Jurkat), bladder (Fen), and A549 cell lines in a dose-dependent manner. That study also determined that the cytotoxic effect of the extract in blood-derived cell lines (K562 and Jurkat) was derived from induced apoptosis [19]. Another study showed that the aqueous extract of *Lysimachia vulgaris*, a member of the *Primulaceae* family, and its hexane, dichloromethane, and methanol fractions had no cytotoxic effect on the MCF-7 and HepG2 cell lines up to a concentration of 200 µg/mL [20]. Studies have also investigated the antiproliferative activity of various compounds isolated from *Primula* species. Tokalov et al. [21] reported that isolated compounds isolated from *Primula denticulata*, such as 5-hydroxyflavone, 2'-hydroxyflavone, 5,2'-dihydroxyflavone, and 5,8-dihydroxyflavone, exhibit antiproliferative effects in the human acute myeloid leukemia (HL-60) cell line by activating cell cycle arrest and apoptosis.

Polyphenols are an important class of secondary herbal metabolites reported to exhibit strong antioxidant properties [6]. Recent studies in particular have reported that polyphenols can prevent the proliferation of cancer cells by activating cell cycle arrest, apoptosis, and cell signalization [22]. *Primula* species have been shown to be rich in phenolic compounds, such as kaempferol, quercetin, rutin, 5-hydroxy pyrogallol, apigenin, catechin derivatives, gallic acid, rosmarinic acid, *p*-coumaric acid, protocatechuic acid, *p*-OH benzoic acid, vanillic acid, caffeic acid, ferulic acid, and ellagic acid [7,8]. In our previous study, we demonstrated that the major components of *P. vulgaris* are as follows: *p*-coumaric acid (848 µg), rutin (336.5 µg), *p*-OH benzoic acid (76.5 µg), vanillic acid (65 µg), catechin (53.9 µg), caffeic acid (53.1 µg), protocatechuic acid (30.7 µg), and gallic acid (3.2 µg) per g sample [7]. There are also considerable investigations of the anticancer properties of these compounds in various types of cancer cells [23,24]. Studies examining the cytotoxic properties of extracts from various natural products show that the overall effect of the extract has first been examined, and the results have been

attributed to synergistic effects. Effective compounds have been isolated from crude extract, and its biological effects have also been investigated [6]. It is believed that all these phenolic compounds of the *P. vulgaris* flower extract contribute to its cytotoxic effect.

5. Conclusion

This is the first study to examine the mechanisms involved in the in vitro cytotoxic effect of *P. vulgaris* flower extract on HeLa cells. Further studies are now needed for a more detailed understanding of the exact interaction of the signaling pathways involved.

Conflicts of interest

The authors declare that there are no conflicts of interest.

Acknowledgments

The authors wish to thank Professor Ersan Kalay from the Medical Biology Department, Karadeniz Technical University for professional assistance with the flow cytometry studies.

References

- [1] S.A. Hussain, A.A. Sulaiman, C. Balch, et al., Natural polyphenols in cancer chemoresistance, *Nutr. Cancer* 68 (2016) 879–891.
- [2] L. Tao, L. Han, X. Li, et al., Prevalence and risk factors for cervical neoplasia: a cervical cancer screening program in Beijing, *BMC Public Health* 14 (2014) 1185, <http://dx.doi.org/10.1186/1471-2458-14-1185>.
- [3] S. Behzad, K. Ebrahim, M. Mosaddegh, et al., *Primula auriculata* extracts exert cytotoxic and apoptotic effects against HT-29 human colon adenocarcinoma cells, *Iran. J. Pharm. Res.* 15 (2016) 311–322.
- [4] S. Unnati, S. Ripal, A. Sanjeev, et al., Novel anticancer agents from plant sources, *Chin. J. Nat. Med.* 11 (2013) 16–23.
- [5] S. Demir, Y. Aliyazicioglu, I. Turan, et al., Antiproliferative and proapoptotic activity of Turkish propolis on human lung cancer cell line, *Nutr. Cancer* 68 (2016) 165–172.
- [6] I. Turan, S. Demir, R. Aliyazicioglu, et al., Evaluation of antioxidant and cytotoxic properties of *Primula vulgaris* leaf extract, *KSU J. Nat. Sci.* 20 (2017) 361–367.
- [7] M.T. Ozkan, R. Aliyazicioglu, S. Demir, et al., Phenolic characterisation and antioxidant activity of *Primula vulgaris* and its antigenotoxic effect on fibroblast cells, *Jundishapur J. Nat. Pharm. Prod.* 12 (2017) e40073, <http://dx.doi.org/10.5812/jjnpp.40073>.
- [8] F.A. Mostafa, M.A. Gamal, I.R.M. Sabrin, et al., Antioxidant and anti-inflammatory activities of phenolic constituents from *Primula elatior* L. aerial part, *Int. J. Pharm. Pharm. Res.* 6 (2014) 74–78.
- [9] D.D. Orhan, B. Ozelik, S. Hosbas, et al., Assessment of antioxidant, antibacterial, antimycobacterial, and antifungal activities of some plants used as folk remedies in Turkey against dermatophytes and yeast-like fungi, *Turk. J. Biol.* 36 (2012) 672–686.
- [10] K. Aslam, I.A. Nawchoo, M.A. Bhat, et al., Ethno-pharmacological review of genus *Primula*, *Int. J. Adv. Res.* 2 (2014) 29–34.
- [11] A.U. Turker, C. Usta, Biological screening of some Turkish medicinal plant extracts for antimicrobial and toxicity activities, *Nat. Prod. Res.* 22 (2008) 136–146.
- [12] J. Jakubowicz-Gil, R. Paduch, Z. Ulz, et al., Cell death in HeLa cells upon imipenem and cisplatin treatment, *Folia Histochem Cytobiol.* 50 (2012) 381–391.
- [13] T. Mosmann, Rapid colorimetric assay for cellular growth and survival: application to proliferation and cytotoxicity assays, *J. Immunol. Methods* 65 (1983) 55–63.
- [14] I. Turan, S. Demir, K. Kilinc, et al., *Morus rubra* extract induces G₁ cell cycle arrest and apoptosis in human lung and prostate cancer cells, *Ind. J. Pharm. Educ. Res.* 51 (2017) 51–58.
- [15] S. Demir, I. Turan, Y. Aliyazicioglu, et al., *Morus rubra* extract induces cell cycle arrest and apoptosis in human colon cancer cells through endoplasmic reticulum stress and telomerase, *Nutr. Cancer* 69 (2017) 74–83.
- [16] I. Turan, S. Demir, K. Kilinc, et al., Antiproliferative and apoptotic effect of *Morus nigra* extract on human prostate cancer cells, *Saudi Pharm. J.* 25 (2017)

- 241–248.
- [17] Q. Najmus-Saqib, F. Alam, M. Ahmad, Antimicrobial and cytotoxicity activities of the medicinal plant *Primula macrophylla*, *J. Enzyme Inhib. Med. Chem.* 24 (2009) 697–701.
- [18] S. Behzad, A. Pirani, M. Mosaddegh, Cytotoxic activity of some medicinal plants from Hamedan district of Iran, Iran. *J. Pharm. Res.* 13 (2014) 199–205.
- [19] Z. Amirghofran, M. Bahmani, A. Azadmehr, et al., Antitumor activity and apoptosis induction in human cancer cell lines by *Dionysia termedia*, *Cancer Investig.* 25 (2007) 550–554.
- [20] F. Pehlivan Karakas, A. Birinci Yildirim, R. Bayram, et al., Antiproliferative activity of some medicinal plants on human breast and hepatocellular carcinoma cell lines and their phenolic contents, *Trop. J. Pharm. Res.* 14 (2015) 1787–1795.
- [21] S.V. Tokalov, B. Kind, E. Wollenweber, et al., Biological effects of epicuticular flavonoids from *Primula denticulata* on human leukemia cells, *J. Agric. Food Chem.* 52 (2004) 239–245.
- [22] M.L. Hu, Dietary polyphenols as antioxidants and anticancer agents: more questions than answers, *Chang Gung Med. J.* 34 (2011) 449–460.
- [23] D. Ravishankar, A.K. Rajora, F. Greco, et al., Flavonoids as prospective compounds for anti-cancer therapy, *Int. J. Biochem. Cell Biol.* 45 (2013) 2821–2831.
- [24] Y. Zhou, J. Zheng, Y. Li, et al., Natural polyphenols for prevention and treatment of cancer, *Nutrients* 8 (2016) 515, <http://dx.doi.org/10.3390/nu8080515>.



Contents lists available at ScienceDirect

Journal of Pharmaceutical Analysis

journal homepage: www.elsevier.com/locate/jpa
www.sciencedirect.com

Original Research Article

Discourging on Soxhlet extraction of ginseng using association analysis and scanning electron microscopy

Yuan Yue^a, Zi-Dong Qiu^{b,c}, Xian-You Qu^a, Ai-Ping Deng^b, Yuan Yuan^b, Lu-Qi Huang^{b,*}, Chang-Jiang-Sheng Lai^{b,*}^a Chongqing Academy of Chinese Materia Medica, Chongqing Key Laboratory of Traditional Chinese Medicine Resources, Chongqing Sub-center of National Resource Center for Chinese Materia Medica, China Academy of Chinese Medical Sciences, Chongqing 400065, PR China^b National Resource Center for Chinese Materia Medica, China Academy of Chinese Medical Sciences, State Key Laboratory Breeding Base of Dao-di Herbs, Beijing 100700, PR China^c State Key Laboratory of Natural Medicines (China Pharmaceutical University), No. 24 Tongjia lane, Nanjing 210009, PR China

ARTICLE INFO

Article history:

Received 11 July 2018

Received in revised form

22 August 2018

Accepted 23 August 2018

Available online 23 August 2018

Keywords:

Ginseng
Ginsenosides
Soxhlet extraction
Repeatability
Siphon times

ABSTRACT

Soxhlet extraction is a common method of sample preparation. However, there has been no discussion about the efficiency of Soxhlet extraction from different batches and the factors that cause content fluctuation. In this study, *Panax ginseng* was selected as a model sample. Soxhlet extraction by means of a water bath, which has always been neglected, was identified as a novel key factor in the poor repeatability in different batches of Soxhlet extraction, as it can affect the siphon times and reflux time, which have been positively correlated with the ginsenoside contents. By substituting round bottom flasks in the same column, the relative standard deviation of the most fluctuated compound, ginsenoside Rb₁, was decreased from 24.6% to 5.02%. Scanning electron microscopy analysis confirmed that the breakdown of the surface of the ginseng powder in the Soxhlet extraction led to a better dissolution of ginsenosides, indicating that chloroform may promote the extraction of ginsenosides by disrupting the cell structure. Moreover, 70% methanol was regarded as the better solvent for extracting the ginsenosides. Overall, this work offers a practical and effective protocol for improving the accuracy and repeatability of Soxhlet extraction methodology for ginsenosides and other analytes.

© 2018 Xi'an Jiaotong University. Production and hosting by Elsevier B.V. This is an open access article under the CC BY-NC-ND license (<http://creativecommons.org/licenses/by-nc-nd/4.0/>).

1. Introduction

Extraction is an important step in analytical methodologies, as it constitutes the principal source of error and remains one of the most time-consuming one [1–3]. In practice, it is necessary to select appropriate extractions and solvents based on physico-chemical principles such as polarity and thermal stability, for enriching the desired compounds or removing the impurities [4–6]. Particularly, Soxhlet extraction, as a dynamic extraction and continuous reflux method, is commonly used for biological, pharmaceutical, food, and environmental analyses [7–9]. In order to significantly improve the efficiency of sample preparation, batch Soxhlet extraction with separate heat sources has been widely used. However, some unintended processes previously considered negligible, including the heating positions and the devices, have caused

significant content fluctuations, yet are rarely reported in batch Soxhlet extraction analysis using the same heat source [3].

Soxhlet extraction is the standard extraction protocol for the quality control of some herbal medicines in China [10] and other countries [11,12]. In the Chinese Pharmacopoeia 2015 edition for traditional Chinese medicines, the Soxhlet extraction method was used in 33 kinds of medicinal materials for quantitative analysis of plants such as ginseng and red ginseng [10]. Usually, the Soxhlet extraction was adjusted to allow a more complete movement of the grease components [13] and more effective protection of the chromatographic columns than the enzyme hydrolysis [14], ultrahigh pressure extraction [15], microwave-assisted extraction [16], solid extraction [17], and supercritical fluid extraction [18] approaches. However, in this study, we discovered serious ginsenoside content fluctuations in the batch Soxhlet extraction of ginseng and red ginseng using different extraction positions within the same device, which significantly influenced the quantification accuracy.

Considering that batch Soxhlet extraction is a universal issue, *Panax ginseng* was selected as a model sample to develop a

Peer review under responsibility of Xi'an Jiaotong University.

* Corresponding authors.

E-mail addresses: laichangjiang44@126.com (C.-J.-S. Lai), huangluqi01@126.com (L.-Q. Huang).

systematic protocol for screening the key factor causing the extraction content fluctuations. Under our developed protocol, the siphon times, reflux time, and corresponding contents in different Soxhlet extraction positions were comprehensively monitored. Association analysis was applied to discover the complex relationship between the negligible factors and the content fluctuations. Scanning electron microscopy (SEM), as a good platform, was also used to discover the mechanism behind the microscopic changes and the ginsenosides release, using different extraction methods [19–21]. In the United States Pharmacopoeia, methanol solvent is used for the extraction of ginseng, while *n*-butanol and chloroform are used in the Chinese Pharmacopoeia. Therefore, the microscopic changes in ginseng using different extraction solvents are also discussed in this paper. Association analysis and SEM analysis were used to identify the mechanism behind the content fluctuations in batch Soxhlet extraction for the first time. After removing the interfering factors, we were able to decrease the relative standard deviation of the most fluctuated compound, ginsenoside Rb₁, from 24.6% to 5.02%, meeting the provisions of the Chinese Pharmacopoeia [10]. The SEM analysis confirmed that the breakdown of the surface of the ginseng powder in the Soxhlet extraction led to a better dissolution of ginsenoside. This work offers a practical and effective protocol for improving the accuracy and repeatability of the Soxhlet extraction methodology for ginsenosides and other analytes, and proposes for the first time the unique role of chloroform in the extraction of ginsenosides.

2. Materials and methods

2.1. Chemicals and reagents

Reference standards of ginsenosides Rg₁ (GRg₁, ≥ 91.7%), Re (GRe, ≥ 92.3%), and Rb₁ (GRb₁, ≥ 93.7%) were purchased from the Chinese National Institutes for Food and Drug Control (Beijing, China). Analytical grade methanol, *n*-butanol, and chloroform were purchased from Beijing Chemical Works (Beijing, China); HPLC grade methanol and acetonitrile were purchased from Fisher Scientific (Geel, Belgium) and Merck (Darmstadt, Germany), respectively. Deionized water (18.2 MΩ/cm) was prepared by Barnstead GenPure UV/UF water purifier from Thermo Scientific (Langensfeld, Germany).

2.2. Sample preparation

Ginseng and red ginseng samples were purchased from Beijing Tongrentang (Dongzhimen Pharmacy, Beijing, China) in July 2016, and then were dried, crushed over 65 mesh screen (250 ± 9.9 μm), and stored in the dryer. According to the standard extraction of ginseng in the Chinese Pharmacopoeia (2015

Edition), the powders (~ 1 g) loaded into cellulose thimbles were Soxhlet extracted with chloroform (3 h each) using a standard six-hole water bath with 1.5 kW power (Fig. 1). After overnight soaking, the dried ginseng residues along with the filter paper were ultrasonic-extracted (250 W, 50 kHz) with 50 mL water saturated *n*-butanol for 30 min at room temperature. Then 25 mL subsequent filtrates were evaporated to dryness, dissolved in 5 mL HPLC grade methanol, and mixed well. The solution was filtered through a 0.22-μm PTFE filter from Pall Corporation (Ann Arbor, MI, USA) and stored at 4 °C prior to HPLC analysis.

2.3. HPLC analysis

All samples were analyzed on an Agilent 1260 HPLC-DAD system (Agilent Technologies, Palo Alto, CA, USA) for qualitative and quantitative analyses of ginsenosides in the ginseng and red ginseng at 30 °C using an Agilent Eclipse XDB-C18 column (4.6 mm × 250 mm, 5.0 μm) with the flow rate of 1 mL/min and the wavelength of 203 nm. The mobile phase consisted of water (A) and acetonitrile (B). The standard gradient elution program was according to the Chinese Pharmacopoeia [10]. This was 19% B at 0–35 min; 19%–29% B at 35–55 min; 29%–29% B at 55–70 min; 29%–40% B at 70–100 min; 40%–100% B at 100–106 min, then 100% B was maintained for 5 min to clean the column. The equilibration time was 5 min.

2.4. Systematic investigations of interference factors

In order to correct for systematic errors in the instruments and natural samples, the methodological parameters of the chemical markers (*i.e.* GRg₁, GRb₁, and GRe) including precision, linearity, and stability, were evaluated. Furthermore, the repeatability in the batch Soxhlet extraction was determined by two operators and the stability along with the recovery was also assessed. The intra-day precision was evaluated using the extract of 1 g ginseng powder (*n* = 6) in one day. The inter-day precision was determined over six successive days by quantification of the same extract. The stock extract was analyzed every 4 h to test the stability of the above three chemical markers at 25 °C. The linearity was assessed at the concentration of 0.0512–0.5120 mg/mL for GRg₁, 0.0503–0.5030 mg/mL for GRe, and 0.0537–0.5365 mg/mL for GRb₁, respectively. The interference factors in the Soxhlet extraction, including extraction position, siphon time [3], and reflux time [22], were simultaneously determined under the developed sampling method [10] using the same solvent. Finally, association analysis of the ginsenoside contents and these interference factors was comprehensively conducted.

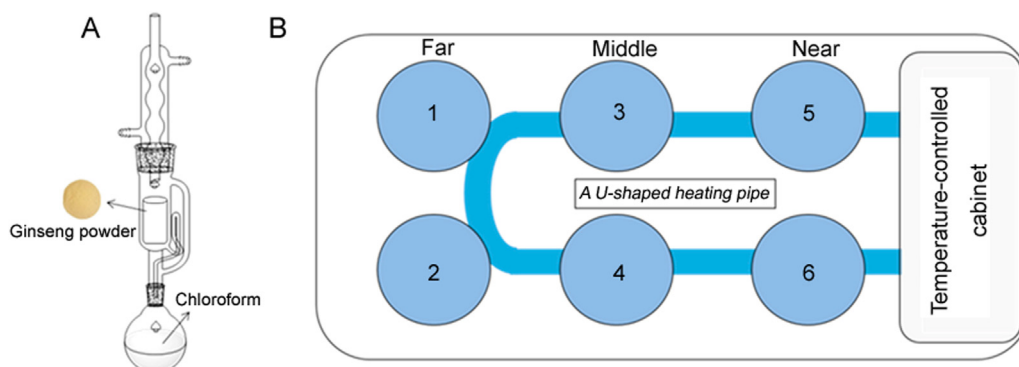


Fig. 1. The conventional Soxhlet extractor (A) and standard six-hole water bath (B) for the Soxhlet extraction of ginseng and red ginseng.

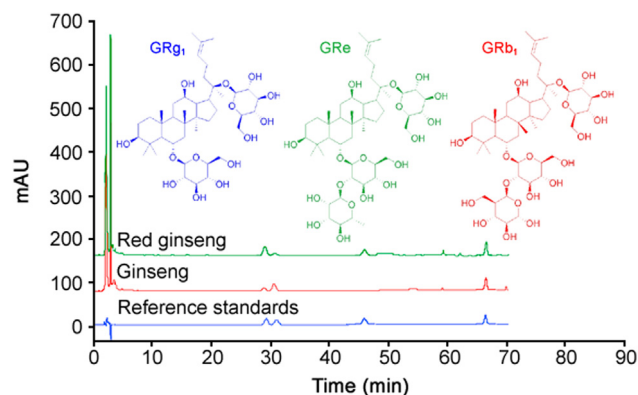


Fig. 2. The HPLC spectra of ginseng, red ginseng, and mixed reference standards.

2.5. Scanning electron microscopy (SEM) analysis

Ginseng powders were observed under the SU1510 SEM (Hitachi High-Technologies Corporation, Tokyo Japan) for morphological characterization before and after extraction. Five samples of the untreated residue, the ultrasound extracted residue using 50 mL of 70% methanol (USP Reference Standards) [23], the chloroform refluxed residue, the standard residue using the Chinese Pharmacopoeia [10], and the ultrasound extracted residue using *n*-butanol were used for the SEM analysis. The study on the role of the solvent in the extraction of ginsenosides from ginseng materials was processed by comparing the effects of different solvents on the morphological changes, which could indicate the ability of the release of intracellular ginsenosides into the extract indirectly. All ultrasound extractions were performed for 30 min at the frequency of 50 kHz and the ultrasonic power of 250 W. After drying the extracted residues at 60 °C in an air oven, all samples were fixed on a specimen holder with a carbon double-sided tape (NISSHIN EM Co., Ltd., Tokyo) and then sputtered with gold in a KYKY SBC-12 sputter-coater (KYKY Technology Co., Ltd., Beijing, China) to be examined with SEM.

3. Results and discussion

3.1. Issues with repeatability in batch Soxhlet extraction

HPLC-UV was used to analyze the ginsenosides in ginseng, in which GRg₁ (28.9 min), GRe (30.8 min), and GRb₁ (46.2 min) displayed good peak shapes and separations (Fig. 2). Under the set concentration ranges, the squared multiple correlation coefficients (R^2) of all determined ginsenosides were above 0.9991, and the intra-day and inter-day precisions were all below 4.43% (Table 1), indicating the accuracy of the instrument and the adopted separation method was sufficient. In addition, all extracted samples were stable for 36 consecutive hours and monitored every 4 h at 25 °C.

However, poor repeatability always appeared in the batch Soxhlet extraction with different positions. Initially, these

Table 1

The linearity, precision, and stability of the official HPLC-UV for ginseng.

Component	Curvilinear equation	R^2	Linearity range (mg/mL)	Precision (% RSD)		Stability (% RSD)
				Inter-day	Intra-day	
GRg ₁	$Y = 3115.4X - 10.8830$	0.9998	0.0512–0.5120	2.20	1.66	3.03
GRe	$Y = 2750.6X - 14.5050$	0.9997	0.0503–0.5030	0.28	2.06	1.26
GRb ₁	$Y = 2287.6X + 3.8394$	0.9991	0.0537–0.5365	0.60	4.43	2.26

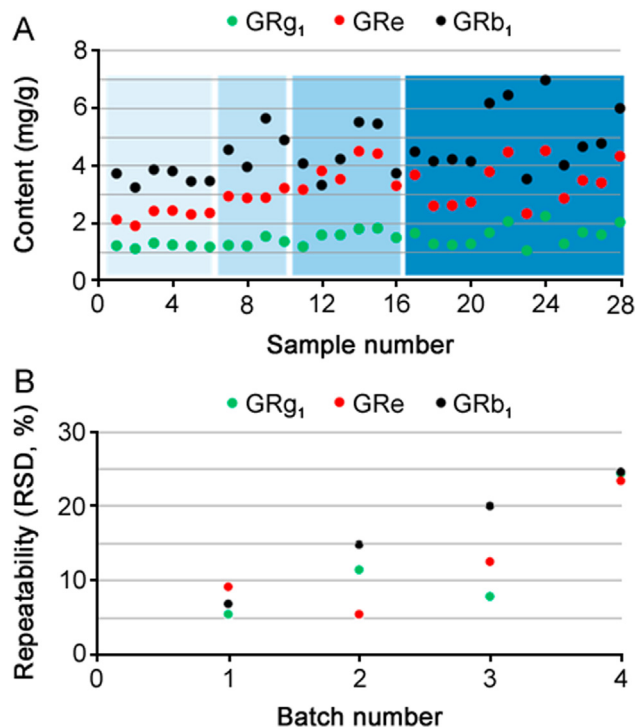


Fig. 3. The determined contents (A) and their corresponding repeatability (B) of ginsenosides. Especially, the No. 1–10 and No. 17–28 results were examined by the same operator on different days, and the No. 11–16 results were examined by another operator.

significant quantification fluctuations were speculated to be caused by artificial errors, so two operators, the No. 1–10 samples for the one and the No. 11–16 samples for the other, conducted repeatability studies on different days (Fig. 3A). However, the repeatability was still unsatisfactory. Traditionally, the use of more samples (9 batches, No. 17–28) could effectively eliminate the errors. Surprisingly, the relative standard deviation of the most variable, ginsenoside Rb₁, even reached 24.6% (Fig. 3B), indicating that more samples led to poorer quantification. Notably, the similar content change trends for GRb₁ and GRg₁ indicated that the instability of the ginsenosides was not the responsible factor. Thus, considering the good credibility of ultrasonic extraction followed by HPLC for ginsenosides [24], we began to speculate that some other factors in the Soxhlet extraction might be responsible for the poor repeatability.

3.2. Systematic association analyses of the Soxhlet extraction factors with the content fluctuations

While processing the repeatability test, we found the reflux time and droplet speed were different for the extraction holes in the far (Positions 1 and 2), middle (Positions 3 and 4), and near (Positions 5 and 6) positions in the U-type temperature regulator (Fig. 1B, and Table 2). Moreover, the fastest droplet speed extracted more ginsenosides. In order to elucidate the complex relationship

Table 2
Extraction efficiency of ginsenosides at different positions of the standard six-hole water bath.

Position	Reflux time (s/100 drops)	Siphon times (in 3 h)	Red ginseng			Ginseng		
			GRg ₁ (%)	GRe (%)	GRb ₁ (%)	GRg ₁ (%)	GRe (%)	GRb ₁ (%)
1	44	6.5	0.29	0.08	0.33	0.12	0.23	0.34
2	44	6.5	0.29	0.08	0.34	0.12	0.23	0.35
3	28	8.0	0.31	0.09	0.40	0.13	0.24	0.39
4	29	8.0	0.29	0.08	0.38	0.12	0.24	0.38
5	54	3.0	0.26	0.08	0.28	0.12	0.21	0.37
6	54	3.0	0.26	0.07	0.29	0.11	0.19	0.32

of the contents and the reflux time, the efficiency of all selected round flasks was first evaluated using the same volume of chloroform (~ 200 mL) under the conventional Soxhlet extractor (Fig. 1A) and consecutively tested 3 h in the same hole. When there were no significant differences for the mean reflux time per 100 drops of chloroform [24] and siphon times [3], the round flask would be selected to conduct further studies.

Unfortunately, using the same parameters, significant differences still appeared when the selected round flasks were used in different positions (Table 2). The samples from the two middle holes had the smallest mean reflux time to reach 100 drops, resulting in the largest siphon times, with 8.0 in 3 h. Moreover, the reflux time of the far holes were larger than those of the near ones. Meaningfully, the middle holes of the Soxhlet extractor showed the highest efficiency for sampling. The samples from the same column of holes had similar extraction efficiency (RSD < 5%).

Interestingly, for the first time, using association analysis, we discovered a strong relationship between the siphon times and ginsenosides contents in ginseng and red ginseng (Figs. 4A and B). Their R^2 values of the contents with the siphon times were all above 0.5348 in red ginseng and 0.8448 in ginseng, and even reached 0.9847 for GRe or GRg₁ in different types of samples. Moreover, the results between the reflux time per 100 drops with the contents confirmed the above good relationships (their R^2 all above 0.8448) (Figs. 4C and D), indicating the different positions of the Soxhlet extractor containing the U-type temperature regulator were the major factor causing poor repeatability. Meaningfully, the different extraction efficiencies of the different water-bath positions would significantly influence the accuracy of the quantification for ginsenosides, which was considered a negligible factor in previous studies. At the same time, it also suggested that the different positions of one water bath could have an effect on the

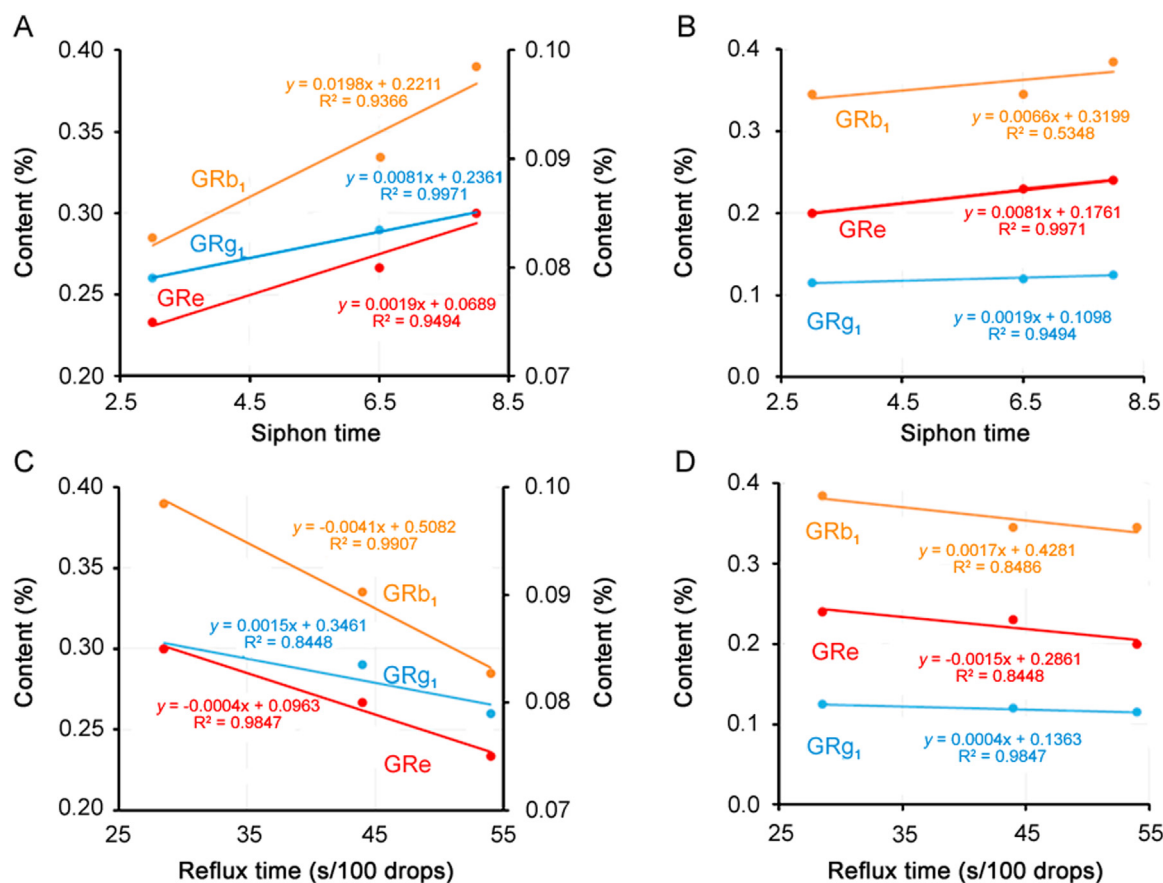


Fig. 4. The positive relationship between the siphon times (A and B) and reflux time (C and D) for ginseng (left) and red ginseng (right) samples.

Table 3
The recovery and repeatability of parallel soxhlet extraction for ginsenosides.

Component	Recovery (% , n = 9)			Repeatability (%, RSD, n = 6)
	Low (80%)	Med. (100%)	High (120%)	
GRg ₁	104.44	97.25	103.51	2.47
	97.43	102.05	98.83	
	106.88	101.95	99.39	
GRe	99.06	98.01	95.71	4.90
	104.15	101.27	98.24	
	98.88	102.55	95.29	
GRb ₁	96.67	106.21	104.09	5.02
	100.83	99.77	100.77	
	95.84	97.50	103.31	

extraction efficiency of ginsenosides. Therefore, more attention should be paid to the design of the temperature regulator for the water bath [3] in future batch Soxhlet extractions.

3.3. Accurate quantification of ginsenosides using the same column positions for the Soxhlet extraction

According to the above results, we used parallelized round bottom flasks to extract samples in the same column positions, the middle two holes (Positions 3 and 4), to re-determine the recovery and repeatability (Table 3). Fortunately, the recovery ranged from 95.29% to 106.88% and the repeatability was below 5.02%, indicating that this new method could meet the requirements of the Chinese Pharmacopoeia [10]. Moreover, this unintended extraction process solidly for the first time confirmed that the water-bath position for the Soxhlet extraction was critical to accurately quantify the ginseng ginsenosides. In tests of real samples, their concentrations of GRg₁, GRe, and GRb₁ in ginseng were 0.12%, 0.22%, and 0.36%, and in red ginseng were 0.30%, 0.09%, and 0.39%, respectively. Notably, in the comparison of the above complex optimized official sample preparation, simple ultrasonic extraction [24,25], with a short extraction time, low solvent consumption,

and good repeatability, is another choice for the accurate quantification of ginsenosides in future study.

3.4. Scanning electron microscopy for discovering the Soxhlet extraction mechanism for improving ginsenosides release from materials

In order to elucidate how the conventional Soxhlet extractor assists the extraction of ginsenosides from raw ginseng, SEM was used to examine the surface changes that could account for the sampling-triggered content release [21,26]. Compared with the untreated sample, there were serious structure changes on the surfaces of the samples treated using 70% methanol, chloroform, chloroform along with *n*-butanol, and *n*-butanol only (Figs. 5A-E), which were selected according to the ginseng extraction method in the U.S. Standard and Chinese Pharmacopoeia [10]. After Soxhlet extraction using chloroform only, slight cellular damage with some small particles was observed (Figs. 5A and D). In addition, the Soxhlet extraction effectively assisted sonication by disrupting the surface structure of the ginseng powder and rapidly releasing intracellular ginsenosides (Figs. 5B and D-F), which is the main by which Soxhlet extraction improves the extraction of ginsenosides. Therefore, the degree of damage to the surface wall of the ginseng powder was increased after being Soxhlet extracted by chloroform. In other words, it allowed more ginsenosides from the raw materials to be extracted by the following *n*-butanol. Notably, the significant differences in the penetrability and enrichment ability of the solvents in regards to the cell walls caused serious damage to the treated samples and varied concentrations, respectively. The chloroform reflux process will inevitably lead to the loss of effective components [27]. However, in our study, the ginsenoside contents at larger siphon times were higher than those at smaller siphon times, indicating that the loss of ginsenosides was less than that using ultrasonic-extraction with water saturated *n*-butanol. Therefore, for ginseng, chloroform promoted the extraction of ginsenosides by destroying the cell structure and not only the usual degreasing. Notably, the yields of ginsenosides ultrasonically extracted with 70% methanol were higher than those of the

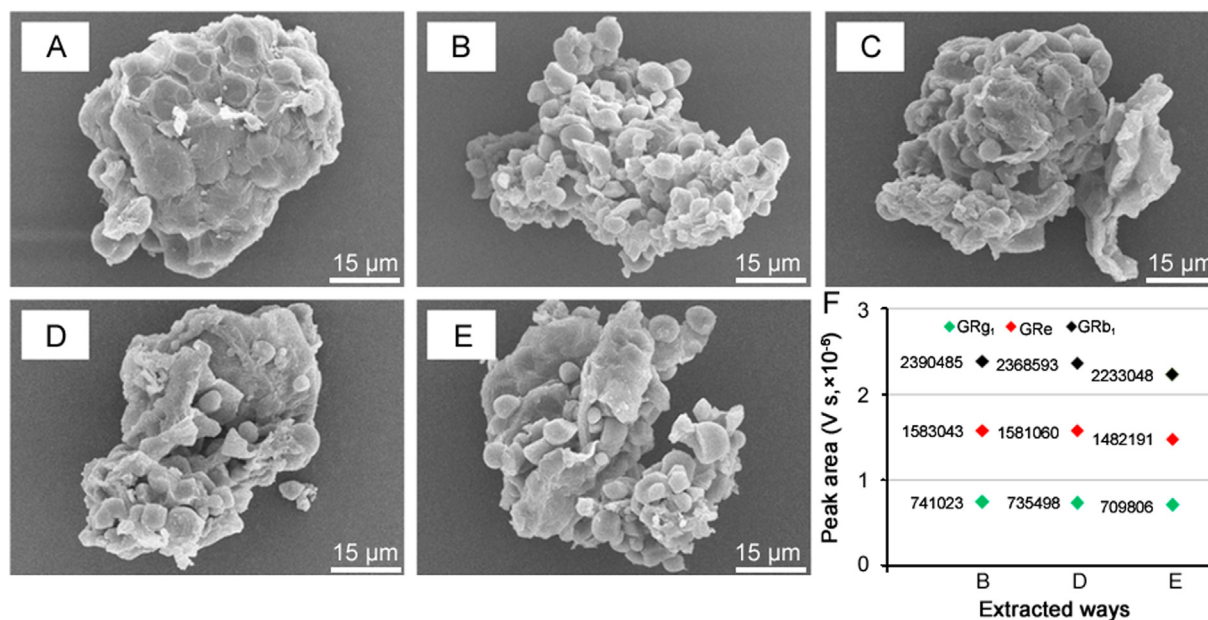


Fig. 5. Scanning electron microscopic (SEM) analyses and ginsenoside content comparisons using different sampling methods. The SEM images of the residues for untreated sample (A) and treated samples using ultrasound extraction with 70% methanol for 30 min (B), chloroform reflux for 3 h (C), chloroform reflux for 3 h along with *n*-butanol ultrasound extraction for 30 min (D), and *n*-butanol ultrasound extraction for 30 min (E) were recorded. The mean peak areas of ginsenosides ($n = 3$) of the three ways of extraction were compared (F). In particular, the peak area of sample B was zoomed in five times due to the fact that the solvent volume was 50 mL for 1 g ginseng powder.

chloroform reflux with *n*-butanol ultrasound (Fig. 5F), indicating the 70% methanol was the better solvent for extracting the ginsenosides.

4. Conclusion

This study demonstrates a standard protocol that systematically investigates some important factors of batch Soxhlet extraction resulting in content fluctuations. Interestingly, we were the first who discovered the different water-bath positions of the conventional Soxhlet extractor, considering a negligible factor in previous studies, could significantly cause the poor repeatability of ginsenosides. In particular, the unstable ginsenoside Rb₁ was above 24.6% using batch Soxhlet extraction. After processing the developed protocol, different Soxhlet extraction positions of the same device showed significant differences in efficiency. In addition, using correlation analysis for the first time, the reflux time and siphon times were found to be in good linear agreement with their corresponding ginsenoside contents. Therefore, the water-bath position of the Soxhlet extraction was a key factor assisting the extraction of ginsenosides from raw ginseng material. In addition, SEM confirmed that Soxhlet extraction improves ultrasound extraction by disrupting the surface of the ginseng powder to effectively release the cellular ginsenosides, not just the previously considered defatting. In real sample analyses, the recovery and repeatability in the same column positions at the middle holes could meet the requirements of the Chinese Pharmacopoeia, indicating that the efficiency of different Soxhlet extraction positions should be systematically investigated in further studies. Furthermore, the content results of the official sample preparations showed that ultrasonic extraction with 70% methanol was feasible and credible for the accurate quantification of the ginsenosides in ginseng.

Conflicts of interest

The authors declare that there are no conflicts of interest.

Acknowledgments

The financial support of the key project at the central government level: The Ability Establishment of Sustainable Use for Valuable Chinese Medicine Resources (No. 2060302), the Independent Research Grant of National Resource Center for Chinese Materia Medica, China Academy of Chinese Medical Sciences (No. ZZXT201608), and the National Natural Science Foundation of China (No. 81603293), was appreciated.

References

- [1] R. Chen, F. Meng, S. Zhang, et al., Effects of ultrahigh pressure extraction conditions on yields and antioxidant activity of ginsenoside from ginseng, *Sep. Purif. Technol.* 66 (2009) 340–346.
- [2] C.W. Huie, A review of modern sample-preparation techniques for the

- extraction and analysis of medicinal plants, *Anal. Bioanal. Chem.* 373 (2002) 23–30.
- [3] M.D. Luque de Castro, F. Priego-Capote, Soxhlet extraction: past and present panacea, *J. Chromatogr. A* 1217 (2010) 2383–2389.
- [4] X. Yang, S.C. Fan, Progress in traditional Chinese medicine extraction method, *Asia-Pac. Trad. Med.* 8 (2012) 194–196.
- [5] A. Mustafa, C. Turner, Pressurized liquid extraction as a green approach in food and herbal plants extraction: A review, *Anal. Chim. Acta* 703 (2011) 8–18.
- [6] A. Oniszczuk, R. Podgórski, Influence of different extraction methods on the quantification of selected flavonoids and phenolic acids from *Tilia cordata* inflorescence, *Ind. Crop Prod.* 76 (2015) 509–514.
- [7] J. Ryu, H.W. Lee, J. Yoon, et al., Effect of hydrothermal processing on ginseng extract, *J. Gins. Res.* 41 (2017) 572–577.
- [8] Y. Zhou, J. Zheng, R.Y. Gan, et al., Optimization of ultrasound-assisted extraction of antioxidants from the Mung Bean Coat, *Molecules* 22 (2017) 638.
- [9] P.L. Cloutier, F. Fortin, P.E. Groleau, et al., QuEChERS extraction for multi-residue analysis of PCBs, PAHs, PBDEs and PCDD/Fs in biological samples, *Talanta* 165 (2017) 332–338.
- [10] National Commission of Chinese Pharmacopoeia, Pharmacopoeia of the People's Republic of China, 2015 ed., Beijing, China, 2015.
- [11] European Directorate for the Quality of the Medicines (EDQM), European Pharmacopoeia 8.0, Strassbourg, France, 2014.
- [12] S. Masala, U. Rannug, R. Westerholm, Pressurized liquid extraction as an alternative to the Soxhlet extraction procedure stated in the US EPA method TO-13A for the recovery of polycyclic aromatic hydrocarbons adsorbed on polyurethane foam plugs, *Anal. Methods* 6 (2014) 8420–8425.
- [13] L.N. Zhou, W.L. Hao, S.L. Wu, et al., Effects of different accelerated solvent extraction conditions on lipids extraction from *Chlorella sorokiniana*, *Guangdong Agr. Sci.* 43 (2016) 126–132.
- [14] C.J.S. Lai, T. Tan, S.L. Zeng, et al., An enzymatic protocol for absolute quantification of analogues: Application to specific protopanaxadiol-type ginsenosides, *Green. Chem.* 17 (2015) 2580–2586.
- [15] S. Zhang, R. Chen, H. Wu, et al., Ginsenoside extraction from *Panax quinquefolium* L. (American ginseng) root by using ultrahigh pressure, *J. Pharm. Biomed. Anal.* 41 (2006) 57–63.
- [16] Y.Y. Shu, M.Y. Ko, Y.S. Chang, Microwave-assisted extraction of ginsenosides from ginseng root, *Microchem. J.* 74 (2003) 131–139.
- [17] X. Xu, S. Liang, X. Meng, et al., A molecularly imprinted polymer for the selective solid-phase extraction of dimethomorph from ginseng samples, *J. Chromatogr. B* 988 (2015) 182–186.
- [18] C. Oba, M. Ota, K. Nomura, et al., Extraction of nobiletin from *Citrus Unshiu* peels by supercritical fluid and its CRE-mediated transcriptional activity, *Phytomedicine* 27 (2017) 33–38.
- [19] A. Faltermaier, M. Zarnkow, T. Becker, et al., Common wheat (*Triticum aestivum* L.): evaluating microstructural changes during the malting process by using confocal laser scanning microscopy and scanning electron microscopy, *Eur. Food Res. Technol.* 241 (2015) 239–252.
- [20] F. Dahmoune, B. Nayak, K. Moussi, et al., Optimization of microwave-assisted extraction of polyphenols from *Myrtus communis* L. leaves, *Food Chem.* 166 (2015) 585–595.
- [21] J. Liu, Y. Liu, Z.H. Zhang, et al., Correlation of cultivation time of *Panax ginseng* with metabolic profiles of nine ginsenosides and mRNA expression of genes encoding major biosynthetic enzymes, *Acta Physiol. Plant.* 38 (2016) 51.
- [22] W.F. Lv, M.Y. Ding, R. Zheng, Isolation and quantitation of amygdalin in *Apricot-kernel* and *Prunus tomentosa* Thunb. by HPLC with solid-phase extraction, *J. Chromatogr. Sci.* 43 (2005) 383–387.
- [23] The United States Pharmacopoeial Convention, herbal medicines compendium, *Panax ginseng* Steamed Root and Rhizome of Version 0.2, United States, 2016, (<https://hmc.usp.org/monographs/panax-ginseng-steamed-root-and-rhizome-0-2>).
- [24] B. Zhang, R. Yang, C.Z. Liu, Microwave-assisted extraction of chlorogenic acid from flower buds of *Lonicera japonica* Thunb., *Sep. Purif. Technol.* 62 (2008) 480–483.
- [25] S.P. Li, C.F. Qiao, Y.W. Chen, et al., A novel strategy with standardized reference extract qualification and single compound quantitative evaluation for quality control of *Panax notoginseng* used as a functional food, *J. Chromatogr. A* 1313 (2013) 302–307.
- [26] H.K. Kala, R. Mehta, K.K. Sen, et al., Strategizing method optimization of microwave-assisted extraction of plant phenolics by developing standard working principles for universal robust optimization, *Anal. Methods* 9 (2017) 2089–2103.
- [27] W. Dong, Y. Qian, X. Zhu, et al., Determination of ginsenosides at the presence of phospholipids, *J. China Pharm. Univ.* 26 (1995) 282–285.



Contents lists available at ScienceDirect

Journal of Pharmaceutical Analysis

journal homepage: www.elsevier.com/locate/jpa
www.sciencedirect.com



Original Research Article

Molecular docking studies of human MCT8 protein with soy isoflavones in Allan-Herndon-Dudley syndrome (AHDS)

Divya Shaji

Department of Pediatrics, Aichi Medical University, Nagakute, Aichi, Japan

ARTICLE INFO

Article history:

Received 24 December 2017

Received in revised form

28 June 2018

Accepted 2 July 2018

Available online 3 July 2018

Keywords:

Molecular docking

MCT8

AHDS

Soy isoflavones

Daidzein

Genistein

ABSTRACT

Monocarboxylate transporter-8 (MCT8) is a specific thyroid hormone transporter, essential for the uptake of thyroid hormone into target tissues. Mutations in the MCT8 gene have been identified as the cause of Allan-Herndon-Dudley syndrome (AHDS). It has been reported that soy isoflavones influence thyroid hormone system and can interact with thyroid hormone transporter proteins. Therefore, the present study aimed to find out whether soy isoflavones (genistein, daidzein and glycitein) can be used as a natural inhibitor to target MCT8 in AHDS. Docking studies were performed for soy isoflavones in order to evaluate their binding affinity to MCT8 protein using AutoDock4 (version 4.2.6) and AutoDock Vina. After docking, the ligands were ranked according to their binding energy and the best lead compound was selected based on the least binding energy. The docking results indicated that daidzein possesses the lowest binding energy against MCT8. Moreover, it was found that the residues PRO-338, HIS-341, and GLU-348 were involved in hydrogen bond interactions with genistein and daidzein. This study suggests that daidzein is a promising natural inhibitor to target MCT8 in AHDS.

© 2018 Xi'an Jiaotong University. Production and hosting by Elsevier B.V. This is an open access article under the CC BY-NC-ND license (<http://creativecommons.org/licenses/by-nc-nd/4.0/>).

1. Introduction

Thyroid hormone plays an important role in our body with widespread biological actions. Adequate levels of thyroid hormone are crucial for the development and proper function of multiple organs [1,2]. Thyroid hormone exists in two forms: T4 (3,3',5,5'-tetraiodothyronine) and T3 (3,3',5-triiodothyronine). The biological activity of thyroid hormone is related to the level of T3 within the cell. MCT8 (monocarboxylate transporter 8) protein is a transporter specific for T3 [1]. The MCT8 gene is located in Xq13 and mutations in MCT8 are responsible for an X-linked condition, known as the Allan-Herndon-Dudley syndrome (AHDS) showing high serum T₃ levels in affected male patients [1,2].

Currently, there is no effective treatment available for AHDS. Hence, there is an urgent need for the identification and validation of novel drug lead compounds for treating AHDS. Therefore, this study aimed to identify the natural potent inhibitors of MCT8 from soy isoflavones. While isoflavones occur in many types of legumes, soybean contains the highest concentration of isoflavones. Genistein, daidzein and glycitein are the soy isoflavones typically accounting for 50%, 40% and 10%, respectively [3]. Due to their chemical structure, the isoflavones can bind to estrogen receptors. As a result of this binding,

isoflavones inhibit and promote the expression of estrogen-sensitive genes [4]. Previous researches have shown that the occurrence of breast cancer is lower in Asian individuals than in other populations because of the high soy consumption as part of their regular diet [3,4].

Soy isoflavones influence thyroid hormone system and can interact with thyroid hormone transporter proteins [5,6]. In vitro and in vivo studies have indicated that genistein and daidzein are the potent inhibitors of thyroid peroxidase [5]. Moreover, soy isoflavones are the potent ligands for transthyretin in serum and cerebrospinal fluid [5]. However, soy isoflavones have not been studied against MCT8. So this study made an attempt to find out whether soy isoflavones (genistein, daidzein and glycitein) can be used as a natural inhibitor to target MCT8 in AHDS.

2. Materials and methods

2.1. Drug-likeness of the ligands

Genistein, daidzein and glycitein were considered as ligands. SwissADME tool [7] was used to calculate the molecular properties of the ligands. The molecular properties were screened based on the "Lipinski's rule of five" [8,9]. The total polar surface area (TPSA) and the number of rotatable bonds were also calculated using SwissADME [7].

Peer review under responsibility of Xi'an Jiaotong University.

E-mail address: divyas.bioinfo@gmail.com

<https://doi.org/10.1016/j.jpha.2018.07.001>

2095-1779/© 2018 Xi'an Jiaotong University. Production and hosting by Elsevier B.V. This is an open access article under the CC BY-NC-ND license (<http://creativecommons.org/licenses/by-nc-nd/4.0/>).

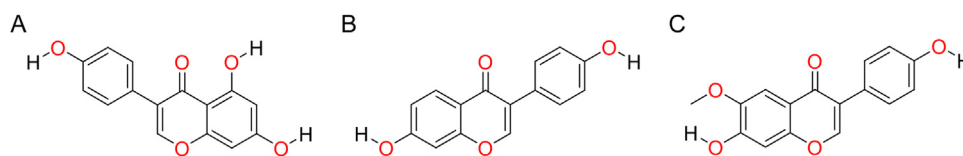


Fig. 1. Chemical structures of (A) genistein, (B) daidzein and (C) glycitein.

Table 1
Molecular properties of the ligands.

Ligand	Num. H-bond acceptors	Num. H-bond donors	MLOGP	Number of rotatable bonds	Molecular weight (g/mol)	TPSA (Å ²)
Genistein	5	3	0.52	1	270.24	90.90
Daidzein	4	2	1.08	1	254.24	70.67
Glycitein	5	2	0.77	2	284.26	79.90

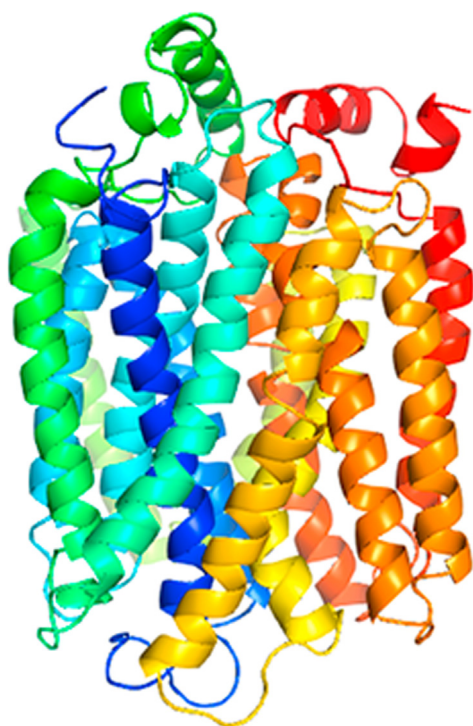


Fig. 2. 3D structure of MCT8 protein by multi-template homology modeling [11]. This 3D model of MCT8 was predicted based on multiple templates (PDB IDs: 1pw4A, 4u4tA, 4ikxA, 4j05A, and 4gbyA) using the advanced modeling feature of MODELLERv9.17 [12,13].

2.2. Protein preparation for docking

The human MCT8 protein is not available in protein data bank (PDB) [10]. The protein used in the docking study was obtained through multi-template based homology modeling [11]. In the previous study [11], a good-quality 3D model of MCT8 was predicted based on multiple templates (PDB IDs: 1pw4A, 4u4tA, 4ikxA, 4j05A, and 4gbyA) using the advanced modeling feature of MODELLERv9.17 [12,13]. The structure refinement of modeled protein was done by ModRefiner [14]. For docking, all water molecules were removed and polar hydrogen atoms were added to the refined model using AutoDock Tools (ADT) [15]. The prepared protein was saved in PDBQT format.

2.3. Ligand preparation for docking

The ligands were downloaded from Pubchem Database [16,17] and converted to PDB [10] file format by using Openbabel software

[18]. The ligands were prepared using ADT [15]. Gasteiger charge was assigned to the ligands. The prepared ligands were saved in PDBQT format.

2.4. Molecular docking

AutoDock4 (version 4.2.6) [15] and AutoDock Vina [19] were used for molecular docking studies. AutoGrid program supplied with AutoDock4 [15] was used for the preparation of grid maps. The grid box size was set at 76, 70, and 76 Å for x, y, and z, respectively. The spacing between the grid points was 1.0 Å. The grid centre was set at 30.375, 17.112, and -37.003 Å for x, y, and z, respectively. The Lamarckian Genetic Algorithm (LGA) was chosen to search for the best conformers. During the docking process, a maximum of 10 conformers was considered for each ligand. All the docking processes were performed with the default parameters of AutoDock 4 [15]. Population size was set to 150, maximum number of evaluations 2,500,000, maximum number of generations 27,000, maximum number of top individual that automatically survived 1, gene mutation rate 0.02 and crossover rate 0.8. AutoDock4 [15] and AutoDock Vina [19] were compiled and run under Windows 10 Operating System. All figures with structure representations were produced using Discovery Studio Visualizer [20].

3. Results and discussion

3.1. Drug-likeness of the ligands

“Lipinski’s rule of five” [8,9] is used to evaluate the drug-likeness of a chemical compound. The molecular properties of a chemical compound consist of molecular weight, hydrogen bond donor, hydrogen bond acceptor, and log *P*. “Lipinski’s rule of five” states that an orally active drug has no more than one violation of the following criteria: (1) less than 5 hydrogen-bond donors, (2) less than 10 hydrogen-bond acceptors, (3) a molecular mass less than 500 Da, and (4) log *P* not greater than 5. All ligands of the present study met the requirements of “Lipinski’s rule of five”. The other significant properties such as total polar surface area (TPSA) and the number of rotatable bonds were also calculated. TPSA of a compound should be less than 140 Å² and the number of rotatable bonds should be less than 10 [21]. All the ligands had the above properties. The chemical structures of the ligands are shown in Fig. 1 and their molecular properties are shown in Table 1.

3.2. Molecular docking

Molecular docking is an important tool in pharmaceutical research [22]. The molecular docking approach can be used to model

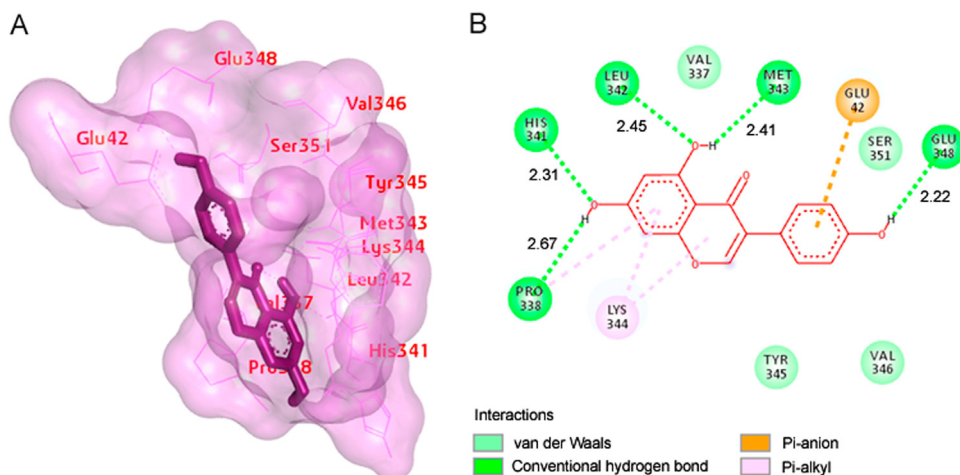


Fig. 3. (A) The output of AutoDock showing the binding site residues of MCT8 protein with the ligand genistein. The residues in the binding site are shown in red color. Genistein is shown in purple stick format. (B) 2D diagram showing the types of contacts formed between MCT8 and genistein. The green dotted lines indicate H-bond interactions between MCT8 and genistein. The values adjacent to the green dotted lines indicate their distance.

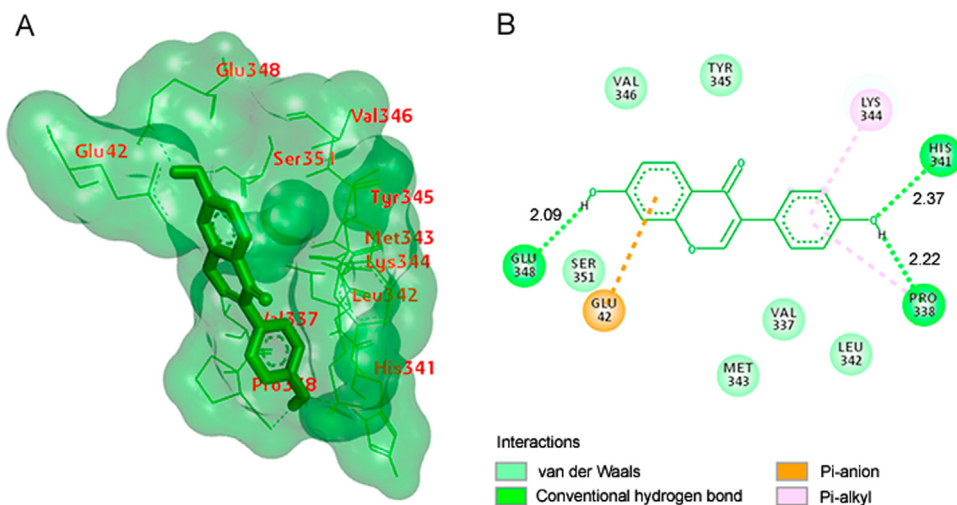


Fig. 4. (A) The output of AutoDock showing the binding site residues of MCT8 protein with the ligand daidzein. The residues in the binding site are shown in red color. Daidzein is shown in green stick format. (B) 2D diagram showing the types of contacts formed between MCT8 and daidzein. The green dotted lines indicate H-bond interactions between MCT8 and daidzein. The values adjacent to the green dotted lines indicate their distance.

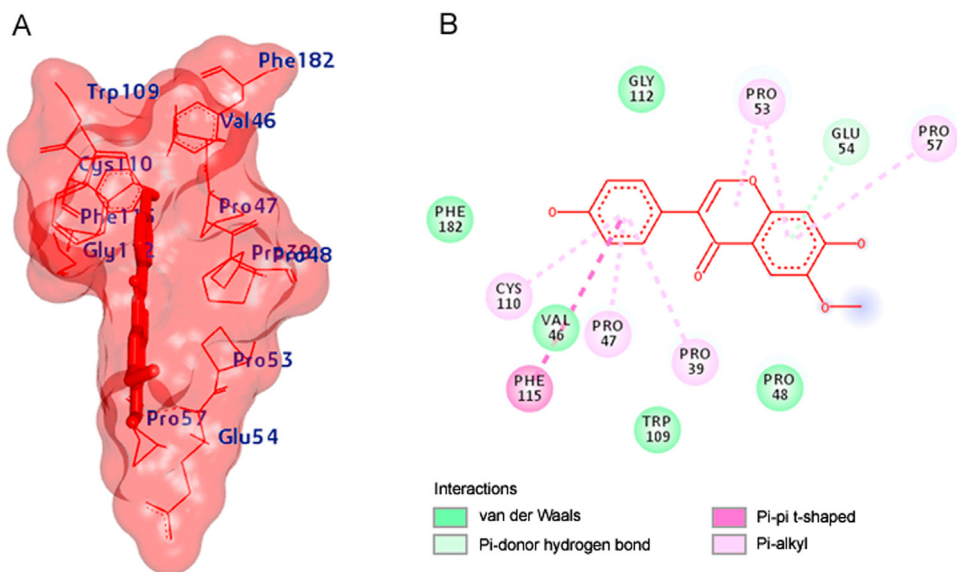


Fig. 5. (A) The output of AutoDock showing the binding site residues of MCT8 protein with the ligand glycitein. The residues in the binding site are shown in blue color. Glycitein is shown in red stick format. (B) 2D diagram showing the types of contacts formed between MCT8 and glycitein.

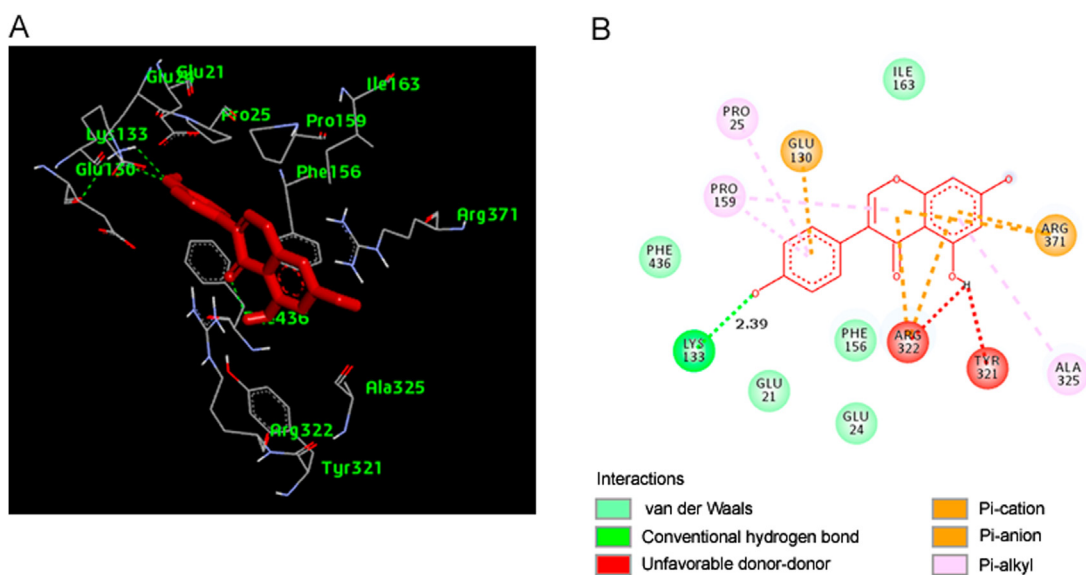


Fig. 6. (A) The output of AutoDock Vina showing the binding site residues of MCT8 protein with the ligand genistein. The residues in the binding site are shown in green color. Genistein is shown in red stick format. (B) 2D diagram showing the types of contacts formed between MCT8 and genistein. The green dotted lines indicate H-bond interactions between MCT8 and genistein. The values adjacent to the green dotted lines indicate their distance.

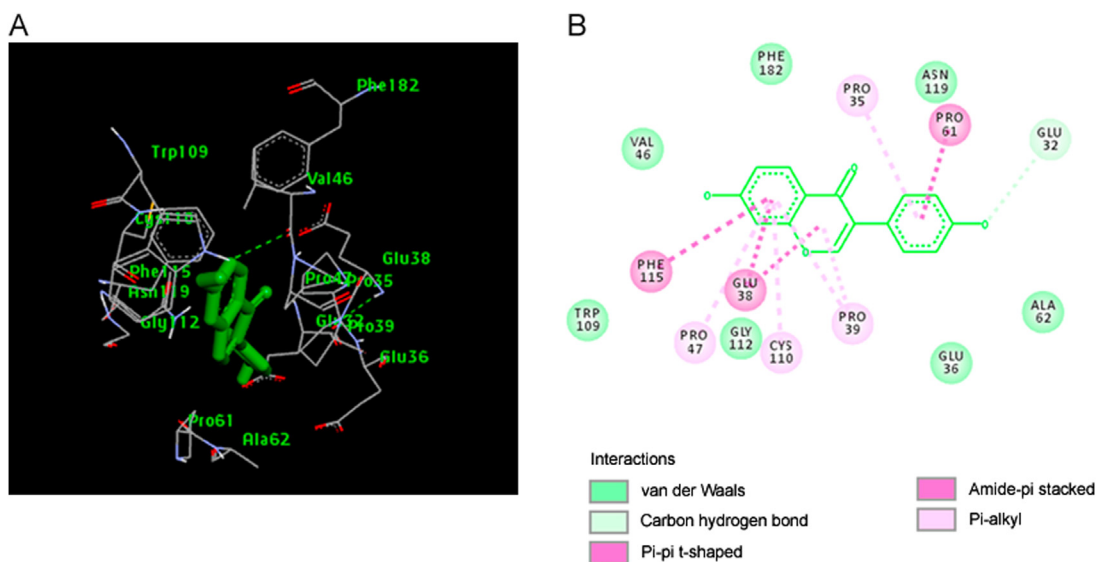


Fig. 7. (A) The output of AutoDock Vina showing the binding site residues of MCT8 protein with the ligand daidzein. The residues in the binding site are shown in green color. Daidzein is shown in green stick format. (B) 2D diagram showing the types of contacts formed between MCT8 and daidzein.

the interaction between a ligand and a protein at the atomic level [22,23]. The docking process involves two basic steps: prediction of the ligand conformation and assessment of the binding affinity [22]. These two steps are related to sampling methods and scoring schemes, respectively [22].

Docking studies were performed for 3 compounds in order to evaluate their binding affinity to MCT8 protein using AutoDock4 (version 4.2.6) [15] and AutoDock Vina [19]. The 3D structure of the MCT8 protein is shown in Fig. 2. The results were analyzed based on the binding energies of the docked complexes. AutoDock4 [15] and AutoDock Vina [19] generated 10 poses for each ligand. The selection of the best pose was done on the least binding energy between the ligand and the protein. After docking, the ligands were ranked according to their binding energy.

3.2.1. Docked results with AutoDock4

All the ligand molecules were docked against MCT8 using AutoDock4 [15]. The best selected pose of MCT8-genistein docked

complex (binding energy -5.76 kcal/mol) with binding site residues is shown in Fig. 3A. The hydrogen bonds and the types of contacts involved in MCT8-genistein complex are shown in Fig. 3B. It was observed that PRO-338, HIS-341, LEU-342, MET-343 and GLU-348 were involved in hydrogen bond interactions.

The best selected pose of MCT8-daidzein docked complex (binding energy -6.22 kcal/mol) with binding site residues is shown in Fig. 4A. The hydrogen bonds and the types of contacts involved in MCT8-daidzein complex are shown in Fig. 4B. It was observed that PRO-338, HIS-341, and GLU-348 were involved in hydrogen bond interactions.

The best selected pose of MCT8-glycitein docked complex (binding energy -5.54 kcal/mol) with binding site residues is shown in Fig. 5A. The types of contacts involved in MCT8-glycitein complex are shown in Fig. 5B. The results showed that there were no hydrogen bonds formed between MCT8 and glycitein.

The docking with AutoDock4 showed that daidzein was the best scored compound against MCT8 with the lowest binding energy.

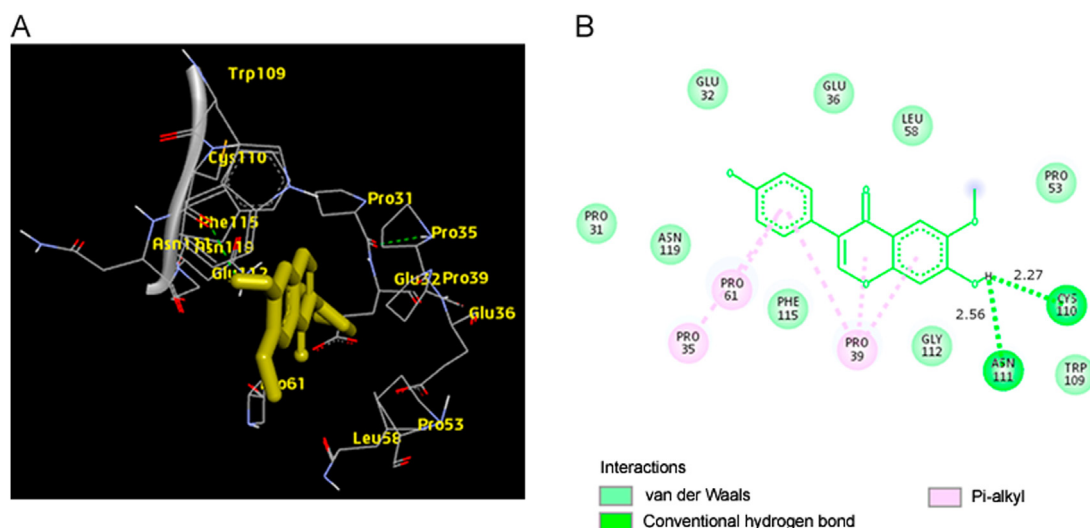


Fig. 8. (A) The output of AutoDock Vina showing the binding site residues of MCT8 protein with the ligand glycitein. The residues in the binding site are shown in yellow color. Glycitein is shown in yellow stick format. (B) 2D diagram showing the types of contacts formed between MCT8 and glycitein. The green dotted lines indicate H-bond interactions between MCT8 and glycitein. The values adjacent to the green dotted lines indicate their distance.

Table 2
Binding energies of the ligands.

Ligand	Binding energy calculated by AutoDock4 (kcal/mol)	Binding energy calculated by AutoDock Vina (kcal/mol)
Genistein	– 5.76	– 8.6
Daidzein	– 6.22	– 8.6
Glycitein	– 5.54	– 8.5

3.2.2. Docked results with AutoDock Vina

The ligands were docked against MCT8 using AutoDock Vina [19]. The best scored conformation was selected by considering the lowest binding energy between the protein and the ligand. The best selected pose of MCT8-genistein docked complex (binding energy –8.6 kcal/mol) predicted by AutoDock Vina is shown in Fig. 6A. The 2D diagram showing the hydrogen bonds and the types of contacts involved in MCT8-genistein complex is shown in Fig. 6B. The results showed that genistein interacted with MCT8 by forming hydrogen bonds with LYS-133.

The best docking pose of MCT8-daidzein docked complex (binding energy –8.6 kcal/mol) is shown in Fig. 7A. The types of contacts involved in MCT8-daidzein complex is shown in Fig. 7B. There were no hydrogen bonds formed between MCT8 and daidzein.

The best docking pose of MCT8-glycitein complex (binding energy –8.5 kcal/mol) is shown in Fig. 8A. The 2D diagram showing the hydrogen bonds and the types of contacts involved in MCT8-glycitein complex is shown in Fig. 8B. It was observed that CYS-110 and ASN-111 were involved in hydrogen bond interactions.

3.2.3. Analysis of the docked results

The docking results predicted by AutoDock4 [15] were compared to those of AutoDock Vina [19]. Docking analysis showed that there were hydrogen bonds formed between MCT8 and the inhibitors used. Opposite to the results of AutoDock4 [15], AutoDock Vina [19] generated hydrogen bonds in MCT8-glycitein interaction. Opposite to the results of AutoDock Vina, AutoDock generated hydrogen bonds in MCT8-daidzein interaction. Moreover, van der Waals interactions were also involved in addition to hydrogen bonds. It is important to point out that both compounds, genistein and daidzein, have hydrogen bonds with residues PRO-338, HIS-341 and GLU-348.

The best lead compound was selected in terms of binding energy. The binding energies of the ligands calculated by AutoDock4 [15] and AutoDock Vina [19] are shown in Table 2. Based on the analysis with AutoDock Vina [19], it was observed that binding energies of the three compounds were almost the same. Docking studies with AutoDock4 [15] and AutoDock Vina [19] showed that the natural compound Daidzein showed the lowest binding energy value of –6.22 and –8.6 kcal/mol, respectively (Table 2). Based on these findings, gaidzein can be used as a natural inhibitor to target MCT8 in AHDS. However, daidzein should be subjected to further investigation using in vitro studies.

4. Conclusion

Recently, many researches have focused on the identification of inhibitors from natural sources. This study concludes that daidzein is an effective lead compound which will be useful for the design of novel less toxic and highly efficient drugs for the treatment of AHDS. Daidzein should be subjected to further experimental study in order to confirm this finding. This study also identified that PRO-338, HIS-341 and GLU-348 of MCT8 play an important role in hydrogen bonding with genistein and daidzein.

Conflicts of interest

The authors declare that there are no conflicts of interest.

References

- [1] C.E. Schwartz, R.E. Stevenson, The MCT8 thyroid hormone transporter and Allan–Herndon–Dudley syndrome, *Best. Pract. Res. Clin. Endocrinol. Metab.* 21 (2007) 307–321.
- [2] W.M. Vander Deure, R.P. Peeters, T.J. Visser, Molecular aspects of thyroid hormone transporters, including MCT8, MCT10, and OATPs, and the effects of genetic variation in these transporters, *J. Mol. Endocrinol.* 44 (2010) 1–11.
- [3] F.J. He, J.Q. Chen, Consumption of soybean, soy foods, soy isoflavones and breast cancer incidence: differences between Chinese women and women in Western countries and possible mechanisms, *Food Sci. Human. Wellness* 2 (2013) 146–161.
- [4] S. Ziaei, R. Halaby, Dietary isoflavones and breast cancer risk, *Medicines* 4 (2017) 18.
- [5] B. Radović, B. Mentrup, J. Köhrlé, Genistein and other soya isoflavones are

- potent ligands for transthyretin in serum and cerebrospinal fluid, *Br. J. Nutr.* 95 (2006) 1171–1176.
- [6] S.T.C. Lima, T.L. Merrigan, E.D. Rodrigues, Synthetic and plant derived thyroid hormone analogs, *Thyroid Parathy. Dis.- New Insights into some Old. some New Issues* (2012) 221–236.
- [7] A. Daina, O. Michielin, V. Zoete, SwissADME: a free web tool to evaluate pharmacokinetics, drug-likeness and medicinal chemistry friendliness of small molecules, *Sci. Rep.* 7 (2017) 42717.
- [8] C.A. Lipinski, Drug-like properties and the causes of poor solubility and poor permeability, *J. Pharmacol. Toxicol. Methods* 44 (2000) 235–249.
- [9] C.A. Lipinski, F. Lombardo, B.W. Dominy, et al., Experimental and computational approaches to estimate solubility and permeability in drug discovery and development settings, *Adv. Drug Deliv. Rev.* 23 (1997) 3–25.
- [10] H.M. Berman, J. Westbrook, Z. Feng, et al., The protein data bank, *Nucleic Acids Res.* 28 (2000) 235–242.
- [11] D. Shaji, Multi-template homology modeling of human MCT8 protein, *Int. J. Adv. Res.* 5 (2017) 1025–1036.
- [12] A. Šali, L. Potterton, F. Yuan, et al., Evaluation of comparative protein modeling by MODELLER, *Protein. Struct. Funct. Bioinform.* 23 (1995) 318–326.
- [13] N. Eswar, B. Webb, M.A. Martin-Renom, et al., Comparative protein structure modeling using modeller, *Curr. Protoc. Bioinform.* 15 (2006) 5.6.1–5.6.32.
- [14] D. Xu, Y. Zhang, Improving the physical realism and structural accuracy of protein models by a two-step atomic-level energy minimization, *Biophys. J.* 101 (2011) 2525–2534.
- [15] G.M. Morris, R. Huey, W. Lindstrom, et al., AutoDock4 and AutoDockTools4: automated docking with selective receptor flexibility, *J. Comput. Chem.* 30 (2009) 2785–2791.
- [16] NCBI-PubChem Compound database, (<http://pubchem.ncbi.nlm.nih.gov>).
- [17] D.L. Wheeler, T. Barrett, D.A. Benson, et al., Database resources of the national center for biotechnology information, *Nucleic Acids Res.* 36 (2007) D13–D21.
- [18] N.M. O'Boyle, M. Banck, C.A. James, et al., Open Babel: an open chemical toolbox, *J. Cheminf.* 3 (2011) 33.
- [19] O. Trott, A.J. Olson, AutoDock Vina: improving the speed and accuracy of docking with a new scoring function, efficient optimization, and multi-threading, *J. Comput. Chem.* 31 (2010) 455–461.
- [20] A.D.S. Visualizer, Version 4. 5. Softw. Vis. Anal. Protein Struct. (2017), < <http://www.accelrys.com> > .
- [21] D.F. Veber, S.R. Johnson, H.Y. Cheng, et al., Molecular properties that influence the oral bioavailability of drug candidates, *J. Med. Chem.* 45 (2002) 2615–2623.
- [22] X.Y. Meng, H.X. Zhang, M. Mezei, et al., Molecular docking: a powerful approach for structure-based drug discovery, *Curr. Comput. Aided Drug Des.* 7 (2011) 146–157.
- [23] B.J. McConkey, V. Sobolev, M. Edelman, The performance of current methods in ligand–protein docking, *Curr. Sci.* 83 (2002) 845–856.



Original Research Article

Mass spectrometry detection of basic drugs in fast chiral analyses with vancomycin stationary phases

Hongyue Guo^a, M. Farooq Wahab^a, Alain Berthod^b, Daniel W. Armstrong^{a,*}^a Department of Chemistry and Biochemistry, University of Texas at Arlington, Planetarium Place, Arlington, TX 76019, USA^b Institut des Sciences Analytiques, CNRS, Université de Lyon 1, 5 rue de la Doua, 69100 Villeurbanne, France

ARTICLE INFO

Article history:

Received 9 June 2018

Received in revised form

28 July 2018

Accepted 6 August 2018

Available online 9 August 2018

Keywords:

Mass spectrometry detection

Chiral separation

Basic drugs

Beta-blockers

Superficially porous particle

Fully porous particle

Fast separation

Vancomycin

ABSTRACT

Current trends in chiral analysis of pharmaceutical drugs are focused on faster separations and higher separation efficiencies. Core-shell or superficially porous particles (SPP) based chiral stationary phases (CSPs) provide reduced analysis times while maintaining high column efficiencies and sensitivity. In this study, mobile phase conditions suitable for chiral analyses with electrospray ionization LC-MS were systematically investigated using vancomycin as a representative CSP. The performance of a 2.7 μm SPP based vancomycin CSP (SPP-V) 10 cm \times 0.21 cm column was compared to that of a corresponding 5 μm fully porous particles based analogue column. The results demonstrated that the SPP-V column provides higher efficiencies, 2–5 time greater sensitivity and shorter analysis time for a set of 22 basic pharmaceutical drugs. The SPP-V was successfully applied for the analysis of the degradation products of racemic citalopram whose enantiomers could be selectively identified by MS.

© 2018 Xi'an Jiaotong University. Production and hosting by Elsevier B.V. This is an open access article under the CC BY-NC-ND license (<http://creativecommons.org/licenses/by-nc-nd/4.0/>).

1. Introduction

Over the past decades, after the issuance of U.S. Food and Drug Administration (FDA) guidelines relating to the study and pharmaceutical development of individual enantiomers [1], the analysis and quantification of chiral drugs has become a necessity. This is due to the different pharmacological or toxicological effects that the two enantiomers of a chiral active pharmaceutical ingredient may have. Whereas one enantiomer can have the desired beneficial properties, the other can have none or the same or even adverse effects.

High-performance liquid chromatography (HPLC) coupled to mass spectrometry (MS) has become one of the most dominant techniques for analysis in the pharmaceutical field [2]. Hyphenation of the high-resolving power of HPLC to MS provides straightforward method development capabilities with excellent analytical linearity, sensitivity and selectivity in the enantioselective analysis of drugs throughout the drug discovery and development process [2,3]. Applying tandem mass spectrometry in HPLC-MS adds further selectivity to MS detection of drug molecules and their metabolites in complex biological matrices, which can help avoid the need for more complicated separation or extensive sample clean-up procedures [4].

In the pharmaceutical industry, current trends of enantioselective analysis of drugs are focused on separation efficiency and faster analysis time [2,5–9]. This is mainly driven by the challenges of either more complex samples or increasing numbers of samples [10]. The analytical throughput of chiral analysis is primarily dependent on the selectivity and efficiency of chiral columns. Fast chromatography approaches such as micro-column technologies with smaller particle size and monolithic silica column methods have been developed to make high-speed chiral separations possible. However, these micro-columns are often accompanied with much higher system backpressure and/or decreased chromatographic resolution and efficiency [11]. Although monolith based stationary phases can provide fast separations, there are often drawbacks such as instability and irreproducibility of the columns, and high cost of making these columns [12–15]. There has yet to be any competitive monolithic chiral stationary phases (CSPs).

The recent development of superficially porous particles (SPPs, fused-core or core-shell) based columns is generally considered a breakthrough in column technology that provides reduced analysis time while maintaining high column efficiencies with relatively low operational back pressure [16–18]. The increased efficiencies result from lower eddy dispersion, as well as other minimized band broadening effects compared to their fully porous particle (FPP) analogues [19–22]. In addition to the above mentioned advantages, SPP materials provide flatter dependence of column

Peer review under responsibility of Xi'an Jiaotong University.

* Corresponding author.

E-mail address: sec4dwa@uta.edu (D.W. Armstrong).

performance on the mobile phase flow-rate, primarily due to decreased resistance to mass-transfer compared to FPP (a smaller C-term in the van Deemter equation), hence are better suited for high-speed separations [23].

Although SPP based achiral stationary phases have been developed and have become widely used for drug analysis in recent years, chiral SPP based materials have lagged behind. Recently, several polysaccharide and glycopeptide based chiral selectors have been coated or covalently bonded to SPP silica gel for chiral separations [9,23,24]. Higher enantiomeric separation efficiency and resolution were often observed with the use of SPP based CSPs when compared to their corresponding FPP analogues [23–25]. Chiral separations done in seconds were achieved with these newly developed materials [9]. However, all the enantiomeric separation methods based on these novel SPP columns were developed with UV detection and most of them cannot be directly utilized with HPLC-MS due to various mobile phases and additive incompatibilities. Diminished or lost enantiomeric selectivity/resolution is often observed when simply changing mobile phase solvents and additives of previously developed HPLC-UV methods to achieve MS compatible conditions [25,26]. Hence, the LC-MS conditions need to be carefully optimized prior to chiral analysis.

The purposes of this study are: (1) to systematically evaluate mobile phase conditions suitable for chiral LC-MS analysis, and provide a guideline for users in the selection of mobile phase additives in chiral LC-MS, (2) to evaluate the feasibility of using SPP based CSPs for fast and efficient enantioseparation of pharmaceutical basic drugs with MS detection, and (3) to compare the enantioseparation performance between SPP and FPP based CSPs. The macrocyclic glycopeptide vancomycin chiral selector has been used in the enantiomeric separation of a variety of chiral basic drugs. The usefulness of this macrocyclic selectors results from its broad selectivity, making it an ideal candidate for chiral LC-MS analyses [26–29].

2. Experimental

2.1. Chiral drugs and chemicals

22 basic drugs including 11 β -blockers, 4 antidepressants, 4 sedative-analgesics and 3 other drugs were selected as test standards (Table 1) and provided by Millipore Sigma-Aldrich (St. Louis, MO, USA). The mobile phases were prepared from the following compounds (purities > 95%) and solvents: formic acid (FA), trifluoroacetic acid (TFA), triethylamine (TEA), ammonium formate (NH_4FA), ammonium acetate (NH_4Ac), ammonium trifluoroacetate (NH_4TFA), and triethylammonium acetate (TEAAc) were all from Sigma-Aldrich; acetic acid (AA) was from J.T. Baker (Center Valley, PA, USA); HPLC-MS grade methanol and water were from Honeywell Burdick and Jackson (Morristown, NJ, USA). Citalopram was obtained from Sigma-Aldrich and standards of its two degradation products were a gift from Lundbeck (Valby, Denmark).

2.2. Chromatography

Table 2 lists the characteristics of the chiral vancomycin stationary phases used in this work in two 10 cm \times 0.21 cm columns. The Astec-Chirobiotic V[®] column was obtained from Supelco (product 11018A-ST, Millipore-Sigma, a division of Merck KGaA, Darmstadt, Germany). The VancoShell[®] column was obtained from AZYP (product LS2002, Azyp, Arlington, Texas, USA). The columns

were mounted in a Prominence LC-20AT HPLC system (Shimadzu, Columbia, Maryland, USA) coupled to an MS-8040 triple quad mass spectrometer (Shimadzu) with an orthogonal electrospray ionization (ESI) source. Signal acquisition and data handling were performed with the LabSolutions v5 software (Shimadzu). Due to the lack of ionization with apolar normal-phase solvents, the two columns were evaluated with pure methanol mobile phases in polar ionic mode (PIM) and hydro-organic mobile phases in reversed-phase (RP) mode.

Unless otherwise indicated, the flow rate was 0.3 mL/min producing a dead time of about 40 s with the 10 cm columns with 0.21 cm internal diameter (mobile phase velocity: 0.25 cm/s). The basic drugs were dissolved in methanol in stock solutions at 1 mg/mL, and stored at 5 °C. The injection loop had a 2 μL volume. All experiments were done at room temperature.

2.3. Forced decomposition study of citalopram

The antidepressant citalopram was subjected to a 2-day hydrolytic degradation. A 10 mg solution of citalopram in 100 mL 0.2 M NaOH (pH 13.3) was heated at 80 °C for 48 h, and 10 mL solution portions were taken at time 12 h and 48 h and neutralized with a drop of acetic acid. The hydrolytic degradation products were extracted by adding 10 mL dichloromethane and vigorously shaking the biphasic mixture. The separated lower organic layer was dried with argon and reconstituted in methanol prior to LC-MS analysis.

3. Results and discussion

3.1. Mobile phase and mass spectrometry detection

3.1.1. Flow rate effect

A UV detector is a non-destructive concentration sensitive detector, while the MS detector is a mass sensitive destructive detector. The difference between the two types of detector can be put simply: if the mobile phase flow rate is stopped when a solute is in the detector, the concentration sensitive UV signal will stay constant; the mass sensitive MS signal will drop to zero as soon as the ion input ceases. The critical consequence is a strong difference in signal intensity that depends on the mobile phase flow rate with the MS detector and not with the UV detector. This signal intensity difference makes the integrated surface area obtained with the UV concentration sensitive detector inversely proportional to the mobile phase flow rate. This surface would not be sensitive to flow rate with the MS mass sensitive detector if the ESI efficiency was not flow rate dependent. Unfortunately, ESI becomes less efficient when there are more or bigger droplets to ionize and this effect also makes the experimental MS surface area decrease when the flow rate increases [30]. With the MS instrument in this study, a flow rate of 0.3 mL/min provided the optimal compromise between chromatographic separation duration and ESI signal intensity and it was used for all mobile phase composition testings.

3.1.2. Mobile phase composition effect

Ions must be produced by the ESI source. The mobile phase chemical composition greatly affects ionization. A systematic investigation is difficult since changing the mobile phase composition also affects the chromatographic separation modifying retention time, peak efficiencies and chromatographic resolution. Table 3 gathers the observed effects of mobile phase composition on ESI-MS detection.

Table 1
Names, structures, properties and best separation conditions of the studied basic drugs^a.

Name/therap. class	Structure	M.W.	Log P _{oct} /Log P _{cation}	pK _a	k'	α	Rs	N Plates	Optimal LC-MS mobile phase ¹
Acebutolol <i>β</i> -blocker		336.2	1.53 –1.7	9.57	3.0 6.4	1.2 1.2	1.3 1.2	1900 1200	PIM
Alprenolol <i>β</i> -blocker		249.2	2.69 –0.55	9.67	2.9 7.0	1.1 1.1	1.1 1.0	3900 2800	PIM
Atenolol <i>β</i> -blocker		266.2	0.43 –2.8	9.67	2.2 4.0	1.2 1.1	1.3 1.2	3600 2900	PIM
Carvedilol <i>β</i> -blocker		406.2	3.42 0.18	8.74	4.1 8.8	1.1 1.1	1.1 1.0	3000 2300	PIM
Esmolol <i>β</i> -blocker		295.2	1.82 –1.42	9.67	2.4 6.1	1.05 1.05	0.9 0.8	5000 3400	PIM
Labetalol ² <i>β</i> -blocker		328.4	2.31 –0.27	9.3	6.1/ 9.6/ 10.7/ 16.7	1.1/ 1.4/ 1.1/ 1.4	0.9/ 3.1/ 0.8/ 2.5	3600/ 1900/ 2800/ 1100	PIM
Metoprolol <i>β</i> -blocker		267.2	1.76 –1.48	9.67	2.4 3.6	1.1 1.1	1.1 1.0	6000 3600	PIM
Pindolol <i>β</i> -blocker		233.1	1.69 –1.55	9.66	1.3 2.5	1.1 1.1	1.4 1.4	5500 3400	PIM
Propranolol <i>β</i> -blocker		259.2	2.58 –0.66	9.67	7.9 16.1	1.2 1.2	2.4 1.4	3500 1200	PIM
Salbutamol <i>β</i> -blocker		239.2	0.34 –2.36	9.60	1.85 3.15	1.1 1.1	1.3 1.2	5000 3200	PIM

Table 1 (continued)

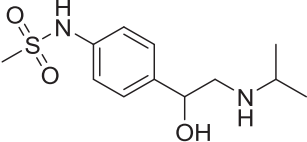
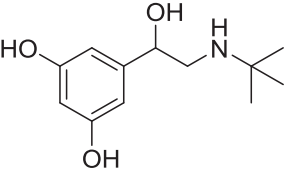
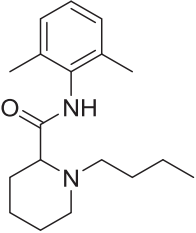
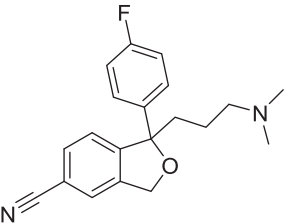
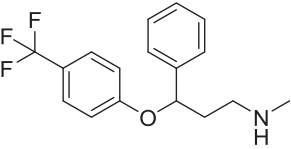
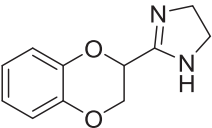
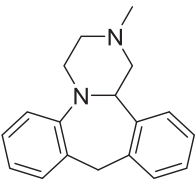
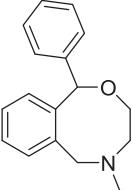
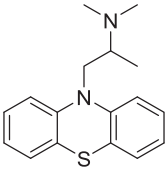
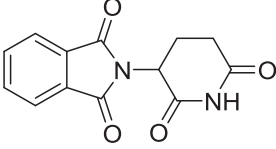
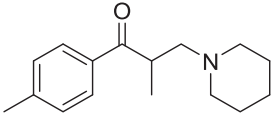
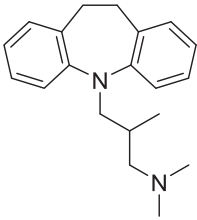
Name/therap. class	Structure	M.W.	Log P_{oct} / Log P_{cation}	pK_a	k'	α	R_s	N Plates	Optimal LC-MS mobile phase ¹
Sotalol <i>β-blocker</i>		272.1	-0.40 -3.2	9.65	1.7 2.9	1.2 1.2	1.6 1.5	4100 2500	PIM
Terbutaline <i>β-adrenergic agonist</i>		225.1	0.46 -1.90	8.86	3.9 11.1	1.1 1.1	1.4 1.2	5000 3000	PIM
Bupivacaine <i>Anesthetic</i>		288.2	4.52 1.0	8.0	0.9 2.0	1.2 1.3	1.4 1.5	3800 1300	RP
Citalopram <i>Antidepressant</i>		324.2	3.76 0.26	9.78	17.1 28.3	1.1 1.1	1.3 1.1	3400 2400	RP
Fluoxetine <i>Antidepressant</i>		309.1	4.17 0.93	9.80	10.7 21.9	1.3 1.2	5.0 3.1	5800 3900	RP
Idazoxan <i>α-blocker</i>		204.1	0.77 -1.65	8.62	2.9 6.4	1.1 1.1	1.6 1.4	5900 3500	RP
Mianserin <i>Antidepressant</i>		264.2	3.83 0.33	6.92	0.9 1.9	2.5 2.2	7.0 5.9	3000 1900	RP
Nefopam <i>Analgesic</i>		253.2	3.40 1.80	7.92	2.9 7.9	1.2 1.1	1.5 1.1	2000 2700	RP

Table 1 (continued)

Name/therap. class	Structure	M.W.	Log P _{oct} /Log P _{cation}	pK _a	k'	α	Rs	N Plates	Optimal LC-MS mobile phase ¹
Promethazine Sedative		284.1	4.29 0.79	9.05	3.4 6.7	1.8 1.6	6.6 5.3	3100 2500	RP
Thalidomide Sedative		258.1	0.01 non ionizable	11.6	1.3 3.3	2.2 2.0	4.4 3.2	1200 1000	RP
Tolperisone Muscle relaxant		245.2	3.57 0.07	8.78	3.0 8.6	1.2 1.2	1.7 1.5	2500 1300	RP
Trimipramine Antidepressant		294.2	4.76 3.40	9.40	3.3 6.6	1.3 1.2	3.1 1.4	3600 1300	RP

1-PIM: polar ionic mode (2.0 mM TEAAc in methanol); RP: reversed phase with 90% methanol/10% 5 mM NH₄Ac buffer pH 4.1; flow rate 0.3 mL/min.

2-The compound Labetalol has two chiral centers, hence four enantiomers.

^a The first line of values: SPP column VancoShell, 10 cm × 0.21 cm, 2.7 μm particles. The second line of values: FPP column Chirobiotic V, 10 cm × 0.21 cm, 5 μm particles; Log P_{oct} is the octanol/water partition coefficient of the drug in molecular form; Log P_{cation} is for the cationic form calculated values (ChemAxon and Molinspiration softwares); k', α, and Rs are respectively the experimental retention, enantioselectivity, and resolution factors with 5%–10% RSD; N is the efficiency taken on the first eluting enantiomer in theoretical plates (50% RSD).

The apolar mobile phases used in the normal phase mode do not solubilize ions. Also they preclude efficient molecule ionization; hence this mode is inappropriate with MS detection. The PIM uses non-aqueous polar mobile phases in which small amounts (0.05%–0.5%) of amine and organic acid are added to modify the ionization state of both the solutes and the stationary phase. Pure methanol was used as the PIM solvent with different added acids, bases or salts. Table 3 shows that good ionization was obtained with ammonium salts, either formate, acetate or trifluoroacetate. The best signal was obtained with 0.5–1 mM TEA acetate. However, this salt has a trade-off since higher than 1 mM concentration produced faster separation (lower retention times), but it also degraded MS sensitivity due to ionization suppression. The in-situ formation of TEA acetate by adding proportion of TEA and AA to methanol gave similar results with ionization suppression observed when more than 0.02% (v/v) was added. 0.02% TEA corresponds to 1.44 mM and 0.02% AA is 3.5 mM, the combination of which makes 1.44 mM TEAAc with an excess of about 2 mM AA. Pure acids induce solute MS ionization, but they are not recommended for chromatographic reasons: the protonated basic drugs of our set were eluted at the dead volume not giving any separation, since they were electrostatically repelled from the positively charged stationary phase.

The polar aqueous reversed phase mobile phases were appropriate for MS detection. The best salt additive was ammonium

acetate in our working conditions with methanol:water (90:10, v/v). TEAAc, NH₄FA and NH₄TFA also could be used giving poorer peak shapes but with an acceptable signal. Concentrations of TEAAc higher than 0.5 mM and addition of TEA and AA higher than 0.05% (v/v) produced significant ionization suppression. Since higher salt concentrations provided faster separations, the optimum reversed phase composition was methanol/water (90:10, v/v) with 5 mM NH₄Ac (Table 3).

3.2. Enantiomer separation with fully porous and superficially porous particles

Table 1 lists the retention, selectivity and resolution factors obtained with the basic drugs and the two chiral columns containing the same macrocyclic glycopeptide vancomycin selector. For each compound, the first line corresponds to the data obtained with the VancoShell[®] SPP column and the second line gives the Chirobiotic[®] V FPP column data, all obtained with the same column geometry, mobile phase composition and flow rate. The detection was done by MS for both columns. The PIM mobile phase composition: pure methanol with 2 mM TEAAc, provided optimal separations in term of solute retention, resolution and signal for all β-blocker solutes. The other basic drugs were best separated by the reversed mobile phase made of methanol:water (90:10, v/v) with 5 mM NH₄Ac, both flown at 0.3 mL/min.

Table 2
Characteristics of the chiral vancomycin columns.

Column trade name	Manufacturer	Length (cm)	Internal diameter (mm)	Silica particles						Selector loading ($\mu\text{mol}/\text{column}$)
				Diameter (μm)	Porosity	Pore (nm)	Surface (m^2/g)	Carbon loading (%)	Bonding ($\mu\text{mol}/\text{m}^2$)	
Chirobiotic V	Supelco Millipore-Sigma	10	2.1	5	FPP 100%	10	300	13.5	0.75	72
VancoShell	AZYP	10	2.1	2.7	SPP 75%	12	120	7.2	0.87	33

The core-shell particles have a solid spherical core of $1.7 \mu\text{m}$ diameter and $2.57 \mu\text{m}^3$ volume and a $0.5 \mu\text{m}$ thick porous layer making a volume of $7.74 \mu\text{m}^3$ or 75% of the whole $2.7 \mu\text{m}$ particle volume of $10.3 \mu\text{m}^3$.

The first general observation is that the Chirobiotic[®] V FPP column systematically produced longer retention times, seen in almost always 50% higher retention factors, k' , than the VancoShell[®] SPP column for the same solute, mobile phase and flow rate. The second observation is that the enantioselectivity factors obtained with the two columns are very similar. The last general observation is that the peak efficiency obtained with the SPP column is always higher than that observed with the FPP column of equal length.

Pointing that the chiral selector is the same for the two columns, the results can be explained as follows: (i) the difference in retention is due to the fact that the FPP column contains twice more vancomycin selector than the SPP column ($72 \mu\text{moles}$ versus $33 \mu\text{moles}$, Table 2); (ii) this larger amount of selector increases equally the retention of both enantiomers, so the ratio of the two increased retention factors, which is the enantioselectivity factor, stays constant; and (iii) the peak efficiency in column of equal length is linked to the silica particle diameter which is almost twice smaller ($2.7 \mu\text{m}$) in the SPP column compared to the FPP one ($5 \mu\text{m}$, Table 2). It must be noted that the listed peak efficiencies

are not obtained at the same retention time so the difference between columns may be even higher. Further, the greater extra-column volume, associated with MS detection, limits the efficiency gains of the SPP column somewhat [9,19,24,25].

The resolution factor combines retention, selectivity and efficiency in a single quality parameter. The R_s factors obtained with the VancoShell[®] SPP column are clearly significantly better than their corresponding values obtained with the Chirobiotic[®] FPP column (Table 1). The advantage of the SPP particles is obvious that faster separations are obtained with better resolution factors. Not surprisingly, these results are fully coherent with previously published works done with the vancomycin chiral selector [6,9,31].

3.3. Sensitivity comparison

The most used chromatographic detector is the UV–vis detector for its versatility, ease of use and cost. It is sensitive down to the nanogram on five orders of magnitude linear range, up to almost a milligram injected. With optimized ionization, the MS detector is known to be almost three orders of magnitude more sensitive than

Table 3
Mobile phase compositions and MS detection with electrospray ionization.

Solvents	Buffer/salts	Status	Comments
Normal phase mode			
Heptane/ propanol	Not soluble	Not MS compatible	Apolar mobile phases cannot handle ions
Polar ionic mode			
100% methanol	Formic acid Acetic acid Trifluoroacetic acid	Good ionization	Useless with basic drugs whose protonated forms are not retained
100% methanol	TEAAC	Excellent ionization at 0.5–1 mM – suppression is observed at higher concentrations	Higher salt concentrations reduce solute retention times
100% methanol	TEA/AA	Excellent ionization with 0.02% (v/v) or less – suppression is observed with higher % v/v	At equal TEA and AA %v/v there are 2.4 AA mol per TEA mol.
100% methanol	NH ₄ TFA	Good ionization	Higher salt concentrations reduce retention times
100% methanol	NH ₄ FA	Good ionization	Higher salt concentrations reduce retention times
100% methanol	NH ₄ Ac	Acceptable ionization	Higher salt concentrations reduce retention times
Reversed phase			
90% methanol / 10% aqueous buffer	Formic acid Acetic acid Trifluoroacetic acid	Good ionization	Useless with basic drugs whose protonated forms are not retained
90% methanol/ 10% aqueous buffer	TEAAC	Significant ionization suppression above 0.5 mM	Long retention of the analytes at low salt concentration
90% methanol/ 10% aqueous buffer	TEA/AA	Significant ionization suppression above 0.05% (v/v)	Long retention of the analytes
90% methanol/ 10% aqueous buffer	NH ₄ TFA	Acceptable ionization	Mediocre additive for chiral recognition
90% methanol/ 10% aqueous buffer	NH ₄ FA	Good ionization	Good peak shapes
90% methanol/ 10% aqueous buffer	NH ₄ Ac	Best RP additive	Good peak shape and solute retention

Orthogonal ESI source of a Shimadzu LC-MS 8040 triple quad MS; positive ion monitoring, ionization voltage: 4.5 kV; desolvation line at 250 °C; heating block at 500 °C; 2 mL/min N₂ nebulizing gas; 15 L/min N₂ drying gas. TEA: triethylamine; AA: acetic acid; Ac: acetate; FA: formic acid; TFA: trifluoroacetic acid.

Table 4
Comparison of detection limits (LOD) between the VancoShell SPP and Chirobiotic V FPP columns for the selected basic drugs^a.

Compound ^b	Monitored <i>m/z</i>	LOD (inj. pg) ^c		Improvement factor ^d
		Chirobiotic V FPP	VancoShell SPP	
Acebutolol	337.2	1.8	0.4	4.5
Alprenolol	250.2	0.9	0.2	4.5
Atenolol	267.2	2.0	0.8	2.5
Esmolol	296.2	1.4	0.4	3.6
Metoprolol	268.2	0.7	0.2	3.7
Oxprenolol	266.3	0.9	0.2	4.3
Pindolol	234.1	2.0	0.8	2.5
Propranolol	260.2	1.3	0.4	3.3
Salbutamol	240.2	1.0	0.4	2.4
Sotalol	273.1	6.0	3.0	2.0
Terbutaline	226.1	1.3	0.4	3.3
Bupivacaine	289.2	0.2	0.1	1.7
Citalopram	325.2	5.0	1.4	3.6
Fluoxetine	310.1	3.3	1.2	2.8
Idazoxan	205.1	6.0	1.4	4.3
Mianserin	265.2	0.1	0.04	2.5
Nefopam	254.2	0.5	0.2	2.7
Promethazine	285.1	7.5	3.0	2.5
Thalidomide	259.1	5.0	1.2	4.2
Tolperisone	246.2	6.0	2.0	3.0
Trimipramine	294.2	1.3	0.6	2.2

^a Chromatographic condition: RP with methanol:5 mM NH₄Ac buffer solution (90:10, v/v); flow rate: 0.3 mL/min.

^b All these basic drugs studied were first separated with the chromatographic conditions mentioned in Table 1, and were then detected in positive SIM mode at the *m/z* indicated.

^c The reported LODs are absolute values in picograms injected for the first eluted enantiomer.

^d calculated comparing the LOD values of Chirobiotic V FPP to those obtained with VancoShell SPP.

the UV detector [32]. So the MS detector is not compared to the UV detector in term of sensitivity. The limit of detection (LOD) that can be reached with both SPP and FPP columns in similar conditions were compared.

The LODs in LC-MS were obtained by serial dilution of the standard solution of each compound until a signal-to-noise ratio (S/N) of three was noted in five replicate injections of the diluted sample. The LOD determinations were performed with the column in the positive SIM mode monitoring the *m/z* of the protonated analyte. Table 4 summarizes the detection limits for all these tested drugs after column separation using both the VancoShell SPP and the Chirobiotic V FPP columns under identical mobile phase and *m/z* SIM MS conditions. As can be seen in Table 4, a LOD as low as 40 fg (0.04 pg in absolute values i.e. 2 µL of a 20 ng/L dilution injected) was obtained for the mianserin drug with the VancoShell SPP column. This lowest LOD was 2.5 lower than that obtained with the Chirobiotic V FPP column for the same compound. The LODs with the VancoShell SPP column were all down to the picogram injected and 2–5 times lower than the corresponding LODs obtained with the Chirobiotic V FPP column in the same MS conditions.

3.4. Fast SPP separations

The SPP core-shell particles were developed for reducing separation duration and especially solvent consumption [6,9]. As seen in Table 1, in optimal enantioselective conditions at 0.3 mL/min, the VancoShell SPP column separates the listed enantiomers two to four times faster than the Chirobiotic V FPP column with a better resolution. Since fast chiral separations are needed in two-dimensional chromatography, the MS response was tested in separations done in seconds. Fig. 1 shows the separation of three drugs achieved in less than a minute. To obtain such fast separations some

compromises had to be made. The faster flow rate produced a lower ESI response compensated by injecting 20 pg of solute. Also the PIM mobile phase was selected because it gave lower drug retentions; however, the resolution factors also were significantly lower. The promethazine resolution factor dropped from 6.6 with optimized RP mobile phase (Table 1) to 1.4 with the fast PIM mobile phase (Fig. 1) mainly due to the great drop in efficiency (from 3100 plates to 400 plates) with broadening peaks at this fast flow rate. However, even in these conditions, the ESI signal is perfectly usable and ESI-MS detection could be used in a fast second dimension in 2D-LC with baseline separation of the enantiomers [33].

3.5. Application: following citalopram basic degradation

The characterization of all possible impurities and degradation products in a drug substance and product is required by regulatory agencies [30]. Since many drugs are chiral, the advantage of using CSPs for the degradation studies is that not only degradation products but also each enantiomer of the degraded drug products can be identified and quantified. The MS detection adds the information on the nature of the degradation products providing their mass to charge ratio.

A forced degradation study was done using the racemic form of the antidepressant drug citalopram as a representative. Two major peaks (*m/z* 343 and 344) were found in the positive triple-quadrupole-scan mode with direct injection of 2 µL of the processed sample. The degraded sample was further separated on the SPP-V column and was detected in positive Q3-SIM mode. The peaks were compared to the citalopram standard. As shown in Fig. 2, the citalopram standard peaks that appear in the retention window of 12–15 min progressively decrease and eventually disappear, indicating the complete degradation of citalopram in less than two days at 80 °C, pH 13. The extracted ion chromatograms (EIC) in SIM mode at

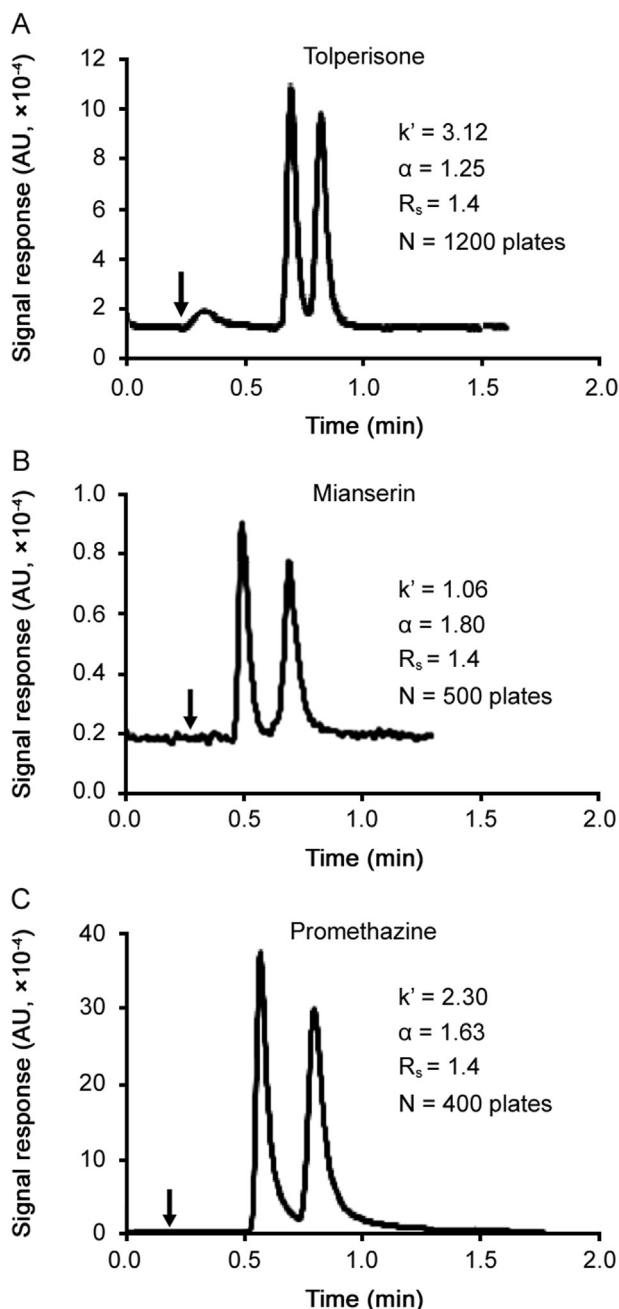


Fig. 1. Fast separations of basic drugs using the VancoShell SPP column. Chromatographic conditions: PIM mobile phase: methanol with 2 mM TEAAc; flow rate: (A) 1.0 mL/min for tolperisone, (B) 0.8 mL/min for mianserin, (C) 1.2 mL/min for promethazine; injection volume: 2 μ L of 10 ng/mL. MS detection in positive SIM mode; monitored m/z : tolperisone 246.2, mianserin 265.2 and promethazine 285.1. The vertical arrows point at the dead time.

m/z 343 and 344 showed two chiral degradation products. One enantiomeric pair appears at the retention window: 3.0–4.5 min and the other pair eluting between 18 and 21 min. After checking for possible structures corresponding to the m/z ratios and determining the retention times of the provided degradation product standards (Fig. 2), the structure of Product 1 was confirmed to be the amide obtained by hydrolysis of the citalopram nitrile group:

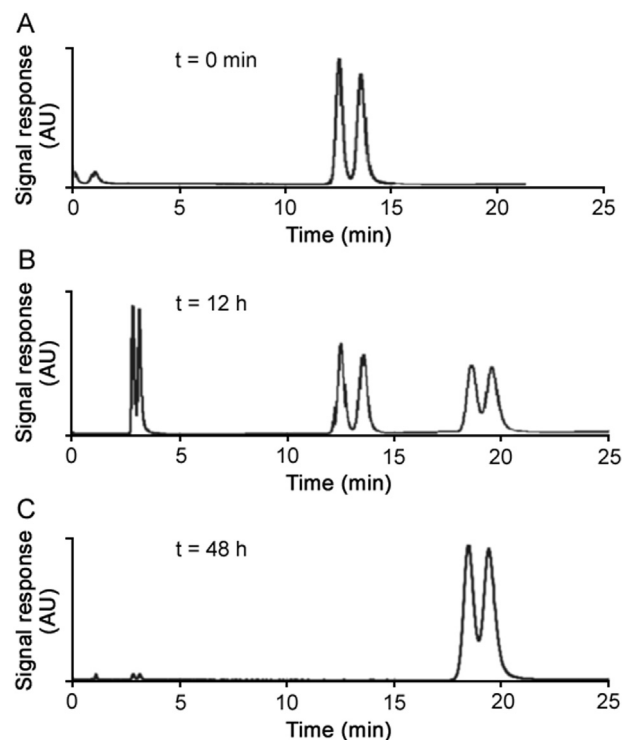
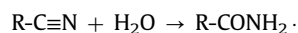


Fig. 2. Following the achiral basic degradation of citalopram in aqueous pH 13 solution at 80 °C. Chromatographic conditions: column VancoShell 10 cm \times 0.21 cm, 2.7 μ m core shell particles; RP mobile phase, methanol/buffer 5 mM NH_4Ac (10:90, v/v); flow rate, 0.3 mL/min; injection volume, 2 μ L. MS conditions: (A) TIC in positive Q3-scan mode, (B) and (C) positive Q3 SIM mode at m/z 343.2 from 0 to 5 min (amide), 325.2 from 5 to 15 min (nitrile), and 344.2 from 15 to 25 min (acid derivative).

This amide was itself hydrolyzed in the corresponding acid Product II following $\text{R-CONH}_2 \rightarrow \text{R-COOH}$. The confirmed structures of degradation Products I and II were consistent with previously reported results in the literature [34,35].

4. Conclusions

An MS detector is suitable to detect separated enantiomers in the polar ionic mode with methanol and appropriate salt mobile phases, and in the reversed phase mode with an aqueous buffer mobile phase rich in organic modifier. Volatile salts must be used to buffer the mobile phase or to adjust the stationary phase ionization for best enantiorecognition. Amounts of triethylamine and acetic acid smaller than 0.05% (v/v) were optimal, allowing to adjust the acidity/basicity by adapting the TEA and AA proportions. Larger amounts of salts produced ESI ionization suppression. Ammonium acetate was the best salt additive in the RP mode when higher than 1 mM concentration was needed for peak shape or lower retention of the basic drugs tested.

The advantages of using a column containing superficially porous particles are faster separations using significantly less mobile phase associated with better efficiencies giving similar or better resolution. These advantages were confirmed by comparing an SPP column to a fully porous column of identical geometry and both containing the same vancomycin chiral selector. In optimized conditions the LODs obtained with the SPP column were between two and five times lower than those obtained with the FPP column. However, higher mobile phase flow rates are associated with

a lower ionization yield due to an increased number of larger droplets in the ESI source, suggesting that separations of enantiomers done in seconds will be detected by the MS with lower performance (LOD) than those obtained in optimal (slower) conditions.

Conflicts of interest

The authors declare that there are no conflicts of interest.

Acknowledgments

We thank AZYP, LLC, for their technical support for HPLC chiral column technology, and Shimadzu Institute Center for Nanostructured Materials for providing support for all mass spectrometry experiments. This work was supported by the Robert A. Welch Foundation (Y0026) and the French National Center for Scientific Research (ISA-CNRS-UMR5280).

References

- [1] Anonymous, FDA'S. Policy Statement Dev. New Stereo. Drugs Chirality 4 (1992) 338–340.
- [2] Y. Nie, X. Liu, X. Yang, et al., Review: recent application of chiral liquid chromatography–tandem mass spectrometric methods for enantiomeric pharmaceutical and biomedical determinations, *J. Chromatogr. Sci.* 51 (2013) 753–763.
- [3] N.M. Maier, P. Franco, W. Lindner, Separation of enantiomers: needs, challenges, perspectives, *J. Chromatogr. A* 906 (2001) 3–33.
- [4] G.L. Erny, A. Cifuentes, Liquid separation techniques coupled with mass spectrometry for chiral analysis of pharmaceuticals compounds and their metabolites in biological fluids, *J. Pharm. Biomed. Anal.* 40 (2006) 509–515.
- [5] J. Chen, W.A. Korfmacher, Y. Hsieh, Chiral liquid chromatography–tandem mass spectrometric methods for stereoisomeric pharmaceutical determinations, *J. Chromatogr. B* 820 (2005) 1–8.
- [6] C.L. Barhate, Z.S. Breitbach, E.C. Pinto, et al., Ultrafast separation of fluorinated and desfluorinated pharmaceuticals using highly efficient and selective chiral selectors bonded to superficially porous particles, *J. Chromatogr. A* 1426 (2015) 241–247.
- [7] K. Zawatzky, M. Biba, E.L. Regalado, et al., MISER chiral supercritical fluid chromatography for high throughput analysis of enantiopurity, *J. Chromatogr. A* 1429 (2016) 374–379.
- [8] M. Biba, E.L. Regalado, N. Wu, et al., Effect of particle size on the speed and resolution of chiral separations using supercritical fluid chromatography, *J. Chromatogr. A* 1363 (2014) 250–256.
- [9] D.C. Patel, Z.S. Breitbach, M.F. Wahab, et al., Gone in seconds: praxis, performance, and peculiarities of ultrafast chiral liquid chromatography with superficially porous particles, *Anal. Chem.* 87 (2015) 9137–9148.
- [10] S. Fekete, E. Oláh, J. Fekete, Fast liquid chromatography: the domination of core–shell and very fine particles, *J. Chromatogr. A* 1228 (2012) 57–71.
- [11] Y. Hsieh, W.A. Korfmacher, Increasing speed and throughput when using HPLC–MS/MS systems for drug metabolism and pharmacokinetic screening, *Curr. Drug Metab.* 7 (2006) 479–489.
- [12] B. Chankvetadze, C. Yamamoto, Y. Okamoto, Very fast enantioseparations in HPLC using cellulose tris(3,5-dimethylphenylcarbamate) coated on monolithic silica support, *Chem. Lett.* 32 (2003) 850–851.
- [13] B. Chankvetadze, Monolithic chiral stationary phases for liquid-phase enantioseparation techniques, *J. Sep. Sci.* 33 (2010) 305–314.
- [14] R. Hayes, A. Ahmed, T. Edge, et al., Core-shell particles: preparation, fundamentals and applications in high performance liquid chromatography, *J. Chromatogr. A* 1357 (2014) 36–52.
- [15] C. Karlsson, L. Karlsson, D.W. Armstrong, Evaluation of vancomycin chiral stationary phase in capillary electrochromatography using polar organic and reversed-phase modes, *Anal. Chem.* 72 (2000) 4394–4401.
- [16] J.M. Cunliffe, T.D. Maloney, Fused-core particle technology as an alternative to sub-2- μm particles to achieve high separation efficiency with low back-pressure, *J. Sep. Sci.* 30 (2007) 3104–3109.
- [17] K.K. Unger, R. Skudas, M.M. Schulte, Particle packed columns and monolithic columns in high-performance liquid chromatography–comparison and critical appraisal, *J. Chromatogr. A* 1184 (2008) 393–415.
- [18] S. Fekete, J. Fekete, Fast gradient screening of pharmaceuticals with 5 cm long, narrow bore reversed-phase columns packed with sub-3 μm core–shell and sub-2 μm totally porous particles, *Talanta* 84 (2011) 416–423.
- [19] D. Cabooter, A. Fanigliulo, G. Bellazzi, et al., Relationship between the particle size distribution of commercial fully porous and superficially porous high-performance liquid chromatography column packings and their chromatographic performance, *J. Chromatogr. A* 1217 (2010) 7074–7081.
- [20] A.S. Breitbach, Y. Lim, Q.-L. Xu, et al., Enantiomeric separations of α -aryl ketones with cyclofructan chiral stationary phases via HPLC and supercritical fluid chromatography, *J. Chromatogr. A* 1427 (2016) 45–54.
- [21] F. Griitti, G. Guiochon, Possible resolution gain in enantioseparations afforded by core–shell particle technology, *J. Chromatogr. A* 1348 (2014) 87–96.
- [22] F. Griitti, T. Farkas, J. Heng, et al., On the relationship between band broadening and the particle-size distribution of the packing material in liquid chromatography: theory and practice, *J. Chromatogr. A* 1218 (2011) 8209–8221.
- [23] K. Lomsadze, G. Jibuti, T. Farkas, et al., Comparative high-performance liquid chromatography enantioseparations on polysaccharide based chiral stationary phases prepared by coating totally porous and core–shell silica particles, *J. Chromatogr. A* 1234 (2012) 50–55.
- [24] D.A. Spudeit, M.D. Dolzan, Z.S. Breitbach, et al., Superficially porous particles vs. fully porous particles for bonded high performance liquid chromatographic chiral stationary phases: isopropyl cyclofructan 6, *J. Chromatogr. A* 1363 (2014) 89–95.
- [25] Q. Kharashvili, G. Jibuti, T. Farkas, et al., Further proof to the utility of polysaccharide-based chiral selectors in combination with superficially porous silica particles as effective chiral stationary phases for separation of enantiomers in HPLC, *J. Chromatogr. A* 1467 (2016) 163–168.
- [26] M.J. Desai, D.W. Armstrong, Transforming chiral liquid chromatography methodologies into more sensitive liquid chromatography–electrospray ionization mass spectrometry without losing enantioselectivity, *J. Chromatogr. A* 1035 (2004) 203–210.
- [27] D.W. Armstrong, Y. Tang, S. Chen, et al., Macrocyclic antibiotics as a new class of chiral selectors for liquid chromatography, *Anal. Chem.* 66 (1994) 1473–1484.
- [28] K.H. Ekbord-Ott, J.P. Kullman, X. Wang, et al., Evaluation of macrocyclic antibiotic as a new chiral selector for HPLC, *Chirality* 10 (1998) 627–660.
- [29] C.L. Barhate, D.A. Lopez, A.A. Makarov, et al., Macrocyclic glycopeptide chiral selector bonded to core-shell particles enables enantiopurity analysis of the entire *verbecestat* synthetic route, *J. Chromatogr. A* 1539 (2018) 87–92.
- [30] J.S. Page, R.T. Kelly, K. Tang, et al., Ionization and transmission efficiency in ESI-MS interface, *J. Am. Soc. Mass Spectrom.* 18 (2007) 1582–1590.
- [31] G. Hellinghausen, D. Roy, J.T. Lee, et al., Effective methodology for enantiomeric separations of 150 pharmacology and toxicology related 1°, 2°, and 3° amines with core-shell chiral stationary phases, *J. Pharm. Biomed. Anal.* 155 (2018) 70–81.
- [32] N. Barbarin, J.D. Hennion, Y. Wu, Comparison between LC–UV and LC–MS detection for the characterization of impurities and/or degradants present in trimethoprim tablets, *J. Chromatogr. A* 970 (2002) 141–154.
- [33] C.L. Barhate, E.L. Regalado, N.D. Contrella, et al., Ultrafast chiral chromatography as the second dimension in 2D-liquid chromatography experiments, *Anal. Chem.* 89 (2017) 3545–3553.
- [34] M. Sharma, P.R. Jawa, R.S. Gill, et al., Citalopram Hydrobromide: degradation product characterization and a validated stability-indicating LC–UV method, *J. Braz. Chem. Soc.* 22 (2011) 836–848.
- [35] R.N. Rao, A.N. Raju, R. Narsimha, Isolation and characterization of degradation products of citalopram and process-related impurities using RP–HPLC, *J. Sep. Sci.* 31 (2008) 1729–1738.



Original Research Article

Simultaneous determination of indapamide, perindopril and perindoprilat in human plasma or whole blood by UPLC-MS/MS and its pharmacokinetic application

Yi Tao^a, Sheng Wang^a, Lei Wang^b, Min Song^a, Taijun Hang^{a,*}^a Department of Pharmaceutical Analysis, China Pharmaceutical University, Nanjing 210009, China^b Jiangsu Jiayi Pharmaceutical Co., Ltd., Nanjing 210000, China

ARTICLE INFO

Article history:

Received 9 February 2018

Received in revised form

17 May 2018

Accepted 18 May 2018

Available online 19 May 2018

Keywords:

Indapamide

Perindopril

Perindoprilat

Pharmacokinetics

LC-MS/MS

ABSTRACT

Simple and sensitive methods were developed for the determination of indapamide, perindopril and its active metabolite perindoprilat in human plasma or whole blood by hyphenated ultra-performance liquid chromatography-mass spectrometry (UPLC-MS/MS). Indapamide-d₃, perindopril-d₄ and perindoprilat-d₄ were used as the internal standards. The separation was performed on a Thermo BDS Hypersil C₁₈ column (4.6 mm × 100 mm, 2.4 μm) for indapamide and perindopril simultaneously following a protein precipitation pretreatment of the biosamples. The separation of perindoprilat was achieved independently on a phenomenex PFP column (4.6 mm × 150 mm, 5 μm). All the analytes were quantitated with positive electrospray ionization and multiple reactions monitoring mode. The assay exhibited a linear range of 1–250 ng/mL for indapamide, 0.4–100 ng/mL for perindopril and 0.2–20 ng/mL for perindoprilat. The methods were fully validated to meet the requirements for bioassay in accuracy, precision, recovery, reproducibility, stabilities and matrix effects, and successfully applied to the pharmacokinetic study of perindopril tert-butylamine/indapamide compound tablets in Chinese healthy volunteers and the comparative pharmacokinetic study between plasma and whole blood.

© 2018 Xi'an Jiaotong University. Production and hosting by Elsevier B.V. This is an open access article under the CC BY-NC-ND license (<http://creativecommons.org/licenses/by-nc-nd/4.0/>).

1. Introduction

Perindopril (Fig. 1), a non-sulphydryl angiotensin-converting enzyme inhibitor (ACEI), is prescribed for the treatment of hypertension and heart failure. It is hydrolysed to the active metabolite perindoprilat (Fig. 1) in vivo, which can selectively inhibit the activity of angiotensin-converting enzyme (ACE) and reduce the level of angiotensin II [1,2]. Indapamide (Fig. 1) is a thiazide-type diuretic commonly used to treat mild to moderate hypertension by diuretic effect and calcium antagonist activity. As an antihypertensive drug proved to produce a significant and sustained reduction in blood pressure, indapamide works on sodium and chloride excretion and it has been reported to reduce the vascular reactivity to pressor amines [3–5].

The combination of perindopril and indapamide is suggested as one of the antihypertensive combinations of priority use by the last update of European Hypertension Guidelines [5,6]. Due to their synergistic mechanisms of actions, this combination has shown a higher antihypertensive effect with fewer side effects [7,8]. Usually perindopril tert-butylamine/indapamide is

administered in the form of tablets containing 2/0.625, 4/1.25 or 8/2.5 mg of the active pharmaceutical ingredients.

Several LC-MS/MS methods have been reported for the pharmacokinetic studies on perindopril and perindoprilat or indapamide individually in biological samples [9–14]. However, only a few pharmacokinetic studies on perindopril tert-butylamine/indapamide compound tablets have been reported [15,16]. And until now, there have not been any reports for comparative pharmacokinetic studies between plasma and whole blood. This paper describes a sensitive and reproducible LC-MS/MS method for the simultaneous determination of indapamide and perindopril in both human plasma and whole blood and an independent method for perindoprilat. The methods have been fully validated and applied to the pharmacokinetic study of perindopril tert-butylamine/indapamide compound tablets in Chinese healthy volunteers and the comparative pharmacokinetic study between plasma and whole blood.

2. Experimental

2.1. Chemicals and reagents

The reference standards of indapamide (99.5%), perindopril tert-butylamine (99.2%) and perindoprilat (99.2%) were obtained

Peer review under responsibility of Xi'an Jiaotong University.

* Corresponding author.

E-mail address: hangtj@cpu.edu.cn (T. Hang).

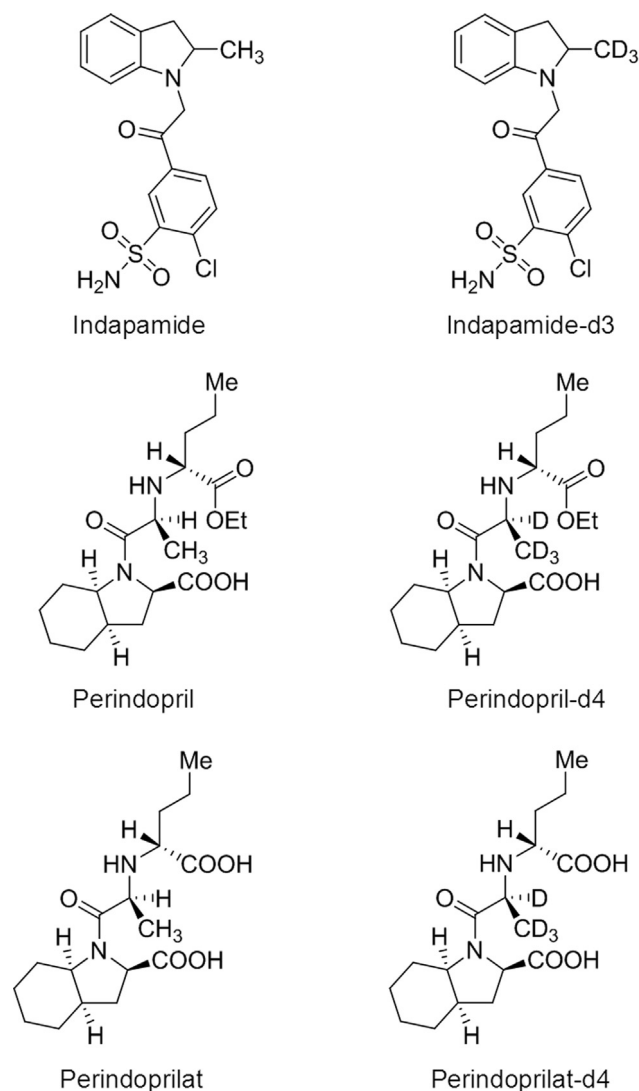


Fig. 1. Chemical structures of indapamide, perindopril, perindoprilat, indapamide-d3 (IS), perindopril-d4 (IS) and perindoprilat-d4 (IS).

from National Institutes for Food and Drug Control (Beijing, China). Indapamide-d3 (97%), perindopril-d4 (98%) and perindoprilat-d4 (98%) reference standards employed as the internal standards (ISs) for the bioassays were obtained from Toronto Research Chemicals (North York, Canada). Chemical structures of these compounds are presented in Fig. 1. Perindopril tert-butylamine/indapamide compound tablets (Batch No: 607903) were purchased from Servier Pharmaceutical Co., Ltd. (Tianjin, China). HPLC grade methanol, acetonitrile and formic acid were purchased from Tedia (Ohio, USA). Guaranteed grade perchloric acid was purchased from Sinopharm Chemical Reagent Co., Ltd (Shanghai, China). Analytical grade ammonium acetate was purchased from Nanjing Chemical Reagent Co., Ltd. (Nanjing, China). Water was purified with a Millipore Milli Q-Plus system (Millipore, MA, USA).

2.2. Instruments

Quantitative analysis was performed with a Dionex Ultimate 3000 chromatographic system (Thermo Scientific, MA, USA) coupled to a TSQ Quantum Ultra AM triple quadrupole mass spectrometer (Thermo Scientific, MA, USA) operated in positive electrospray ionization (ESI) through multiple reaction monitoring

(MRM) mode. System control and data acquisitions were conducted by LCQUAN™ 2.9QF1 (Thermo Scientific, MA, USA).

2.3. Liquid chromatographic and mass spectrometric conditions

2.3.1. Indapamide and perindopril

Simultaneously chromatographic separations of perindopril and indapamide were achieved on a Thermo BDS Hypersil C₁₈ column (4.6 mm × 100 mm, 2.4 μm) maintained at 40 °C through linear gradient elution at 0.65 mL/min of the mobile phases consisting of A (a mixture of water and methanol (90:10, v/v) containing 0.05% ammonium acetate and 0.2% formic acid) and B (methanol containing 0.05% ammonium acetate and 0.2% formic acid) according to the following programs (A:B): 0.0 min (60:40) – 3.5 min (60:40) – 3.6 min (5:95) – 4.6 min (5:95) – 4.7 min (60:40) – 6.0 min (60:40).

Mass spectrometer was operated in a positive ionization mode and the analytes were detected by MRM with the transitions of *m/z* 366.4–132.1 for indapamide, *m/z* 369.1–135.0 for indapamide-d3, *m/z* 369.3–172.1 for perindopril, and *m/z* 373.3–176.1 for perindopril-d4, respectively. The parameters were optimized as follows: spray voltage 4.5 kV, capillary temperature 350 °C, the sheath gas 275 kPa, auxiliary gas 35 kPa, ion sweep gas 3.5 kPa and collision argon gas 1.6×10^{-6} bar. The collision energy was set 12 eV for indapamide and indapamide-d3, 16 eV for perindopril and perindopril-d4.

2.3.2. Perindoprilat

Chromatographic separation of perindoprilat was achieved on a Phenomenex PFP column (4.6 mm × 150 mm, 5 μm) maintained at 40 °C through linear gradient elution at 1 mL/min of the same mobile phases consisting of A and B according to the following programs (A:B): 0.0 min (70:30) – 1.0 min (70:30) – 1.5 min (20:80) – 5.0 min (20:80) – 5.1 min (70:30) – 7.0 min (70:30).

Mass spectrometer was operated in a positive ionization mode and the analytes were detected by MRM with the transitions of *m/z* 341.2–170.1 for perindoprilat, and *m/z* 345.2–170.1 for perindoprilat-d4. The parameters were optimized as follows: spray voltage 4.5 kV, capillary temperature 350 °C, the sheath gas 275 kPa, auxiliary gas 35 kPa, ion sweep gas 3.5 kPa and collision argon gas 1.6×10^{-6} bar. The collision energy was set 15 eV for perindoprilat and perindoprilat-d4.

2.4. Preparation of calibration curve and quality control (QC) samples

Primary stock solutions of indapamide (100 μg/mL) and perindopril (100 μg/mL) were prepared in acetonitrile and diluted with the same solution to make a series of standard working solutions of 5, 12.5, 25, 50, 125, 250, 500, 1000 and 1250 ng/mL for indapamide and 2, 5, 10, 20, 50, 100, 200, 400 and 500 ng/mL for perindopril. Primary stock solution of perindoprilat (100 μg/mL) was prepared in a mixture of methanol and water (80:20, v/v) and diluted with the same solution to make a series of standard working solutions of 1, 2.5, 5, 10, 25, 50, 80 and 100 ng/mL.

The stock solutions of indapamide-d3 (100 μg/mL), perindopril-d4 (100 μg/mL) and perindoprilat-d4 (100 μg/mL) were prepared in acetonitrile and diluted with the same solution at concentrations of 80 ng/mL, 60 ng/mL and 100 ng/mL, respectively.

Calibration standard samples were then prepared by 5-fold spiking the working solutions with blank plasma or whole blood to give respective final concentrations of 1, 2.5, 5, 10, 25, 50, 100, 200 and 250 ng/mL for indapamide, 0.4, 1, 2, 4, 10, 20, 40, 80 and 100 ng/mL for perindopril and 0.2, 0.5, 1, 2, 5, 10, 16 and 20 ng/mL

for perindoprilat. The low QC (LQC), medium QC (MQC) and high QC (HQC) were prepared with the same spiking procedure at concentrations of 2.5, 25 and 200 ng/mL for indapamide, 1, 10 and 80 ng/mL for perindopril and 0.5, 5, 16 ng/mL for perindoprilat. All standard solutions were stored at -20°C and plasma samples were stored at -80°C until analysis.

2.5. Sample preparation

2.5.1. Indapamide and perindopril

An aliquot of 100 μL plasma or whole blood sample was spiked with 20 μL of IS working solution. Then, 200 μL of acetonitrile was added to precipitate the protein by vortex mixing for 1 min. Following centrifugation (12,000 rpm, 10 min at 4°C), 20 μL of the supernatant was injected into the LC-MS/MS system for the analysis.

2.5.2. Perindoprilat

An aliquot of 200 μL plasma or whole blood sample was spiked with 40 μL of IS working solution. Then, 40 μL of 14% perchloric acid was added to precipitate the protein by vortex mixing for 1 min. Following centrifugation (12,000 rpm, 10 min at 4°C), 20 μL of the supernatant was injected into the LC-MS/MS system for the analysis.

2.6. Method validation

The proposed methods were validated according to the Guidelines for Bioanalytical Method Validation published by the European Medicines Agency (EMA) [17].

Specificity of the methods was investigated by comparing blank human plasma or whole blood samples obtained from six sources with those spiked with analytes and IS. The responses of endogenous interfering substances at retention time of the analytes are acceptable if there is less than 20% of the response of lower limit of quantitation (LLOQ). The responses of endogenous interfering substances at retention time of the internal standard are acceptable if there is less than 5% of the response of working internal standard. Carryover was assessed by immediately injecting blank plasma or whole blood samples after the injection of HQC samples.

Calibration curves for the methods were constructed by least-squares linear regression analysis by plotting analyte-to-IS peak area ratio versus its nominal concentration, with $1/x^2$ as the weighting factor. Sensitivity was determined by analyzing six replicates of plasma or whole blood spiked LLOQ samples. The back-calculated concentrations of each calibration standard have to be within $\pm 15\%$ deviation ($\pm 20\%$ for LLOQ) of the nominal values.

Intra-batch and inter-batch precision and accuracy were measured by analyzing QC samples at three concentration levels (LQC, MQC and HQC) with six determinations in three consecutive validation runs. The mean value should be within 15% of the actual value except at LLOQ, where it should not deviate by more than 20%. Inter-batch precision was assessed by One-way analysis of variance (ANOVA). Both intra-batch and inter-batch precision were expressed as relative standard deviation (RSD) and did not exceed 15% (20% for LLOQ).

Recovery of each analyte was determined by analyzing six replicates of QC samples at three concentration levels (LQC, MQC and HQC) and was calculated as the ratio of peak areas obtained from extracted spiked samples to that of non-extracted standard at corresponding concentrations.

Blank plasma or whole blood samples from six different single lots spiked with standard solutions at three concentration levels (LQC, MQC and HQC) were analyzed to assess the matrix effect. The matrix effect was expressed as the ratio of peak areas of

extracted blank plasma or whole blood samples spiked with the pure authentic standard solutions to the peak areas of the pure authentic standard solutions at corresponding concentrations. The IS normalized matrix factors expressed as the ratio of the matrix factor of each analyte to the matrix factor of the IS were used to assess the effects of matrix on ionization.

The stability of each analyte in human plasma or whole blood was investigated at LQC and HQC ($n = 3$) under the conditions of room temperature, three freeze-thaw (-80°C) cycles, long-term (-80°C) storage, and autosampler (8°C).

2.7. Pharmacokinetic study

The pharmacokinetics of perindopril tert-butylamine/indapamide compound tablets was conducted in Chinese healthy volunteers after oral administration. A total of 10 Chinese healthy volunteers were recruited after strict medical, biochemical and physical examinations and were given an informed consent approved by the Ethics Committee of National Medicine Clinical Trial Organization of Nanjing General Hospital (Nanjing, China) according to the principles of the Declaration of Helsinki.

After supervised overnight fasting of at least 10 h, all volunteers received study drug with 240 mL of warm water according to the randomization schedule. Blood samples were collected following oral administration of perindopril tert-butylamine/indapamide compound tablets (4 mg/1.25 mg) at pre-dose and 0.25, 0.5, 0.75, 1, 1.25, 1.5, 2, 2.5, 3, 4, 6, 8, 10, 12, 24 and 48 h. The blood samples were separated in two separate K_2EDTA vacutainer collection tubes. One of the tubes was centrifuged at 3000 rpm for 10 min and the plasma was collected. The collected plasma and whole blood samples were stored at -80°C till use. Pharmacokinetic analysis was performed by Phoenix WinNonlin 6.0.

3. Results and discussion

3.1. Method development

3.1.1. Chromatography

Indapamide, perindopril and perindoprilat have different physicochemical properties, which leads to the difficulty in setting chromatographic conditions that produce symmetrical peak shape and adequate response for all three compounds simultaneously. Hence, two different chromatographic conditions were established according to their physicochemical properties. The composition of mobile phase and column types were mainly optimized to obtain good peak shape and chromatograph separation. The mobile phases consisting of methanol-water-formic acid were chosen to enhance the response and 0.05% ammonium acetate was added to resolve the peaks free from tailing. The use of Thermo BDS Hypersil C_{18} (4.6 mm \times 100 mm, 2.4 μm) column provided good resolution and peak shapes for simultaneously indapamide and perindopril determination. In order to avoid carryover peaks after injections of high concentration samples, the proportion of organic phase was increased to 95% when indapamide and perindopril were eluted. Different types of columns like C_8 , C_{18} and PFP were studied for the analysis of perindoprilat and the best conditions were achieved with gradient elution using a Phenomenex PFP column (4.6 mm \times 150 mm, 5 μm).

3.1.2. Mass spectrometry

Mass parameters were optimized in both positive and negative ionization modes by infusion of the standard solutions into the mass spectrometer using electrospray ionization source and the optimal parameters were obtained by automatic tuning. All three compounds showed better and more stable response when

detected with positive ionization. The most sensitive mass transition was monitored from m/z 366.4–132.1 for indapamide, from m/z 369.1–135.0 for indapamide-d₃, from m/z 373.3–176.1 for perindopril, from m/z 373.3–176.1 for perindopril-d₄, from m/z 341.2–170.1 for perindoprilat, and from m/z 345.2–170.1 for perindoprilat-d₄.

3.1.3. Sample preparation

Sample preparation is a crucial factor for method development in bio-analysis to reach the maximum extraction recovery, minimum matrix effects and also minimize the sample preparation procedure. Simple protein precipitation (PP) procedure was recommended for this work since complicated liquid-liquid extraction (LLE) may compromise the stability of perindopril and influence the quantitation of perindoprilat. Protein precipitants such as acetonitrile, methanol and ethyl alcohol were investigated for the

extraction of indapamide and perindopril. 14% perchloric acid, 7% perchloric acid and 10% trifluoroacetic acid solution were tested for the extraction of highly polar perindoprilat. As a result, acetonitrile and 14% perchloric acid solution were respectively found to reach the best recovery, lowest diluting ratio and highest method sensitivity. The use of stable isotope labeled IS helped the improving of the determination accuracy of the analytes. The extraction methods were appropriate for both plasma and whole blood.

3.1.4. Comparison between the developed methods and the existing methods

As it was mentioned in Introduction, several methods have been reported for the determination of perindopril and perindoprilat or indapamide in biological samples [9–16]. However, most of the reported methods involved only one or two analytes in one

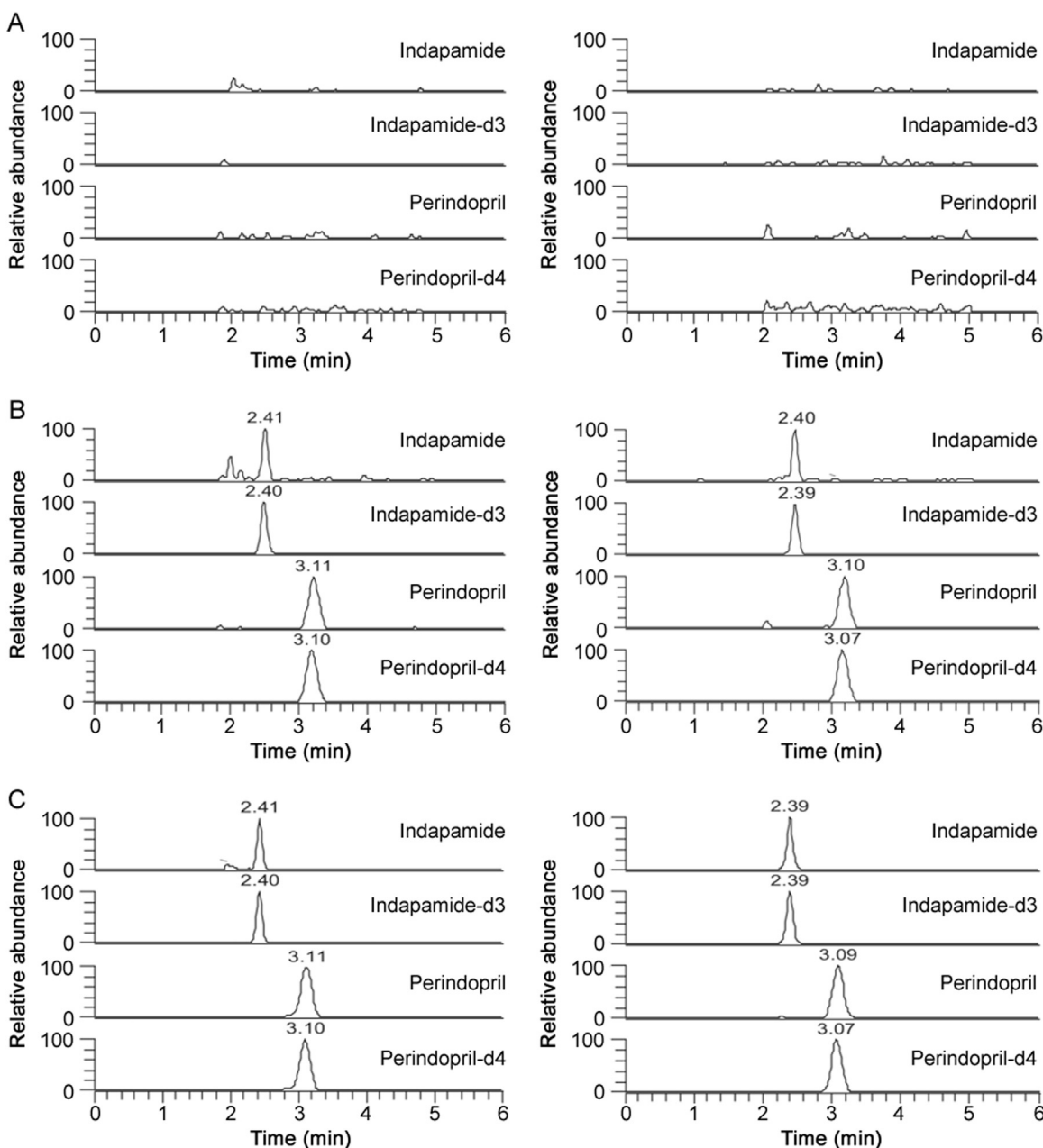


Fig. 2. Typical MRM chromatograms of indapamide and perindopril in (A) blank plasma (left panel) and whole blood (right panel); (B) LLOQ sample plasma (1.00 ng/mL for indapamide and 0.400 ng/mL for perindopril) and whole blood (1.00 ng/mL for indapamide and 0.400 ng/mL for perindopril); (C) subject sample plasma (5.32 ng/mL for indapamide and 11.1 ng/mL for perindopril) and whole blood (14.9 ng/mL for indapamide and 7.35 ng/mL for perindopril) at 2 h.

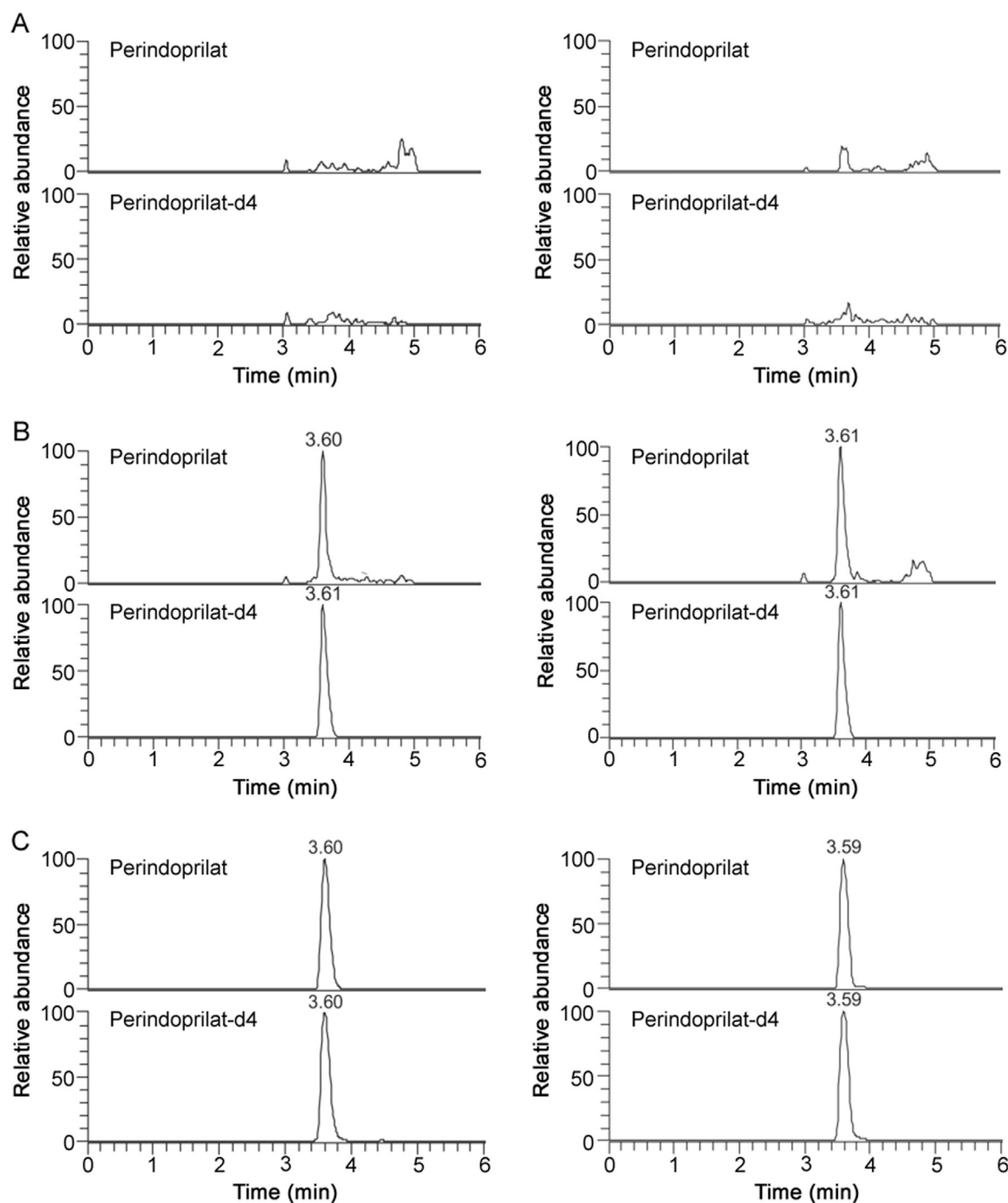


Fig. 3. Typical MRM chromatograms of perindoprilat in (A) blank plasma (left panel) and whole blood (right panel); (B) LLOQ sample plasma (0.200 ng/mL) and whole blood (0.200 ng/mL); (C) subject sample plasma (2.49 ng/mL) and whole blood (1.31 ng/mL) at 2 h.

biofluid. In this study, simple and sensitive PP methods were established for all three analytes both in plasma and whole blood. And compared to the LLE and solid phase extraction (SPE) methods in literature, the developed methods were simpler and faster when applied to high-throughput analysis.

3.2. Method validation

Fig. 2 shows the typical chromatograms of indapamide and perindopril in both the blank plasma and whole blood and the samples after oral administration of perindopril tert-butylamine/indapamide compound tablets. Fig. 3 shows the typical chromatograms of perindoprilat in both the blank plasma and whole

blood and the samples accordingly. No significant interfering peaks were observed at the retention time of analytes and ISs. No significant carry-over peaks were observed for both analytes and ISs (Tables S1 and S2).

The calibration curves ($n = 3$) were linear covering the ranges of 1–250, 0.4–100 and 0.2–20 ng/mL for indapamide, perindopril and perindoprilat, respectively, with correlation coefficient (r) > 0.99 (Tables S3–S8).

The validation results for both plasma and whole blood quality control samples are summarized in Table 1 and Table 2.

The established methods showed very good intra-batch and inter-batch precision and accuracy. The extraction was proved successful and no significant matrix effects were observed both in

Table 1
Validation results for the determination of indapamide, perindopril and perindoprilat in human plasma.

Analyte	Spiked con. (ng/mL)	Intra-batch RSD (%) (n = 6)	Inter-batch RSD (%) (n = 18)	Relative recovery (%) (n = 6)	Extraction recovery (%) (n = 6)	Matrix effect (%) (n = 6)	IS normalized matrix factors (%) (n = 6)
Indapamide	2.50	5.8	15.0	98.5 ± 4.8	126 ± 14.0	105 ± 7.2	89.6 ± 2.1
	25.0	4.5	11.5	94.5 ± 3.0	122 ± 6.8	109 ± 8.4	93.9 ± 6.9
	200	4.9	8.6	98.2 ± 5.4	103 ± 4.4	104 ± 4.3	102 ± 2.7
Perindopril	1.00	5.3	3.0	92.2 ± 7.0	102 ± 10.0	94.9 ± 4.9	102 ± 10.1
	10.0	3.8	1.4	94.8 ± 3.4	100 ± 5.8	87.4 ± 5.0	97.0 ± 3.1
	80.0	4.5	3.6	96.1 ± 4.3	112 ± 6.9	94.9 ± 2.8	100 ± 1.8
Perindoprilat	0.500	7.8	4.5	98.7 ± 7.4	78.7 ± 10.7	172 ± 14.7	102 ± 8.3
	5.00	3.3	4.4	95.3 ± 4.0	80.1 ± 9.8	180 ± 4.3	96.2 ± 4.4
	16.0	4.9	5.6	96.7 ± 4.2	80.2 ± 7.9	186 ± 9.5	101 ± 2.8

Table 2
Validation results for the determination of indapamide, perindopril and perindoprilat in human whole blood.

Analyte	Spiked con. (ng/mL)	Intra-batch RSD (%) (n = 6)	Inter-batch RSD (%) (n = 18)	Relative recovery (%) (n = 6)	Extraction recovery (%) (n = 6)	Matrix effect (%) (n = 6)	IS normalized matrix factors (%) (n = 6)
Indapamide	2.50	11.9	1.6	92.2 ± 13.6	102 ± 17.2	91.8 ± 17	92.6 ± 14.0
	25.0	6.2	3.1	99.8 ± 4.9	104 ± 8.2	85.0 ± 6.4	82.1 ± 8.7
	200	2.8	7.9	98.6 ± 2.1	100 ± 6.2	98.8 ± 5.2	112 ± 5.9
Perindopril	1.00	9.4	13.3	103 ± 11.4	95.1 ± 9.5	98.1 ± 3.5	91.5 ± 3.1
	10.0	2.8	1.6	99.3 ± 2.8	93.1 ± 4.0	92.9 ± 6.2	96.3 ± 10.9
	80.0	6.5	2.7	101 ± 6.7	89.3 ± 8.4	92.9 ± 8.1	89.4 ± 12.8
Perindoprilat	0.500	7.6	5.6	100 ± 8.6	69.5 ± 7.1	193 ± 14.4	102 ± 5.4
	5.00	2.2	5.2	94.0 ± 1.9	69.6 ± 5.8	168 ± 6.5	99.9 ± 4.9
	16.0	3.7	5.6	98.1 ± 4.7	68.2 ± 3.1	168 ± 8.1	97.6 ± 4.0

plasma and whole blood samples for indapamide and perindopril. Though some matrix effects about 180% were observed both in plasma and whole blood samples for perindoprilat, they were stable (RSD% less than 15%). And the ion enhancement was corrected with stable isotope labeled IS.

Three freeze-thaw cycles, long-term storage at -80°C for one month and short-term stability of the biological samples did not result in obvious changes in the drug concentration, as earlier publications have reported [9–14,18]. And the stability results of analytes after 30 h in autosampler at 8°C were within 85%–115% of the actual concentration (Tables S9 and S10).

3.3. Pharmacokinetic study

The validated LC-MS/MS bioanalytical method was successfully applied to determine indapamide, perindopril and its active metabolite perindoprilat in human plasma or whole blood for pharmacokinetic study in ten Chinese healthy volunteers, after oral administration of a tablet containing 4/1.25 mg perindopril tert-butylamine/indapamide in a fasting condition.

Table 3
The pharmacokinetic parameters of indapamide, perindopril and perindoprilat (mean ± SD) in Chinese healthy volunteers after oral administration of perindopril tert-butylamine/indapamide compound tablets.

Pharmacokinetic parameters	Indapamide		Perindopril		Perindoprilat	
	Plasma	Whole blood	Plasma	Whole blood	Plasma	Whole blood
C_{max} (ng/mL)	19.05 ± 5.0	62.03 ± 10.8	47.95 ± 16.2	30.95 ± 10.3	5.959 ± 3.0	3.257 ± 1.1
T_{max} (h)	1.8 ± 0.8	1.6 ± 0.6	0.65 ± 0.1	0.70 ± 0.2	6.4 ± 1.3	5.8 ± 1.1
$t_{1/2}$ (h)	13.4 ± 2.4	13.5 ± 1.6	0.96 ± 0.3	1.11 ± 0.4	17.0 ± 6.5	18.2 ± 7.3
AUC_{0-t} (ng · h/mL)	253.6 ± 83.8	881.6 ± 126.5	51.39 ± 12.8	33.98 ± 8.6	107.8 ± 34.7	60.82 ± 15.7
$AUC_{0-\infty}$ (ng · h/mL)	289.2 ± 84.7	962.8 ± 146.2	52.00 ± 12.9	34.53 ± 8.6	124.7 ± 34.8	73.75 ± 18.6

C_{max} : peak concentration in plasma or whole blood.

T_{max} : time to peak concentration.

$t_{1/2}$: half-life of drug elimination during the terminal phase.

AUC_{0-t} : area under the plasma mean concentrations–time curve from zero to t. For perindopril t = 6 h and for indapamide and perindoprilat t = 48 h.

$AUC_{0-\infty}$: The AUC_{0-t} extrapolated to infinity.

Table 3 shows the main pharmacokinetic parameters of indapamide, perindopril and perindoprilat in plasma and whole blood, respectively. The comparison between mean plasma and whole blood concentrations versus time curves of indapamide, perindopril and perindoprilat is shown in Fig. 4. C_{max} and AUC_{0-t} showed significant differences between plasma and whole blood for all three analytes. For indapamide, due to the high binding to the red blood cell [18,19] the C_{max} and AUC_{0-t} in whole blood were higher than those in plasma while it presented an opposite result for perindopril and perindoprilat. As per the literature [20], perindopril and perindoprilat bind mainly to plasma protein in blood, which resulted in the lower concentration levels in whole blood.

Table 4 shows comparison of main pharmacokinetic parameters of indapamide in whole blood, perindopril and perindoprilat in plasma between this study and reported methods. The results were in close agreement with the earlier reported values for pharmacokinetic study of two fixed dose combination formulations [16]. The T_{max} and AUC_{0-t} of indapamide in whole blood showed disparity after oral administration of indapamide tablets (1.5 mg) individually [11,21], which may be attributed to the

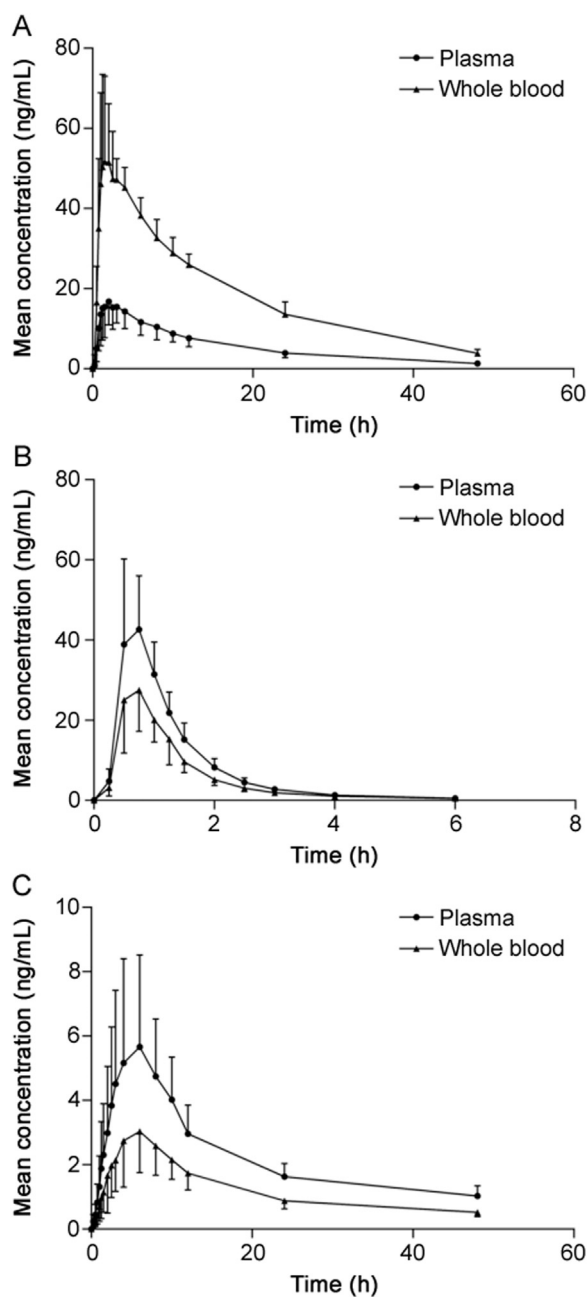


Fig. 4. The mean plasma and whole blood concentrations versus time curves of (A) indapamide, (B) perindopril and (C) perindoprilat, respectively.

different dosage forms as it has been reported that the co-administration of perindopril and indapamide does not change their pharmacokinetic properties [5]. In regard to pharmacokinetic results of perindopril and perindoprilat in plasma, they were in close proximity when compared to the others found in the literature [22,23]. However, the AUC_{0-t} values in literature [24] showed some differences, which may relate to the insensitive method of determination as the literature was published more than 20 years ago.

4. Conclusions

Simple and sensitive UPLC-MS/MS methods for the determination of indapamide, perindopril and perindoprilat in human

Table 4
Comparison of main pharmacokinetic parameters of indapamide in whole blood, perindopril and perindoprilat in plasma between this study and reported methods.

Drug	Dose (mg)	C_{max} (ng/mL)	T_{max} (h)	AUC_{0-t} (ng · h/mL)	Refs.
Indapamide	1.25	62.0 ± 10.8	1.6 ± 0.6	882 ± 126	This study
	1.25	56.2 ± 14.0	2.4 ± 1.1	1152 ± 429	[16]
	1.5	43.6 ± 16.1	10.3 ± 5.3	1318 ± 303	[11] ^a
Perindopril	1.5	41.1 ± 7.6	8.0 ± 3.0	1268 ± 279	[21] ^a
	4	48.0 ± 16.2	0.65 ± 0.1	51.4 ± 12.8	This study
	4	36.5 ± 11.4	0.66 ± 0.2	41.7 ± 10.0	[16]
Perindoprilat	4	63.9 ± 18.0	0.66 ± 0.2	70.3 ± 14.4	[22]
	4	72 ± 20	0.75	106 ± 32	[24]
	4	5.96 ± 3.0	6.4 ± 1.3	108 ± 34.7	This study
Perindoprilat	4	5 ± 2	4.3 ± 2.9	92 ± 30	[23] ^b
	4	5.91 ± 2.9	6.3 ± 1.2	111 ± 18.4	[22]
	4	4.9 ± 2.7	6	191 ± 76	[24]

AUC_{0-t} : in this study $t = 48$ h for indapamide and perindoprilat, $t = 6$ h for perindopril; Ref. [16] $t = 96$ h for indapamide and perindopril; Refs. [11,21] $t = 96$ h for indapamide; Ref. [22] $t = 5$ h for perindopril and $t = 72$ h for perindoprilat; Ref. [23] $t = 72$ h for perindoprilat; Ref. [24] $t = 120$ h for perindopril and perindoprilat.

^a Indapamide sustained-release tablets.

^b One significant digit for C_{max} .

plasma or whole blood were developed and validated. The methods were successfully applied to pharmacokinetic studies in humans. This is the first report on the pharmacokinetics of perindopril tert-butylamine/indapamide compound tablets in Chinese healthy volunteers and the pharmacokinetic results of indapamide, perindopril and perindoprilat in different biological matrices would be helpful in providing some reference for clinical application and clinical medication safety.

Conflicts of interest

The authors declare that there are no conflicts of interest.

Acknowledgments

The authors gratefully acknowledge Jiangsu Jiayi Pharmaceutical Co., Ltd. (Nanjing, China) for graciously providing help during the research and Nanjing General Hospital (Nanjing, China) for providing necessary facilities to carry out this work.

This project was supported by the Priority Academic Program Development of Jiangsu Higher Education Institutions and the Policy Directive Program of Jiangsu Province (BY2015072-03).

Appendix A. Supplementary material

Supplementary data associated with this article can be found in the online version at <http://dx.doi.org/10.1016/j.jpha.2018.05.004>.

References

- [1] M. Kumar, L. Mohan, H. Dikshit, Study of changes in renal function by perindopril and telmisartan during treatment of systemic hypertension, *J. Clin. Diagn. Res.* 8 (2014) HC 07–09.
- [2] J.J. Brugts, R. Ferrari, M.L. Simoons, Angiotensin-converting enzyme inhibition by perindopril in the treatment of cardiovascular disease, *Expert. Rev. Cardiovasc. Ther.* 7 (2009) 345–360.
- [3] F. Ma, F. Lin, C. Chen, et al., Indapamide lowers blood pressure by increasing production of epoxyeicosatrienoic acids in the kidney, *Mol. Pharmacol.* 84 (2013) 286–295.
- [4] P. Schiavi, R. Jochemsen, D. Guez, Pharmacokinetics of sustained and

- immediate release formulations of indapamide after single and repeated oral administration in healthy volunteers, *Fundam. Clin. Pharmacol.* 14 (2000) 139–146.
- [5] V. Barrios, C. Escobar, Complementary mechanisms of action and rationale for the fixed combination of perindopril and indapamide in treating hypertension – update on clinical utility, *Integr. Blood Press. Control* 3 (2010) 11–19.
- [6] G. Mancía, S. Laurent, E. Agabiti-Rosei, et al., Reappraisal of European guidelines on hypertension management: a European Society of Hypertension Task Force document, *J. Hypertens.* 27 (2009) 2121–2158.
- [7] A. Meyrier, M. Dratwa, J. Sennesaël, et al., Fixed low-dose perindopril-indapamide combination in hypertensive patients with chronic renal failure, *Am. J. Hypertens.* 11 (1998) 1087–1092.
- [8] A.J. Matheson, S.M. Cheer, K.L. Goa, Perindopril/indapamide 2/0.625 mg/day: a review of its place in the management of hypertension, *Drugs* 61 (2001) 1211–1229.
- [9] D.S. Jain, G. Subbaiah, M. Sanyal, et al., First LC–MS/MS electrospray ionization validated method for the quantification of perindopril and its metabolite perindoprilat in human plasma and its application to bioequivalence study, *J. Chromatogr. B* 837 (2006) 92–100.
- [10] R.V. Nirogi, V.N. Kandikere, M. Shukla, et al., High-throughput quantification of perindopril in human plasma by liquid chromatography/tandem mass spectrometry: application to a bioequivalence study, *Rapid Commun. Mass Spectrom.* 20 (2006) 1864–1870.
- [11] G.A. Pinto, K.I. Pastre, K.B. Bellorio, et al., An improved LC–MS/MS method for quantitation of indapamide in whole blood: application for a bioequivalence study, *Biomed. Chromatogr.* 28 (2014) 1212–1218.
- [12] D.S. Jain, G. Subbaiah, M. Sanyal, et al., Liquid chromatography-tandem mass spectrometry validated method for the estimation of indapamide in human whole blood, *J. Chromatogr. B* 834 (2006) 149–154.
- [13] L. Ding, L. Yang, F. Liu, et al., A sensitive LC–ESI–MS–MS method for the determination of indapamide in human plasma: method and clinical applications, *J. Pharm. Biomed. Anal.* 42 (2006) 213–217.
- [14] W.D. Chen, Y. Liang, H. Zhang, et al., Simple, sensitive and rapid LC–MS method for the quantitation of indapamide in human plasma—application to pharmacokinetic studies, *J. Chromatogr. B* 842 (2006) 58–63.
- [15] A. Ölçer, M. Ölçer, I. İnce, et al., The advantages of combination therapy on hypertension: development of immediate release perindopril-indapamide tablet and assessment of bioequivalence studies, *Pharm. Dev. Technol.* 21 (2016) 239–249.
- [16] D.S. Patel, Bioequivalence study of two fixed dose combination formulations of perindopril and indapamide (4 + 1.25) mg tablet in healthy human volunteers under fasting condition, *IJPI'S J. Pharmacol. Toxicol.* 1 (2011) 17–24.
- [17] EMA, Guideline on Bioanalytical Method Validation, Committee for Medicinal Products for Human Use (CHMP), London, UK, 2011.
- [18] N. Nakov, K. Mladenovska, N. Labacevski, et al., Development and validation of automated SPE–LC–MS/MS method for determination of indapamide in human whole blood and its application to real study samples, *Biomed. Chromatogr.* 27 (2013) 1540–1546.
- [19] D.B. Campbell, A.R. Taylor, Y.W. Hopkins, et al., Pharmacokinetics and metabolism of indapamide: a review, *Curr. Med. Res. Opin.* 5 (2008) 13–24.
- [20] R.J. Macfadyen, K.R. Lees, J.L. Reid, Perindopril, a review of its pharmacokinetics and clinical pharmacology, *Drugs* 39 (1990) 49–63.
- [21] F.L. Gan, X.Y. Cui, F.F. Li, et al., Pharmacokinetics and bioequivalence study of indapamide sustained-release capsules in human whole blood, *Chin. J. Hosp. Pharm.* 28 (2008) 2106–2110.
- [22] H.W. Zhang, P. Ge, W.Q. Wang, et al., Pharmacokinetics and bioequivalence study of two perindopril preparations for multiple cross-over design in healthy volunteers, *Chin. Pharm. J.* 44 (2009) 861–866.
- [23] E. Bellissant, J.F. Giudicelli, Pharmacokinetic-pharmacodynamic model for perindoprilat regional haemodynamic effects in healthy volunteers and in congestive heart failure patients, *Br. J. Clin. Pharmacol.* 52 (2001) 25–33.
- [24] V. Lachaud-Pettiti, S. Lachau-Durand, T. Duvauchelle, et al., Bioequivalence study of combination of indapamide and perindopril administered as once tablet or two capsules after oral single dose, *Am. J. Hypertens.* 8 (1995) 181A.



Short Communication

Determination of asenapine in presence of its inactive metabolites in human plasma by LC-MS/MS

Nirav P. Patel^{a,b}, Mallika Sanyal^{b,c}, Naveen Sharma^a, Dinesh S. Patel^a,
Pranav S. Shrivastav^{d,*}, Bhavin N. Patel^a^a Bioanalytical Laboratory, Clantha Research India Ltd., Bodakdev, Ahmedabad 380054, Gujarat, India^b Kadi Sarva Viswavidyalaya, Sector-15, Gandhinagar 382715, Gujarat, India^c Department of Chemistry, St. Xavier's College, Navrangpura, Ahmedabad 380009, Gujarat, India^d Department of Chemistry, School of Sciences, Gujarat University, Navrangpura, Ahmedabad 380009, Gujarat, India

ARTICLE INFO

Article history:

Received 28 October 2017

Received in revised form

14 June 2018

Accepted 15 June 2018

Available online 18 June 2018

Keywords:

Asenapine

Asenapine 13C-d3

Metabolites

LC-MS/MS

Bioequivalence study

Human plasma

ABSTRACT

A highly selective and sensitive liquid chromatography-tandem mass spectrometry (LC-MS/MS) assay has been described for the determination of asenapine (ASE) in presence of its inactive metabolites *N*-desmethyl asenapine (DMA) and asenapine-*N*-glucuronide (ASG). ASE, and ASE 13C-d3, used as internal standard (IS), were extracted from 300 μ L human plasma by a simple and precise liquid-liquid extraction procedure using methyl *tert*-butyl ether. Baseline separation of ASE from its inactive metabolites was achieved on Chromolith Performance RP_{8e} (100 mm \times 4.6 mm) column using acetonitrile-5.0 mM ammonium acetate-10% formic acid (90:10:0.1, v/v/v) within 4.5 min. Quantitation of ASE was done on a triple quadrupole mass spectrometer equipped with electrospray ionization in the positive mode. The protonated precursor to product ion transitions monitored for ASE and ASE 13C-d3 were m/z 286.1 \rightarrow 166.0 and m/z 290.0 \rightarrow 166.1, respectively. The limit of detection (LOD) and limit of quantitation (LOQ) of the method were 0.0025 ng/mL and 0.050 ng/mL respectively in a linear concentration range of 0.050–20.0 ng/mL for ASE. The intra-batch and inter-batch precision (% CV) and mean relative recovery across quality control levels were \leq 5.8% and 87.3%, respectively. Matrix effect, evaluated as IS-normalized matrix factor, ranged from 1.03 to 1.05. The stability of ASE under different storage conditions was ascertained in presence of the metabolites. The developed method is much simpler, matrix free, rapid and economical compared to the existing methods. The method was successfully used for a bioequivalence study of asenapine in healthy Indian subjects for the first time.

© 2018 Xi'an Jiaotong University. Production and hosting by Elsevier B.V. This is an open access article under the CC BY-NC-ND license (<http://creativecommons.org/licenses/by-nc-nd/4.0/>).

1. Introduction

Asenapine (ASE) is a second generation antipsychotic drug used for the acute treatment of manic or mixed episodes, associated with bipolar I disorder and schizophrenia [1–3]. Pharmacologically, ASE is a dibenzo-oxepino pyrrole drug with a tetracyclic structure. It is the ninth atypical antipsychotic agent that received regulatory approval in August 2009 from the US Food and Drug Administration (FDA) to schizophrenia and bipolar I disorder in adults [4]. It shows high affinity to serotonin receptors (5-HT_{1a}, 5-HT_{1b}, 5-HT_{2a}, 5-HT_{2b}, 5-HT_{2c}, 5-HT₅, 5-HT₆, and 5-HT₇), dopamine receptors (D₁, D₂, D₃, and D₄), alpha 1 and 2 receptors, histamine (H₁) receptors and moderate affinity to histamine (H₂) receptors. Unlike other antipsychotic agents, ASE has no

appreciable affinity towards muscarinic receptors [1,4]. ASE is unique among other atypical antipsychotics like risperidone, olanzapine and aripiprazole, in its mode of administration. It is available only as a sublingual, rapidly dissolving formulation that exposes the drug only to salivary enzymes and bypasses first pass metabolism. When administered sublingually, it has a bioavailability of about 35%, while the oral bioavailability is only 2%, when swallowed [5]. The time taken to achieve the maximum drug plasma concentration (T_{max}) after a single 5 mg dose is about 1 h. ASE is highly protein bound (95%), primarily to albumin and alpha-1 acid glycoprotein and shows excellent penetration across the blood–brain barrier. Asenapine is metabolized to several metabolites; however, none of them have any significant pharmacological activity. The primary mechanism of metabolism involves glucuronidation through UDP glucuronosyl transferase 1A4 (UGT1A4), producing asenapine-*N*-glucuronide (ASG). The other major metabolite of ASE is *N*-desmethyl asenapine (DMA), which is formed via demethylation, mainly through CYP1A2, with only minor contributions from CYP3A4 and CYP2D6 [2,6].

Peer review under responsibility of Xi'an Jiaotong University.

* Correspondence author.

E-mail address: pranav_shrivastav@yahoo.com (P.S. Shrivastav).

Literature presents few methods to determine ASE in biological samples [7–11]. Van de Wetering-Krebbbers et al. [7] studied the excretion balance and metabolism routes of ASE in humans and determined its plasma, urine and fecal concentration using high-performance liquid chromatography (HPLC). A gas chromatography-mass spectrometry (GC-MS) method is also described to analyze ASE in postmortem samples [8]. Reddy et al. [9] have presented a liquid chromatography-tandem mass spectrometry (LC-MS/MS) method for the simultaneous determination of ASE and valproic acid in human plasma. Two other methods describe quantification of ASE and its inactive metabolites in human plasma [10] and urine [11] using LC-MS/MS. In these methods [10,11], two separate assays were developed, one for ASE, DMA and 11-*O*-sulfate asenapine (OSA) and the other for ASG, respectively under gradient elution. In the present work a highly selective and sensitive LC-MS/MS assay is developed to determine ASE in human plasma in presence of its inactive metabolites, ASG and DMA. The assay presents a straightforward liquid-liquid extraction (LLE) extraction procedure to obtain a precise and quantitative recovery of ASE. The proposed method was successfully applied to a bioequivalence study of 10 mg asenapine sublingual tablet formulation in 14 healthy subjects under fasting.

2. Experimental

2.1. Chemicals and materials

Reference standards of asenapine (ASE, 99.6%), asenapine 13C₃-d₃ (IS, 99.5%), *N*-desmethyl asenapine (DMA, 99.1%) and asenapine-*N*-glucuronide (ASG, 98.7%) were procured from Clearsynth Labs (P) Ltd. (Mumbai, India). HPLC grade methanol and acetonitrile, analytical grade formic acid, ammonia and ammonium acetate were obtained from S.D. Fine Chemicals Ltd. (Mumbai, India). Deionized water used for LC-MS/MS was prepared using Milli Q water purification system from Millipore (Bangalore, India). Methyl *tert*-butyl ether (MTBE) was procured from J.T Baker Chemicals Ltd. (Haryana, India). Control buffered (K₂-EDTA) human plasma was procured from Clinical Department, Clantha Research India Limited (Ahmedabad, India) and was stored at –20 °C until use.

2.2. LC-MS/MS instrumentation and conditions

The liquid chromatography system from Shimadzu (Kyoto, Japan) consisted of an LC-10ADvp pump, an autosampler (SIL-HTc) and an on-line degasser (DGU-14A). Chromatographic column used was Chromolith Performance RP_{8e} (100 mm × 4.6 mm) from Merck (Mumbai, India). The mobile phase consisted of acetonitrile-5.0 mM ammonium acetate-10% formic acid in 90:10:0.1 (v/v/v) ratio, delivered at a flow rate of 0.9 mL/min. The auto sampler temperature was maintained at 4 °C and the injection volume was kept at 5.0 μL. Ionization and detection of ASE and IS was performed on a triple quadrupole mass spectrometer, API-4000 equipped with turbo ion spray from MDS SCIEX (Toronto, Canada) and was operated in the positive ionization mode. Quantitation was performed using multiple reaction monitoring (MRM) mode to monitor protonated precursor → product ion transition of *m/z* 286.1 → 166.0 for ASE and *m/z* 290.0 → 166.1 for IS. All the parameters of LC and MS were controlled by Analyst software version 1.6.2. The optimized mass parameters are summarized in [Supplementary material](#).

2.3. Preparation of calibration and quality control samples

The calibration standards (CSs) were made at 0.05, 0.10, 0.20, 0.50, 1.00, 2.00, 4.00, 8.00, 16.0 and 20.0 ng/mL for ASE. Six quality control

(QC) samples were prepared at the following concentrations, 0.05 ng/mL (LLOQ QC, lower limit of quantitation quality control), 0.15 ng/mL (LQC, low quality control), 1.50/5.00 ng/mL (MQC-1/MQC-2, medium quality control), 15.0 ng/mL (HQC, high quality control) and 20.0 ng/mL (ULOQ QC, upper limit of quantitation quality control).

2.4. Protocol for sample preparation

Prior to analysis, spiked plasma/subject samples were thawed and allowed to equilibrate at room temperature. The samples were adequately vortexed before pipetting. Aliquots of 300 μL plasma solutions containing 15 μL of working solution of ASE and 285 μL blank plasma were transferred into screw cap tubes. To which, 25 μL of methanol: deionized water (60:40, v/v), 50 μL working solution of IS (25.0 ng/mL) was added and vortexed to mix. Further, 500 μL of 5.0 mM ammonium acetate solution (pH 9, adjusted with ammonia) was added and vortexed again. LLE was carried out using 3.0 mL of MTBE by centrifuging the samples for 5.0 min at 1811g. After freezing the aqueous layer in dry ice bath, the organic layer was transferred in clean pre-labeled glass tubes. The samples were then evaporated to dryness at 40 °C under gentle stream of nitrogen. The dried samples were reconstituted with 500 μL of mobile phase solution and 5.0 μL was used for injection in LC-MS/MS, in partial loop mode.

2.5. Methodology for validation

Method validation for ASE in human plasma was done following the USFDA guidelines [12] and the procedures followed were similar to our previous work [13]. The details are described in [Supplementary material](#).

2.6. Bioequivalence study design and incurred sample reanalysis (ISR)

The design of study comprised an open label, randomized, two-period, two-treatment, two-sequence, crossover, balanced, single dose, evaluation of relative oral bioavailability of test (10 mg asenapine sublingual orally disintegrating tablet from an Indian company) and reference formulations (SAPHRIS[®], 10 mg asenapine sublingual orally disintegrating tablet from Merck Sharp & Dohme Company, Whitehouse Station, NJ08889, USA) in 14 healthy adult Indian subjects under fasting. The procedures followed while dealing with human subjects were based on International Conference on Harmonization, E6 Good Clinical Practice guidelines [14]. An incurred sample reanalysis (ISR) was also conducted by computerized selection of 70 subject samples near C_{max} and the elimination phase for the study as reported previously [15]. The experimental details for the study along with statistical analysis are described in [Supplementary material](#).

3. Results and discussion

3.1. Method development

The objective of the present work was to develop and validate a selective and sensitive method for ASE in presence of its inactive metabolites by LC-MS/MS and to apply the method for a bioequivalence study of ASE sublingual tablet formulation in healthy subjects. Furthermore, the sensitivity of the method should be such that it can monitor at least five half lives of ASE concentration with good accuracy and precision for the analysis of subject samples. Though there are reports on the simultaneous determination of ASE and its metabolites in human plasma and urine [10,11], two different methods were adopted to determine ASG

Table 1
Salient features of LC-MS/MS methods developed for asenapine in human plasma and urine.

Sl. No.	Linear range (ng/mL)	Sample volume	Extraction procedure	Chromatography column; elution mode and mobile phase; flow rate	Retention time; run time	Application	Ref.
1 ^a	0.1–10.02 for ASE	300 μ L plasma	Liquid-liquid extraction with methyl <i>tert</i> -butyl ether	Phenomenex C ₁₈ (50 \times 4.6 mm, 5 μ m); isocratic elution using 10 mM ammonium formate-acetonitrile (5:95,v/v); 0.8 mL/min	1.32 min; 2.50 min	Pharmacokinetic study with 5.0 mg asenapine in 8 healthy subjects	[9]
2 ^b	0.025–20.0 for ASE, 0.050–20.0 for DMA and OSA, 0.25–50.0 for ASG	500 μ L plasma	Automated solid phase extraction using 96-well Oasis HLB extraction plate	Method 1. Discovery C ₈ (150 \times 2.1 mm, 5 μ m) column for ASE, DMA and OSA Method 2. Luna C ₁₈ (30 \times 2.0 mm, 5 μ m) column for ASG; Gradient elution using 10 mM ammonium acetate and acetonitrile (10–80 %) for both the methods; 0.5 mL/min	Method 1. 3.63 min (ASE), 3.66 min (DMA), 3.59 min (OSA); 8.0 min Method 2. 2.10 min (ASG); 5.0 min	Analysis of plasma asenapine (1.0, 3.0 or 5.0 mg) in phase I clinical trial samples from 24 healthy subjects	[10]
3 ^c	0.50–100.0 for ASE and DMA and 10.0–3000 for ASG	150 μ L urine for ASE and DMA and 50 μ L for ASG	Online solid phase extraction	Chromolith RP _{8e} (100 \times 4.6 mm); isocratic elution using acetonitrile-5 mM ammonium acetate-10% formic acid in 90:10:0.1 (v/v/v); 0.9 mL/min	Method 1. 3.17 min (ASE), 3.17 min (DMA); 8.0 min Method 2. 2.26 min (ASG); 5.0 min 3.63 min; 4.50 min	Analysis of urine asenapine (1.0, 3.0 or 5.0 mg) in phase I clinical trial samples from 8 healthy subjects	[11]
4	0.050–20.0 for ASE	300 μ L human plasma	Liquid-liquid extraction with methyl <i>tert</i> -butyl ether in an alkaline medium	Chromolith RP _{8e} (100 \times 4.6 mm); isocratic elution using acetonitrile-5 mM ammonium acetate-10% formic acid in 90:10:0.1 (v/v/v); 0.9 mL/min	3.63 min; 4.50 min	Bioequivalence study with 10.0 mg sublingual tablet in 14 healthy subjects	PM

^a Together with valproic acid;

^b Along with *N*-desmethyl asenapine (DMA), 11-*O*-sulfate asenapine (OSA) and asenapine *N*-glucuronide (ASG);

^c Along with DMA and ASG.

PM: Present method

separately from ASE, DMA and OSA. Moreover, the analytes ASE, DMA and OSA were not chromatographically resolved on reversed-phase C₈ column under gradient elution conditions. Initial attempts to separate ASE from DMA (20.0 ng/mL) and ASG (20.0 ng/mL) on conventional reversed phase C₈ and C₁₈ columns like Hypurity C₁₈ (100 mm \times 4.6 mm, 5 μ m), Hypurity C₈ (100 mm \times 4.6 mm, 5 μ m), ACE C₈ (100 mm \times 4.6 mm, 5 μ m) and Eclipse XDB-C₈ (150 mm \times 4.6 mm, 3.5 μ m) were unsuccessful using acetonitrile/methanol and 2–10 mM ammonium acetate/formate buffer as the mobile phase. Additionally, the flow rate was also varied from 0.6 to 1.2 mL/min. Under these conditions it was difficult to resolve the peaks of ASE and its metabolites even up to 10 min. Attempts to increase the proportion of organic content (> 70%) or the flow rate resulted in poor resolution and peak shapes of ASG and to a lesser extent for DMA. Thus, the method was transferred to a monolithic silica column, Chromolith Performance RP_{8e} (100 mm \times 4.6 mm) and developed using the same mobile phases. However, some peak tailing was observed for ASG and also the response was not adequate for ASE under isocratic elution conditions. Thus, the mobile phase was suitably optimized along with the buffer pH. Increase in pH of buffer resulted in slight increase in retention time of ASE with limited separation from ASG. However, the best chromatographic conditions in terms of resolution, analyte response, peak shape and adequate retention were obtained using acetonitrile-5.0 mM ammonium acetate-10% formic acid (pH, 5.5) in 90:10:0.1 (v/v/v) ratio as the mobile phase at a flow rate of 0.9 mL/min. All three compounds were baseline resolved within 4.5 min. The retention time of ASE, DMA and ASG was 3.63, 2.82 and 4.05 min, respectively. Use of labeled IS helped in offsetting any possible ion suppression caused by the plasma matrix and also by compensating any inconsistency during extraction.

The mass spectra of ASE and ASE 13C-d3 (IS) were recorded in the positive ionization mode as both the compounds are basic in nature due to the presence of pyrrole ring. Using 10.0 ng/mL tuning solution, ASE and IS gave predominant singly charged protonated precursor [M+H]⁺ ions at *m/z* of 286.1 and 290.0 for ASE and IS, respectively in Q1 full scan spectra. Further, fragmentation of the precursor ion was initiated by providing sufficient nitrogen for collisional activation dissociation and by applying 20.0 psi curtain gas to obtain highly consistent and abundant product ions of ASE and IS at *m/z* 166.0 as shown in Fig. S1. Other stable product ions were also found at *m/z* 194, 215 and 229. However, due to superior signal to noise (S/N) ratio the product ion at *m/z* 166.0 was selected for quantitation. Additionally, to verify the identity of the analyte and IS qualifier transitions were also monitored at *m/z* 286.1/194.0 for ASE and *m/z* 290.0/194.1 for IS. Furthermore, to reach an ideal Taylor cone for better spectral response, nebulizer gas pressure was set at 50 psi to get a consistent and stable response. A dwell time of 300 ms was sufficient to generate at least 24 data points for quantitative analysis of ASE and IS. Also, there was no cross talk between the MRMs of ASE and IS which had identical product ions.

In a previous report, Reddy et al. [9] used LLE for the extraction of ASE from human plasma with a recovery of 81.3%. Moreover, ASE has a log *P* value of 4.9 [16]; thus LLE was tested with different solvents like *n*-hexane, MTBE, dichloromethane and diethyl ether and their binary mixtures. In these solvent systems the recovery of ASE ranged from 59% to 77% under neutral conditions. In addition, the recovery was highly consistent, especially in MTBE. In order to further improve the recovery, mild alkaline conditions (pH 9.0) were set to keep the drug in its unionized state using MTBE. The recovery of ASE (85.2%–89.4%) and IS (86.3%–88.0%) thus obtained from spiked plasma samples was highly consistent and reproducible.

The significant features of the present work include baseline separation of ASE from its inactive metabolites under isocratic

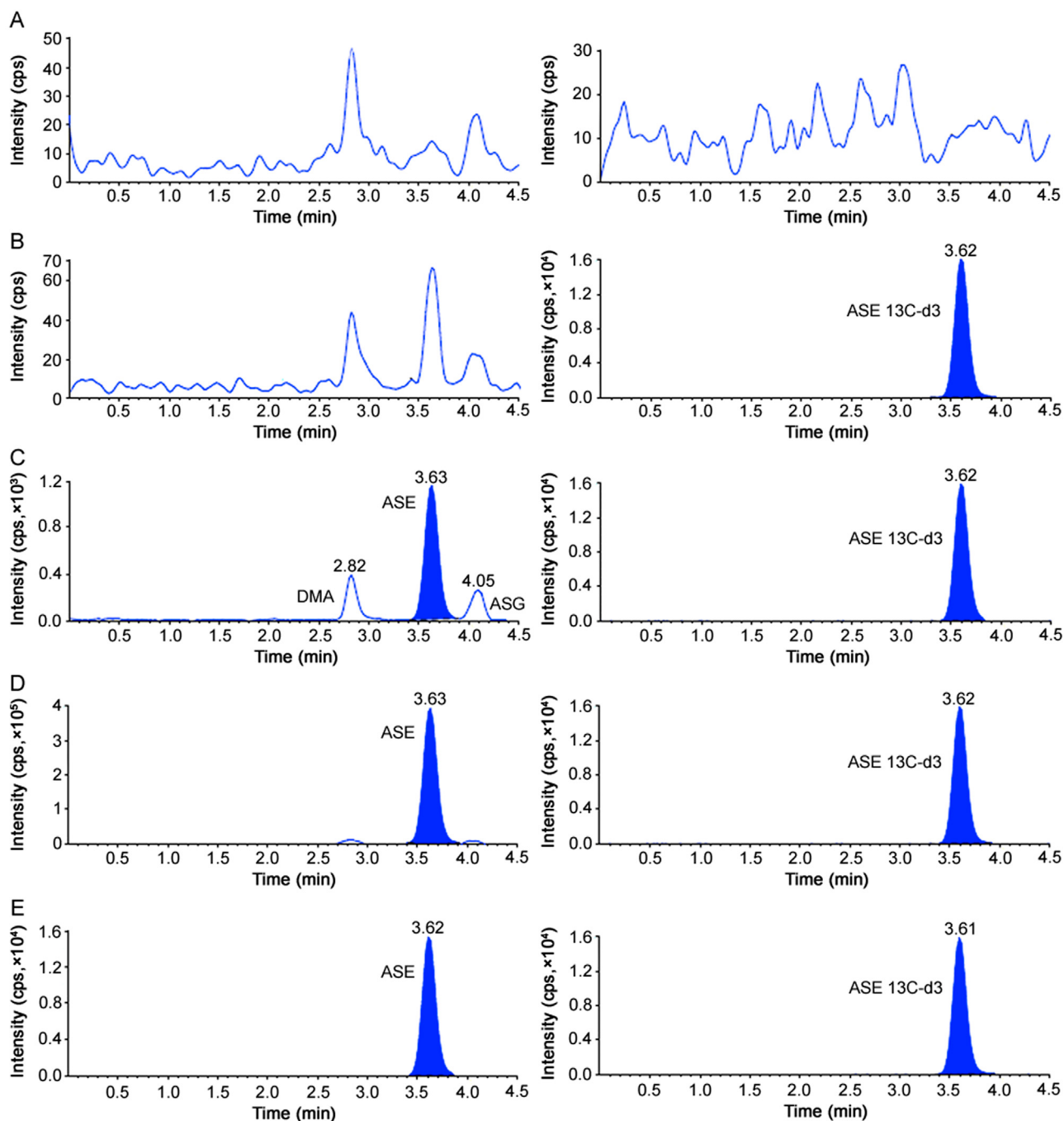


Fig. 1. Representative MRM chromatograms of (A) double blank plasma (without asenapine and asenapine13C-d3), (B) blank plasma spiked with asenapine13C-d3 (25.0 ng/mL), (C) asenapine (0.050 ng/mL), *N*-desmethyl asenapine (20.0 ng/mL) and asenapine-*N*-glucuronide (20.0 ng/mL) and asenapine13C-d3 (25 ng/mL), (D) asenapine (20.0 ng/mL), *N*-desmethyl asenapine (20.0 ng/mL) and asenapine-*N*-glucuronide (20.0 ng/mL) and asenapine13C-d3 (25 ng/mL) and (E) real subject sample at C_{max} after oral administration of 10 mg dose of asenapine.

elution, which is not possible with the existing LC-MS/MS methods employing gradient elution program [10,11]. Further, it was not feasible to analyze ASG along with ASE and other metabolites due to difference in polarity and therefore a separate method was established for ASG [10]. Besides, the newly developed method presents an efficient, relatively inexpensive and straightforward extraction procedure for precise and quantitative recovery of ASE in presence of its inactive metabolites. Though the sensitivity of ASE achieved (0.05 ng/mL) was less than the work of de Boer et al. [10] (0.025 ng/mL), it was higher than that of another report (0.10 ng/mL) [9]. On the other hand, the analysis time of 4.5 min was shorter than in methods reported for the determination of

ASE together with its metabolites [10,11]. The plasma volume used for processing is less (300 μ L) compared to the work of de Boer et al. [10], which employed 500 μ L sample volume. Moreover, their method involved an automated SPE using 96-well plate which is not used routinely. A comparative evaluation of methods developed for ASE is illustrated in Table 1.

3.2. Assay performance and validation

The selectivity of the method from endogenous plasma components was determined by analyzing eight different human plasma sources. This was done to evaluate the extent to which matrix

Table 2
Intra-batch and inter-batch accuracy and precision for asenapine.

QC level (nominal concentration, ng/mL)	Intra-day (<i>n</i> = 6; single batch)			Inter-day (<i>n</i> = 18; 6 from each batch)		
	Mean conc. found (ng/mL)	Accuracy (%)	CV (%)	Mean conc. found (ng/mL)	Accuracy (%)	CV (%)
LLOQ (0.050)	0.048	96.1	2.8	0.046	91.4	5.8
LQC (0.150)	0.146	97.4	1.8	0.140	93.0	4.0
MQC-1 (1.500)	1.492	99.5	1.9	1.455	97.0	2.4
MQC-2 (5.000)	4.798	96.0	1.7	4.653	93.1	2.8
HQC (15.00)	14.12	94.1	1.3	13.68	91.2	3.0
ULOQ (20.00)	18.98	94.9	1.8	18.37	91.9	3.4

LLOQ QC: lower limit of quantitation quality control; LQC: low quality control.
 MQC: medium quality control; HQC: high quality control; CV: coefficient of variation.

Table 3
Extraction recovery and matrix factor for asenapine in presence of its metabolites (*n* = 6).

Quality control level (ng/mL)	Mean area response (<i>n</i> = 6)			Recovery (B/A %)		Matrix factor		
	A (post-extraction spiking)	B (pre-extraction spiking)	C (neat samples in mobile phase)	Analyte	IS	Analyte (A/C)	IS	IS-normalized (analyte/IS)
0.150	17,557	14,961	17,734	85.2	86.3	0.99	0.94	1.05
1.500	173,238	154,888	176,773	89.4	87.3	0.98	0.95	1.03
5.000	551,223	480,015	568,271	87.1	86.8	0.97	0.93	1.04
15.00	1,598,648	1,398,270	1,614,796	87.5	88.0	0.99	0.96	1.03

IS: internal standard, asenapine 13C-d3.

Table 4
Stability results for asenapine under different conditions (*n* = 6).

Storage condition	Quality control level (ng/mL)	In absence of metabolites			In presence of metabolites (20.0 ng/mL of DMA and ASG)		
		Mean stability sample (ng/mL)	CV (%)	Change (%)	Mean stability sample (ng/mL)	CV (%)	Change (%)
Bench top stability (24 h, 25 °C)	0.150	0.138	2.4	– 8.0	0.155	2.3	3.3
	15.00	13.62	1.1	– 9.2	14.44	1.4	– 3.7
Freeze-thaw stability (6 cycles, –20 °C)	0.150	0.140	2.8	– 6.9	0.154	3.0	3.1
	15.00	13.93	2.3	– 7.1	14.49	1.2	– 3.4
Auto sampler stability (94 h, 5 °C)	0.150	0.141	4.6	– 6.1	0.143	4.3	– 2.3
	15.00	13.89	2.2	– 7.4	14.01	2.7	– 3.6
Processed sample stability (75 h, 25 °C)	0.150	0.138	2.6	– 8.0	0.139	3.2	– 4.1
	15.00	13.38	1.2	– 10.8	13.94	4.7	– 5.3
Long-term stability (126 days, –20 °C)	0.150	0.139	2.9	– 7.7	–	–	–
	15.00	14.05	0.8	– 6.3	–	–	–
Long-term stability (126 days, –70 °C)	0.150	0.137	4.7	– 8.4	–	–	–
	15.00	14.25	3.9	– 5.0	–	–	–

CV: coefficient of variation; DMA: *N*-desmethyl asenapine; ASG: asenapine *N*-glucuronide.

$$\text{Change (\%)} = \frac{\text{Mean stability samples} - \text{Mean comparison samples}}{\text{Mean comparison samples}} \times 100.$$

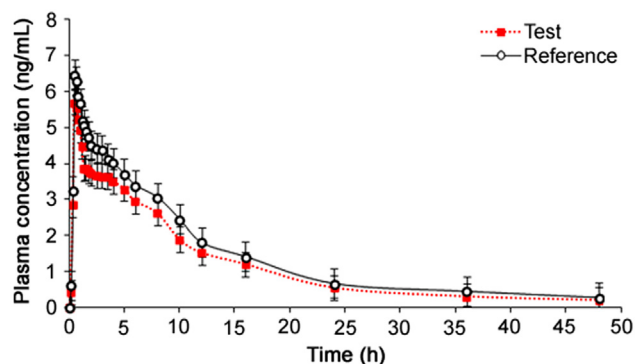


Fig. 2. Mean plasma concentration-time profile of asenapine after sublingual administration of 10 mg tablet (test and reference) formulation to 14 healthy Indian subjects under fasting.

components may interfere at the retention time of ASE and the IS. Fig. 1 demonstrates the selectivity of the method with the chromatograms of double blank plasma, blank plasma spiked with IS, ASE at LLOQ and ULOQ concentration and in subject samples. Carry-over evaluation was performed in each analytical run to ensure that it does not impact the accuracy and precision of the method. The results showed a carryover of $\leq 2.23\%$ for ASE concentration (0.05 ng/mL) in the blank plasma sample after injection of highest calibration standard (ULOQ) at the retention time of ASE. Further, there was no interference of commonly used medications by healthy volunteers like acetaminophen, aspirin, caffeine, chlorpheniramine, cetirizine, ibuprofen and pseudoephedrine at the retention time of ASE and IS. Similarly, none of the metabolites (DMA and ASG) interfered in the determination of ASE as they were chromatographically separated.

The calibration curve was linear over the concentration range of 0.05–20.0 ng/mL with correlation coefficient $r^2 \geq 0.9996$. A

Table 5
Mean pharmacokinetic parameters (\pm SD), comparison of treatment ratios and 90% CIs of natural log (Ln)-transformed following administration of 10 mg asenapine maleate sublingual tablet to 14 healthy Indian subjects under fasting.

Parameter	Test	Reference	Ratio (test/reference, %)	90% CI (Lower – Upper)	Power	Intra subject variation (% CV)
C_{\max} (ng/mL)	5.85 \pm 1.43	6.24 \pm 1.39	93.6	89.2–97.3	0.9996	9.61
AUC _{0–48 h} (h ng/mL)	36.22 \pm 7.51	41.48 \pm 9.36	87.5	83.4–91.5	0.9991	7.34
AUC _{0–inf} (h ng/mL)	39.25 \pm 6.46	44.21 \pm 8.09	88.7	85.2–93.4	0.9992	8.49
T_{\max} (h)	0.51 \pm 0.05	0.52 \pm 0.03	–	–	–	–
$t_{1/2}$ (h)	20.62 \pm 3.60	21.34 \pm 3.21	–	–	–	–
K_{el} (1/h)	0.033 \pm 0.006	0.032 \pm 0.005	–	–	–	–

C_{\max} : maximum plasma concentration; AUC_{0–t}: area under the plasma concentration-time curve from zero hour to 48 h; AUC_{0–inf}: area under the plasma concentration-time curve from zero hour to infinity; T_{\max} : time point of maximum plasma concentration; $t_{1/2}$: half-life of drug elimination during the terminal phase; K_{el} : elimination rate constant; SD: standard deviation.

straight-line fit was made through the data points by least square regression analysis to give a mean linear equation, $y = (1.2033 \pm 0.0035)x - (0.0091 \pm 0.0007)$, where y is the peak area ratio (ASE/IS) and x is the concentration of ASE. The accuracy and precision (% CV) observed for the CSs ranged from 97.3% to 102.3% and 0.6%–2.3%, respectively. The lowest concentration (LLOQ) that was measured with acceptable accuracy and precision was 0.05 ng/mL at $S/N \geq 15$, and the limit of detection (LOD) of the method was 0.0025 ng/mL.

The intra-batch and inter-batch precision and accuracy results are summarized in Table 2. The intra-batch precision (% CV) ranged from 1.3% to 2.8% and the accuracy was within 94.1%–99.5%. For the inter-batch experiments, the precision varied from 2.4% to 5.8% and the accuracy was within 91.2%–97.0%. The extraction recovery and matrix effect data for ASE and IS are shown in Table 3. Highly consistent recovery was obtained across QC levels for ASE. The IS-normalized matrix factors ranged from 1.03 to 1.05, which shows minimal interference of endogenous matrix components. Matrix effect was also checked in different plasma sources (6-K₂EDTA, 1-lipemic and 1-heamolyzed) and was also evaluated at LQC and HQC levels. The precision (% CV) in different plasma sources varied from 0.6% to 2.8% for ASE (Table S1). This was much less than that of a previous report [10], wherein it was > 15% for ASE and its IS. Post-column infusion further substantiated the absence of matrix effects with no signal enhancement or suppression at the retention time of ASE or ASE 13C-d3 (Fig. S2). There was a minor ion suppression (~ 3.0%) observed before the analyte peak at 3.3–3.4 min, but it did not interfere in the quantitation of ASE or IS.

Stability experiments were performed to evaluate the stability of ASE in stocks solutions and in plasma samples under different conditions in presence of its metabolites. ASE was found stable in controlled blank plasma at room temperature up to 24 h and for six freeze and thaw cycles. The stability of ASE in extracted plasma samples was stable for 94 h under refrigerated conditions (5 °C) and for 75 h at room temperature. The spiked plasma samples of ASE stored at –20 °C and at –70 °C for long-term stability showed no evidence of degradation even up to 126 days. The detailed stability results are shown in Table 4.

Dilution integrity of the method was checked to ascertain dilution reliability of samples having concentration of ASE above ULOQ. The precision (% CV) values for 10-fold dilution of 100 ng/mL (5 \times ULOQ concentration) were in range of 0.9%–1.5% and accuracy results was within 97.3%–100.5%. Similarly, the precision and accuracy for method ruggedness on two different Chromolith Performance RP_{8e} columns and with different analysts varied from 1.0% to 7.4% and 92.5%–96.9%, respectively for ASE.

3.3. Application of the method in healthy subjects and ISR results

The validated method was applied to a bioequivalence study of ASE in 14 healthy Indian subjects who received 10 mg test and reference formulations of ASE under fasting condition. The method was sensitive enough to monitor their plasma concentration up to 48 h. Fig. 2 shows the plasma concentration-time profile of ASE in healthy subjects. Table 5 gives the values of pharmacokinetic parameters of test and reference formulations and equivalence statistics of bioavailability for the pharmacokinetic parameters. The results obtained for C_{\max} , T_{\max} , $t_{1/2}$ and AUC were in good agreement with reported studies [3,5,9]. Further, the 90% confidence intervals of the test/reference formulations for C_{\max} , AUC_{0–48h} and AUC_{0–inf} varied from 83.4% to 97.3%, which is within the bioequivalence acceptance criterion of 80%–125%. No statistically significant differences were found between the two formulations in any parameter. Further, there was no adverse event during the course of the study. The % change in the measurement of selected subject samples for ISR was within \pm 14.5%, which confirms method reproducibility.

4. Conclusion

In summary, we have described a selective and sensitive LC-MS/MS method for the estimation of ASE in human plasma, especially to meet the requirement for subject sample analysis. The inactive metabolites, DMA and ASG, were successfully resolved on a monolithic silica column. The LLE procedure employed in the present work gave consistent and reproducible recovery for ASE. The optimized linear concentration range was adequate to monitor at least five half-lives of ASE with good accuracy and precision. Furthermore, the results of the reanalysis of study data have shown sufficient reproducibility of the method.

Conflicts of interest

The authors declare that there are no conflicts of interest.

Acknowledgments

The authors are indebted to Mr. Vijay Patel, Executive Director, Cliantha Research Ltd., Ahmedabad, India, for providing necessary facilities to carry out this work and to Mr. Anshul Dogra, Head of the Department, Cliantha Research Ltd., for his support during the course of this project.

Appendix A. Supplementary material

Supplementary data associated with this article can be found in the online version at <http://dx.doi.org/10.1016/j.jpha.2018.06.002>.

References

- [1] T. Scheidemantel, I. Korobkova, S. Rej, et al., Asenapine for bipolar disorder, *Neuropsychiatr. Dis. Treat.* 11 (2015) 3007–3017.
- [2] J.M. Gonzalez, P.M. Thompson, T.A. Moore, Review of the safety, efficacy, and side effect profile of asenapine in the treatment of bipolar I disorder, *Patient Prefer. Adherence* 5 (2011) 333–341.
- [3] Saphris® (asenapine) sublingual tablets. Full prescribing information, Schering Corporation, a subsidiary of Merck & Co. Inc., Whitehouse Station, NJ. (https://www.accessdata.fda.gov/drugsatfda_docs/label/2015/022117s017s018s0191bl.pdf). (Assessed September 2017).
- [4] C.G. Warren, S.L. Dubovsky, New approaches for the management of bipolar disorder: role of sublingual asenapine in the treatment of mania, *Neuropsychiatr. Dis. Treat.* 9 (2013) 753–758.
- [5] L. Citrome, Role of sublingual asenapine in treatment of schizophrenia, *Neuropsychiatr. Dis. Treat.* 7 (2011) 325–339.
- [6] M. Pompili, P. Venturini, M. Innamorati, et al., The role of asenapine in the treatment of manic or mixed states associated with bipolar I disorder, *Neuropsychiatr. Dis. Treat.* 7 (2011) 259–265.
- [7] S.F.M. van de Wetering-Krebbers, P.L. Jacobs, G.J. Kemperman, et al., Metabolism and excretion of asenapine in healthy male subjects, *Drug Metab. Dispos.* 39 (2011) 580–590.
- [8] C. Miller, O. Pleitez, D. Anderson, et al., Asenapine (Saphris®): gc-ms method validation and the postmortem distribution of a new atypical antipsychotic medication, *J. Anal. Toxicol.* 37 (2013) 559–564.
- [9] A.V.B. Reddy, N. Venugopal, G. Madhavi, Simultaneous determination of asenapine and valproic acid in human plasma using LC-MS/MS: application of the method to support pharmacokinetic study, *J. Pharm. Anal.* 3 (2013) 394–401.
- [10] T. de Boer, E. Meulman, H. Meijering, et al., Quantification of asenapine and three metabolites in human plasma using liquid chromatography–tandem mass spectrometry with automated solid-phase extraction: application to a phase I clinical trial with asenapine in healthy male subjects, *Biomed. Chromatogr.* 26 (2012) 156–165.
- [11] T. de Boer, E. Meulman, H. Meijering, et al., Development and validation of automated SPE-HPLC-MS/MS method for the quantification of asenapine, a new antipsychotic agent, and its two major metabolites in human urine, *Biomed. Chromatogr.* 26 (2012) 1461–1463.
- [12] Guidance for industry, bioanalytical method validation, US Department of Health and Human Services, Food and Drug Administration Centre for Drug Evaluation and Research (CDER), Centre for Veterinary Medicine (CVM), May 2001.
- [13] N.P. Patel, M. Sanyal, N. Sharma, et al., Highly sensitive LC-MS/MS method to estimate doxepin and its metabolite nordoxepin in human plasma for a bioequivalence study, *J. Pharm. Anal.* (<http://dx.doi.org/10.1016/j.jpha.2017.06.004>).
- [14] Guidance for Industry: ICH E6 good clinical practice, U.S. Department of Health and Human Services, Food and Drug Administration, Centre for Drug Evaluation and Research (CDER), Centre for Biologics Evaluation and Research (CBER), 1996.
- [15] M. Yadav, P.S. Shrivastav, Incurred sample reanalysis: a decisive tool in bioanalytical research, *Bioanalysis* 3 (2011) 1007–1024.
- [16] SAPHRIS® (asenapine maleate). Product information, Merck Sharp & Dohme Pty Limited 54-68 Ferndell Street, South Granville, NSW 2142, Australia. (<https://gp2u.com.au/static/pdf/S/SAPHRIS-PI.pdf>). (Assessed September 2017).